Diss. ETH No. 20966

Measurement of the Electronic Recoil Contamination and Development of the Control System for the ArDM Experiment

A dissertation submitted to

ETH Zurich

for the degree of

Doctor of Sciences

presented by

Ursina Lucretia Degunda

Dipl. Phys. ETH

born 18.01.1984

citizen of
Tujetsch GR

accepted on the recommendation of

Prof. Dr. André Rubbia, examiner

Prof. Dr. Klaus Kirch, co-examiner

2013

Abstract

The Standard Model of particle physics describes very accurately the visible matter surrounding us. However, astrophysical observations indicate the existence of additional invisible matter, commonly known as dark matter, which can not be explained by the Standard Model of particle physics. Dark matter is supposed to consist of massive, non-baryonic particles forming halos around galaxies. Promising candidates for these dark matter particles are the so-called WIMPs (weakly interacting massive particles). Although numerous experiments are searching for dark matter, a conclusive detection of dark matter particles is still missing.

The ArDM (Argon Dark Matter) experiment aims at the direct detection of dark matter using 850 kg of liquid argon as target. WIMPs are assumed to interact with ordinary matter by elastic scattering on the nuclei, causing a recoil of the nuclei. The goal of the ArDM experiment is to measure the recoil energies of the target nuclei. The recoil of the argon nuclei leads to ionisation and excitation of the argon atoms and thus produces free electrons and scintillation light. The design of the ArDM detector allows to detect both signals, the ionisation charge and the scintillation light, simultaneously.

Due to the small WIMP-nucleon cross section a good shielding from cosmic muons is essential for direct dark matter detection experiments. Thus, the ArDM experiment will be operated in the Canfranc Underground Laboratory in the Pyrenees. Underground operation necessitates a control system for the ArDM experiment, which monitors and regulates actively the different subsystems of the experiment. The ArDM control system is based on a programmable logic controller (PLC) and allows for process control. The first part of this work describes the development, installation and commissioning of this control system. The ArDM control system monitors all the pressures, temperatures and liquid argon levels in the ArDM detector and its cryogenic system. It also regulates the vacuum system, the cooling of the liquid argon, the argon purification and the power supply of the high voltage generator. In February 2012 the ArDM control system has been installed in the Canfranc Underground Laboratory, together with the cryogenic system of ArDM. Since then it is operated remotely without any difficulty.

The second part of this work focusses on the analysis of the scintillation light signals. The scintillation light of liquid argon is emitted by two excited molecular states with lifetimes of 7 ns and 1.6 μs, respectively [1]. The significant difference in lifetime allows to separate the two components of the scintillation light produced by the two excited molecular states. The relative intensities of these two components depend on the interacting particle and thus allow to distinguish between electronic recoil background from β or γ radiation and nuclear recoil signals from neutrons or WIMPs using pulse shape discrimination. In this work the electronic recoil contamination of nuclear recoil events, i.e. the probability of incorrectly identifying an electronic recoil event as a nuclear recoil event, is determined by applying pulse shape discrimination on data recorded with the light readout system of the ArDM detector, while the detector

was irradiated by γs emitted by a ^{22}Na source. The measured electronic recoil contamination is $(9.8 \pm 4.9) \times 10^{-5}$ for events with 59 – 97 detected photoelectrons (p.e.) and $(1.0 \pm 0.2) \times 10^{-3}$ for events with 36 – 59 detected p.e.. A Monte Carlo simulation of the fraction of electronic recoil events, which are misidentified due to photoelectron statistics, allows to estimate the rejection power for β and γ background events, which can be achieved by pulse shape discrimination for dark matter runs in the Canfranc Underground Laboratory. For a light collection yield of 2.8 p.e. per keV of electronic-equivalent recoil energy (keVee) a rejection power of $(9.5 \pm 0.3) \times 10^{-5}$ is expected for events with a nuclear recoil energy of 30 keV.

Zusammenfassung

Das Standardmodell der Teilchenphysik vermag die sichtbare Materie, die uns umgibt, sehr genau zu beschreiben. Astrophysikalische Beobachtungen deuten jedoch auf die Existenz von zusätzlicher, unsichtbarer Materie hin, die nicht mit dem Standardmodell erklärt werden kann. Diese unsichtbare Materie wird Dunkle Materie genannt. Dunkle Materie besteht vermutlich aus massereichen, nicht baryonischen Teilchen, die Halos um Galaxien bilden. Vielversprechende Kandidaten für diese Teilchen sind die sogenannten WIMPs (weakly interacting massive particles). Obwohl zahlreiche Experimente nach den Teilchen suchen, die die Dunkle Materie bilden, ist es noch nicht gelungen, diese eindeutig nachzuweisen.

Das ArDM (Argon Dark Matter) Experiment nutzt 850 kg flüssiges Argon als Target zum direkten Nachweis von Dunkler Materie. Es wird angenommen, dass WIMPs mit gewöhnlicher Materie wechselwirken, indem sie elastisch an den Kernen streuen und dabei Rückstossenergie an die Kerne abgeben. Der Rückstoss der Argonkerne führt zu Ionisation und Anregung der Argonatome und erzeugt so freie Elektronen und Szintillationslicht. Der Aufbau des ArDM Detektors erlaubt es, beide Signale, die Ionisationsladung und das Szintillationslicht, gleichzeitig zu messen.

Bedingt durch den kleinen WIMP-Nukleon-Wirkungsquerschnitt ist eine gute Abschirmung der kosmischen Myonen unerlässlich für Experimente zum direkten Nachweis von Dunkler Materie. Das ArDM Experiment wird deshalb im Untergrundlabor von Canfranc in den Pyrenäen betrieben werden. Dazu benötigt das ArDM Experiment ein Kontrollsystem, das die verschiedenen Teilsysteme des Experiments überwacht und aktiv reguliert. Das ArDM Kontrollsystem basiert auf einer speicherprogrammierbaren Steuerung (SPS) und ermöglicht eine prozessbasierte Steuerung des Experiments. Der erste Teil dieser Dissertation beschreibt die Entwicklung, Installation und Inbetriebnahme des Kontrollsystems, welches nicht nur Drücke, Temperaturen und Flüssigkeitsniveaus im Experiment überwacht, sondern auch das Vakuumsystem, die Kühlung des flüssigen Argons, die Reinigung des Argons und die Spannungsversorgung des Hochspannungsgenerators steuert. Zusammen mit dem kryogenischen System des ArDM Experiments wurde das Kontrollsystem im Februar 2012 im Untergrundlabor von Canfranc installiert. Seither wird es vom CERN aus fernbedient und funktioniert einwandfrei.

Der zweite Teil dieser Arbeit ist der Analyse der Signale des Szintillationslichts gewidmet. Das Szintillationslicht von flüssigem Argon wird von zwei verschiedenen Molekülzuständen mit einer Lebensdauer von 7 ns und 1.6 μs emittiert [1]. Da sich die beiden Molekülzustände in der Lebensdauer erheblich unterscheiden, können die von ihnen erzeugten Komponenten des Szintillationslichts unterschieden werden. Das Verhältnis der Intensitäten der beiden Komponenten hängt von der Art des Teilchens, das im Detektor wechselwirkt, ab. Dies macht es möglich, mittels der Pulsform des Szintillationssignals zwischen Elektronenrückstössen von β- und γ-Hintergrundstrahlung und Kernrückstössen, verursacht durch Neutronen oder WIMPs, zu un-

terscheiden (Pulse Shape Discrimination). In dieser Dissertation wird die Elektronenrückstoss-Kontamination (electronic recoil contamination) von Kernrückstoss-Ereignissen, d.h. die Wahrscheinlichkeit ein Elektronenrückstoss-Ereignis fälschlicherweise als Kernrückstoss-Ereignis zu identifizieren, bestimmt. Dazu wird die Methode der Pulse Shape Discrimination auf Daten angewandt, die mit dem Lichtauslesesystem des ArDM Detektors aufgezeichnet wurden, während der Detektor mit γs einer ^{22}Na-Quelle bestrahlt wurde. Die gemessene Elektronenrückstoss-Kontamination ist $(9.8 \pm 4.9) \times 10^{-5}$ für Ereignisse mit 59 – 97 detektierten Photoelektronen (p.e.) und $(1.0 \pm 0.2) \times 10^{-3}$ für Ereignisse mit 36 – 59 detektierten Photoelektronen. Mithilfe einer Monte-Carlo-Simulation des Anteils der Elektronenrückstoss-Ereignisse, die aufgrund der Photoelektronstatistik fehlidentifiziert werden, kann die Unterdrückung der β- und γ-Hintergrundstrahlung abgeschätzt werden, welche bei Betrieb des Experiments im Untergrundlabor in Canfranc erreicht werden kann. Die Simulation zeigt, dass bei einer Lichtausbeute von 2.8 p.e./keVee (p.e. per keV of electronic-equivalent recoil energy) für Ereignisse, bei denen eine Rückstossenergie von 30 keV auf den Argonkern übertragen wird, eine Unterdrückung von $(9.5 \pm 0.3) \times 10^{-5}$ erwartet werden kann.

Contents

Chapter 1

Introduction

1.1 Dark Matter

Astronomical observations indicate the existence of non-baryonic matter, which does not absorb or emit photons and hence is invisible. The nature of this so-called dark matter is unknown so far. The Standard Model of particle physics, which describes the known elementary particles and their interactions very successfully, does not provide a particle, that could account for dark matter.
The following sections give a short overview of the indications for dark matter and possible dark matter candidates. An extensive review on dark matter can be found in Reference [2].

1.1.1 Evidence for Dark Matter

The first evidence for the presence of dark matter in the universe was discovered by Fritz Zwicky in 1933 [3]. He studied the red shift of galaxies in the Coma Cluster. By comparing the mass of the luminous matter in the Coma Cluster with the mass estimated by means of the average velocity of the galaxies in the cluster, he found a big discrepancy and concluded that a non-luminous form of matter exists.

In the 1970s Vera Rubin discovered that rotation curves of galaxies, showing the rotational velocity of the stars or gas in the galaxy as a function of their distance from the center of the galaxy, are flat out to very large distances from the galaxy center [4]. From classical mechanics of circular motion follows, that in the outer region of a galaxy the rotational velocity is proportional to the inverse of the square root of the distance from the galactic center. The uniformity of the rotational velocity can be explained with the existence of a spherical dark matter halo surrounding the galaxy. Figure 1.1 shows the measured rotation curve of the galaxy NGC 6503 [5]. It illustrates that the mass of the stars and the gas in the galaxy does not suffice to explain the rotation curve, but adding a dark matter halo gives a good fit of the measured rotational velocity.

Gravitational lensing observations provide another evidence for dark matter. Gravitational lensing is an effect predicted by general relativity. Light emitted from a distant source is bent by large masses on the way to the observer. This gives the possibility to measure the existence of non-luminous mass. Hubble Space Telescope images show multiple and distorted images of distant galaxies. The light from these distant galaxies bends around a closer galaxy cluster. The geometry of the distortion allows to reconstruct the absolute mass and the mass distribution of the bending galaxy cluster. The comparison with the visible mass of the cluster gives an estimate of the amount and distribution of dark matter in the cluster.

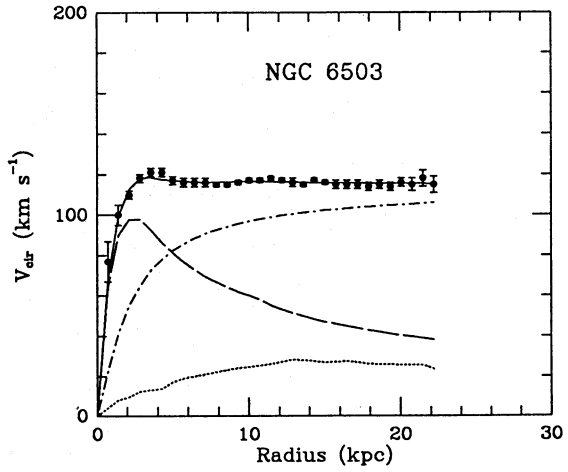

Figure 1.1: Measured rotation curve of the galaxy NGC 6503 (data points) with a dark halo fit (solid line) and the rotation curves of the individual components of the galaxy: visible matter (dashed line), gas (dotted line) and dark halo (dash-dotted line) [5].

Gravitational lensing also allowed to obtain a direct evidence for dark matter from the Bullet Cluster (1E 0657-558), which is composed of two colliding galaxy clusters [6]. The two colliding clusters consist of galaxies, plasma and presumably a large amount of dark matter. During the collision of the two clusters the galaxies behave like collisionless particles, while the plasma is slowed down by friction und is thus separated from the galaxies. By means of gravitational lensing observations a map of the mass distribution could be generated [6]. In the absence of dark matter the two centers of mass should lie in the region of the plasmas, as the mass of the plasmas is much larger than the mass of the galaxies. In Figure 1.2 the reconstructed total mass distribution is shown superimposed on the plasma distributions measured with X-ray observation. The centers of mass are clearly shifted from the centers of the plasmas, which demonstrates that a large amount of the mass in the Bullet Cluster is not slowed down during the collision and is non-luminous.

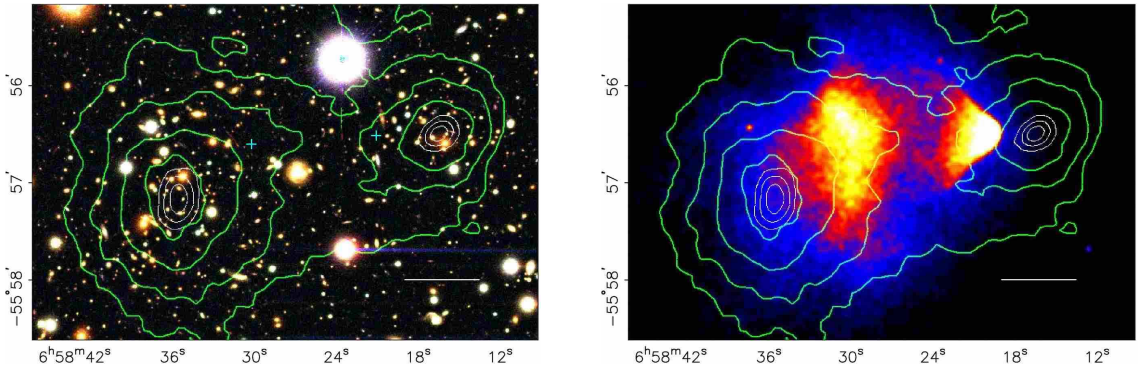

Figure 1.2: *Left:* Image of the Bullet Cluster (1E 0657-558). The mass distribution was determined with gravitational lensing observations and is shown in green. *Right:* The plasmas of the colliding clusters are superimposed on the mass distributions. They are clearly displaced compared to the centers of mass [6].

Further evidence for dark matter can be obtained from the cosmic microwave background (CMB), the relic photons from the time of the photon decoupling. The CMB has an average temperature of 2.73 K [7]. Temperature anisotropies at a level of 10^{-5} have been measured [8].

These anisotropies are ascribed to small fluctuations in the densities of luminous and dark matter at the time of the photon decoupling. The density fluctuations from the luminous and the dark matter can be distinguished, as the luminous matter, in contrast to the dark matter, interacts with photons. The measured temperature anisotropies indicate that, at the time of the photon decoupling, the universe contained about five times more dark matter than luminous matter.
Furthermore, CMB measurements evidence that the universe is composed of about 73 % dark energy[1], 23 % dark matter and 4 % ordinary matter.

1.1.2 Dark Matter Candidates

What dark matter consists of is not known yet. A pure baryonic composition would lead to a conflict with the theory of primordial nucleosynthesis. The primordial nucleosynthesis describes the formation of light nuclei, i.e. deuterium, helium and lithium, a few hundred seconds after the Big Bang. The theory predicts the observed abundances of the light elements in the universe very precisely under the assumption that only 4 % of the universe consists of baryonic matter. Thus, the amount of baryonic matter created by the Big Bang is too small to account for all the dark matter.

Non-baryonic dark matter candidates have to be massive, stable and only weakly and gravitationally interacting. There are several candidates for non-baryonic dark matter, for example sterile massive neutrinos, axions or weakly interacting massive particles (WIMPs). As dark matter seams to form large structures in the universe, it is presumably non-relativistic. Thus, standard model neutrinos can be excluded.

Sterile neutrinos are hypothetical particles similar to the standard model neutrinos. But they would be right-handed and thus only interacting gravitationally or via neutrino oscillation. If they have enough mass, they could be the dark matter particles [9].

Axions were originally proposed as an extension of the standard model to solve the strong CP problem, which arose, because no experimental observation indicates a violation of the CP-symmetry by the strong interaction, although quantum chromodynamics provides no reason why it should be conserved. Axions are considered as dark matter candidates because they are supposed to interact only weakly with ordinary matter. Depending on their mass axions could explain dark matter [2].

The expression WIMP has been created for hypothetical particles with a mass above 1 GeV, which comply with all the requirements on the dark matter particles: They are non-relativistic and their interaction cross section with ordinary matter is at the weak scale or even smaller. A possible WIMP candidate is the lightest supersymmetric particle (LSP), which is motivated by the supersymmetric extension of the standard model [2].

[1] Dark energy is hold responsible for the acceleration of the expansion of the universe. However, the nature of dark energy is not known.

1.2 Dark Matter Search

Three different methods are used to search for dark matter particles and particularly for WIMPs: direct detection, indirect detection and search with collider experiments.
Collider experiments may find supersymmetric particles. To prove that these particles are the dark matter particles is difficult, but the discovery may provide an indication of the mass of the dark matter particles.

1.2.1 Indirect Detection of Dark Matter

Indirect detection of dark matter aims to find products of dark matter annihilation, such as gamma-rays, neutrinos, or positrons.
Possible gamma-rays originating from dark matter annihilation can be detected with satellites such as the Fermi Gamma-ray Space Telescope [10] or with imaging atmospheric Cherenkov telescopes such as MAGIC [11]. An excess of gamma-rays in the few GeV energy region coming from the galactic center was discovered in the data from the Fermi Gamma-ray Space Telescope [12]. This excess could be caused by dark matter, but also by other astrophysical effects [13].
Dark matter could be gravitationally trapped inside the sun or the earth. The annihilation of the trapped dark matter particles would lead to an enhanced neutrino flux from the sun and the earth, which could be measured with large neutrino telescopes, such as IceCube [14] and ANTARES [15], which use ice and sea water, respectively, as target.
The annihilation of dark matter can also produce an excess of positrons. The PAMELA satellite-based experiment [16] and the Fermi Gamma-ray Space Telescope [17] have measured such an excess. Also in this case, the excess could be due to dark matter annihilation as well as to astrophysical sources, such as pulsars.

1.2.2 Direct Detection of Dark Matter

The WIMPs are expected to form halos around galaxies, including the Milky Way. The WIMP halos are at rest with respect to the center of the their galaxy. The earth moves in the dark matter halo of the Milky Way with an average velocity of 245 km/s. The seasonal velocity variations due to the rotation around the sun amount to ± 15 km/s [18]. WIMPs can interact with ordinary matter by elastic scattering on the nuclei. This leads to recoils of the target nuclei. Direct detection of WIMPs is based on the measurement of these nuclear recoils in a detector. For WIMP masses in the range of $10 - 1000$ GeV the typical recoil energies are between 1 and 100 keV [19]. The recoil energy spectrum is expected to decay exponentially with increasing nuclear recoil energy [19]. The shape of the spectrum depends on the WIMP mass and the mass of the nuclei of the detector material.
Crucial for direct dark matter detection are a large target mass, low background radiation and a low energy threshold. There are two different possible types of WIMP-nucleus scattering: the spin-independent (scalar) coupling and the spin-dependent (axial-vector) coupling. For experiments investigating spin-independent scattering, target materials with heavy nuclei are advantageous, because the WIMP-nucleus cross section increases with the mass of the nucleus. In spin-dependent interactions the WIMP couples to unpaired nuclear spins J. The cross-section is in this case proportional to $J(J+1)$. Thus, for experiments investigating spin-dependent scattering large nucleus masses are less important than the spin of the target nuclei [2].

Depending on the detector material the recoil energy can be converted into phonons (heat), ionisation of the detector material or excitation of the target atoms followed by the emission of scintillation light. Direct dark matter detection experiments measure one or more of these characteristics.

The DAMA/LIBRA experiment [20] at the Gran Sasso National Laboratory in Italy measures the scintillation light caused by nuclear recoils using 250 kg of ultra-pure NaI(Tl) crystals. The rate of events in the energy interval $2-6$ keV measured by the DAMA/LIBRA experiment shows an annual modulation at a confidence level of 8.9 σ. The modulation could be a consequence of the annual variation of the dark matter flux due to the rotation of the earth around the sun, but the region of cross section and WIMP mass investigated by the DAMA/LIBRA experiment was later excluded by other experiments described below, which found no evidence for dark matter in this region.
Also the CoGeNT experiment, which is operated in the Soudan Underground Laboratory in Minnesota, observed an annual modulation of the event rate in a parameter space excluded by other experiments [21]. The CoGeNT experiment is a germanium detector, that measures the free charge produced by ionisation.
The CRESST experiment [22] at the Gran Sasso National Laboratory uses $CaWO_4$ crystals as target. Phonon signals and scintillation light are detected simultaneously. During an exposure of 730 kg $\times$ days, 67 low energy nuclear recoil events have been observed. These events can not completely be explained by the background sources at a significance larger than 4 σ. The parameter space compatible with the results from CRESST has also been excluded by other experiments.

The EDELWEISS [23] and CDMS [24] experiments also detect phonon signals, but in contrast to the CRESST experiment not combined with the scintillation light, but with the ionisation charge created by an interaction in the detectors. The target materials are for both experiments semiconductors. EDELWEISS uses germanium detectors while CDMS uses both, germanium and silicium detectors. The WIMP search of EDELWEISS in the Laboratoire Souterrain de Modane in Savoy with an exposure of 384 kg $\times$ days resulted in a null result. It could exclude WIMP-nucleon cross sections down to 4.4×10^{-44} cm^2 for a WIMP mass of 85 GeV at a confidence level of 90 % [23]. Also the CDMS experiment, located in the Soudan Underground Laboratory, did not detect an evidence for dark matter and excluded WIMP-nucleon cross sections down to 3.8×10^{-44} cm^2 for a WIMP mass of 70 GeV at a confidence level of 90 % [24].

Liquid noble gases are used as detector materials for direct dark matter search, as they have good scintillation properties and allow to measure the ionisation charge simultaneously. Liquid xenon is used by several experiments, such as XENON100 [25] and ZEPLIN-III [26]. Both experiments are double phase TPCs (time projection chambers). The ZEPLIN-III experiment at the Boulby Underground Laboratory in North East England excluded WIMP-nucleon cross sections down to 3.9×10^{-44} cm^2 for WIMP masses near 50 GeV at a confidence level of 90 % [26]. The XENON100 experiment at the Gran Sasso Laboratory has a target mass of 62 kg. It set the most stringent limit on the WIMP-nucleon cross section by excluding cross sections down to 2×10^{-45} cm^2 for WIMP masses of 55 GeV [27] at 90 % confidence level. The WIMP search of XENON100, as well as the results of the EDELWEISS, CDMS and ZEPLIN-III experiments mentioned above, excluded the regions of WIMP-nucleon cross section and WIMP mass, where the DAMA/LIBRA, the CoGeNT and the CRESST experiments found indications for dark matter.

Liquid argon as detector material was for instance chosen for the ArDM (Argon Dark Matter) [28], the DarkSide [29] and DEAP-3600 [30] experiments. The MiniCLEAN experiment [31] is designed to be operated with liquid argon or with liquid neon. While DEAP-3600 and MiniCLEAN are single phase detectors and measure only the scintillation light, ArDM and DarkSide are double-phase TPCs detecting both, scintillation light and ionisation charge. All of the here mentioned experiments using liquid argon as detector material are still under development or

in the commissioning phase. The DEAP-3600 and MiniCLEAN experiments will be operated at SNOLAB in Sudbury, Ontario, while DarkSide will be placed in the Gran Sasso Laboratory.

A summary of the favoured regions and current experimental limits of the WIMP-nucleon cross section for spin-independent interaction is shown in Figure 1.3. The results from the experiments mentioned above are shown together with the limits from the COUPP [32] and SIMPLE [33] experiments, two superheated liquid detectors.

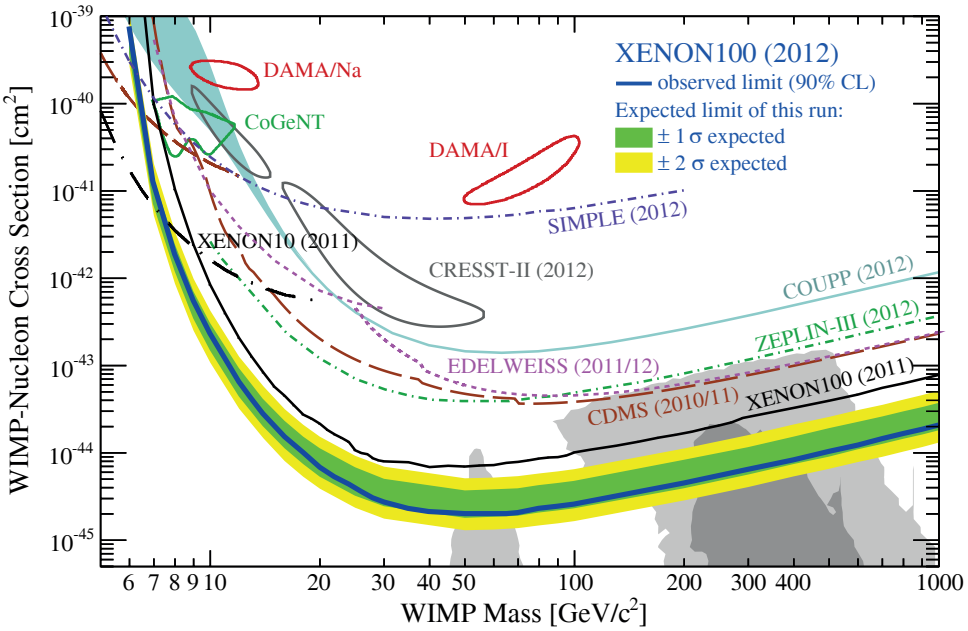

Figure 1.3: WIMP-nucleon cross section as a function of the WIMP mass for spin-independent elastic scattering. The exclusion limit of XENON100 (90% CL) and the expected 1σ and 2σ sensitivity band for the last XENON100 run are shown together with the limits and favoured areas from other experiments. The regions preferred by supersymmetric models (Constrained Minimal Supersymmetric Standard Model, CMSSM) are marked in gray ($1\sigma/2\sigma$) [34–36]. The figure is taken from [27].

1.3 The ArDM Experiment

ArDM is an experiment for direct detection of dark matter particles, which uses liquid argon as detector material. An advantage of liquid noble gases as target for WIMP searches is the possibility to build large detectors up to the ton scale and beyond. This allows the ArDM experiment to employ a target mass of 850 kg. The ArDM detector is currently built at CERN and will be operated in the Canfranc Underground Laboratory (Laboratorio Subterráneo de Canfranc, LSC) in the Pyrenees, where the cryogenic system and the control system for ArDM already have been installed.

In liquid argon, recoils of nuclei due to elastic scattering with WIMPs would lead to ionisation and excitation of argon atoms. The excitation of the argon atoms is then followed by the emission of scintillation light. The ArDM detector is designed to measure both signals, the scintillation light and the ionisation charge, simultaneously. This allows to identify interacting particles based on their ratio of produced scintillation light to ionisation charge and provides an important contribution to the background rejection. The main detector components are thus

the light readout system, consisting of an array of photomultiplier tubes (PMTs) to detect the scintillation light, a high voltage generator, providing an electric field to separate the electrons from the argon ions and drift them to the liquid argon surface, and a charge readout system, which then detects the free electrons.
Compared to xenon, argon has the advantage, that the WIMP event rate is less sensitive to the detection threshold on the recoil energy. This is due to the nuclear form factors. For a detection threshold on the nuclear recoil energy of 30 keV, the event rates per unit target mass are similar for argon and xenon. For higher thresholds the event rate in argon exceeds the event rate in xenon. Thus, experiments using liquid argon as detector material can focus on higher energetic recoil events, while for liquid xenon detectors, it is important to have a very low detection threshold. For this reason, the ArDM detector is designed to detect the scintillation light and the ionisation charge of events with nuclear recoil energies down to 30 keV and the region of interest of the ArDM experiment is defined as the nuclear recoil energy window of 30 – 100 keV.

1.4 Organisation of this Thesis

After a short introduction to the phenomenon of dark matter and direct dark matter search experiments in Chapter 1, Chapter 2 focuses on the ArDM experiment. The mechanisms of light and charge production in liquid argon are explained, followed by a description of the detector design, the individual detector components and the cryogenic system.
In Chapter 3 the development of sensors, readout devices and installation methods for temperature and liquid argon level measurements in the ArDM detector and its cryogenic system are presented. The integration of these sensors into the ArDM control system, which monitors and regulates the various subsystems of the experiment, follows in Chapter 4. This chapter describes the ArDM control system in detail, focusing on the monitoring of the cryogenic system as well as the regulation of the vacuum system, the cooling of the liquid argon and the argon purification systems. Also the planned control of the power supply for the high voltage generator, providing the electric field to drift the electrons towards the charge readout system, is discussed.
Chapter 5 describes the installation of the ArDM control system at the Canfranc Underground Laboratory and the subsequent commissioning of the vacuum control system.
In Chapter 6 the response of the ArDM detector to nuclear recoils in single phase configuration is investigated and the electronic recoil contamination of nuclear recoil events, i.e. the probability of incorrectly identifying an electronic recoil event as a nuclear recoil event, is measured by applying pulse shape discrimination on data recorded with the light readout system of the ArDM detector using a γ source. An overview of the different background sources and rates expected in the Canfranc Underground Laboratory is given, followed by an estimation of the rejection power for β and γ events, which can be achieved by pulse shape discrimination for measurements in the Canfranc Underground Laboratory.

Chapter 2

The ArDM Experiment

The Argon Dark Matter (ArDM) experiment is a double phase argon calorimeter and time projection chamber (TPC) for direct detection of dark matter. Liquid argon is very well suited as detector material for direct dark matter detection. It has excellent scintillation properties and free electrons can drift in liquid argon without being absorbed immediately. The relatively high density of liquid argon increases the probability for rare interactions such as elastic scattering of weakly interacting massive particles (WIMPs) on nuclei. Liquid argon features also good self-shielding. Its radiation length is 14.0 cm [37] and delimiting the fiducial volume helps to reject background events due to particles entering the detector. As noble gas, argon has a very low chemical reactivity. Thus, impurities in argon can be filtered out. Moreover, argon is easily available and cheap. It accounts for about 1% by volume of the atmosphere and can be extracted from air by distillation. Table 2.1 summarises some of the physical properties of argon.

Parameter	**Value**	**Reference**
atomic number	18	
molar mass	39.948 g/mol	
boiling temperature at 1.013 bar	87.3 K	[38]
density of the liquid at the normal boiling point	1395 kg/m^3	[38]
density of the gas at the normal boiling point	5.774 kg/m^3	[38]
molar enthalpy of vaporisation at the normal boiling point	6.43 kJ/mol	[38]
dielectric constant of the liquid	1.496	[38]
average energy for ionization in liquid	23.6 eV	[39]
average energy for ionization in gas	26.4 eV	[40]
scintillation wavelength	128 nm	[41]
Rayleigh scattering length in liquid	90 cm	[42]
radiation length in liquid	14.0 cm	[37]

Table 2.1: Selection of physical properties of argon.

2.1 Light and Charge Production in Liquid Argon

Charged particles crossing a medium lose energy mainly by interacting with the electrons of the medium. Collisions of the particles with the electrons lead to excitation and, if the transferred energy is larger than the binding energy of the electrons, to ionisation of the atoms.
Photons deposit their energy in a medium mainly by the photoelectric effect, Compton scattering and pair production. The photoelectric effect is dominant for small photon energies in the keV range. For energies of several 100 keV to a few MeV Compton scattering becomes dominant. Pair production is only possible for energies larger than $2m_e c^2$, where m_e is the electron mass, and is the most important process for high energetic photons.
In contrast to photons and charged particles, neutrons interact mainly with the nuclei of the medium. Neutron capture, elastic and inelastic scattering are possible processes.
As the WIMP, all these particles produce excited atoms Ar^* and ions Ar^+ in liquid argon, which results in the emission of scintillation light and ionisation electrons. The scintillation mechanism of liquid argon is described in the following section.

2.1.1 Scintillation of Liquid Argon

Luminescence in liquid argon has two origins: the self-trapped exciton luminescence [43] and the recombination luminescence [44,45]. For both processes the scintillation light in liquid argon is generated by the radiative de-excitation of argon excimers, excited dimeric argon molecules. The self-trapped exciton luminescence is caused by the excited argon atoms Ar^*. By colliding with an argon atom Ar in the ground state, the excited argon atom Ar^* forms the excimer Ar_2^*, which decays into two argon atoms in the ground state emitting a photon with energy $h\nu$ [46]:

$$\begin{aligned} Ar^* + Ar &\longrightarrow Ar_2^* \\ Ar_2^* &\longrightarrow 2\,Ar + h\nu. \end{aligned} \tag{2.1}$$

The recombination luminescence process starts from the argon ion Ar^+ produced by the passage of the ionising particle:

$$\begin{aligned} Ar^+ + Ar &\longrightarrow Ar_2^+ \\ Ar_2^+ + e^- &\longrightarrow Ar^{**} + Ar \\ Ar^{**} &\longrightarrow Ar^* + \text{heat} \\ Ar^* + Ar &\longrightarrow Ar_2^* \\ Ar_2^* &\longrightarrow 2\,Ar + h\nu. \end{aligned} \tag{2.2}$$

Within a picosecond the argon ion Ar^+ forms with a neutral argon atom Ar an ionised argon molecule Ar_2^+ [45]. The ionisation electrons get thermalized by exciting and ionising other argon atoms. By recombining with such a thermalized electron the Ar_2^+ forms a highly excited argon atom Ar^{**} and an argon atom in the ground state. The Ar^{**} de-excites in a non-radiative process to the excited state Ar^*, from where the same reaction as in the case of the self-trapped exciton luminescence leads to the emission of the scintillation light [46].

The wavelength of the emitted scintillation light is for both processes in the vacuum ultraviolet (VUV) region. The spectrum of the scintillation light is peaked around 128 nm. The full width at half-maximum of this peak is about 8 nm [41, 47]. The energy of the scintillation photons of 9.8 eV is lower than the energy required to excite an argon atom to the first excited state. Thus, the liquid argon is transparent to its scintillation light. However, the scintillation photons can be absorbed by impurities in the liquid argon. They also interact with the argon atoms via Rayleigh scattering without energy transfer.

In both luminescence processes two excited molecular states, the singlet state $^1\Sigma_u^+$ and the triplet state $^3\Sigma_u^+$, emit scintillation light. The lifetime of the singlet state τ_1 is about 7 ns and thus significantly shorter than the one of the triplet state τ_3, which is about 1.6 μs for pure argon [1]. The triplet state has a longer lifetime than the singlet state, because the ground state has spin zero. The significant difference in lifetime of the two excimer states allows to separate the so-called fast component, produced by the singlet state, from the slow component of the scintillation light, which originates from the de-excitation of the triplet state.

The argon excimers can collide with impurities, such as N_2, O_2 or H_2O. The collision, here as an example with a N_2 molecule, can de-excite the argon excimers non-radiatively [48]:

$$Ar_2^* + N_2 \longrightarrow 2Ar + N_2. \tag{2.3}$$

This process leads to a decrease of the argon excimer concentration and thus the number of emitted scintillation photons. The probability to collide with an impurity, before the radiative decay occurs, is higher for longer lifetimes. Thus, for impurity concentrations at the ppm level only the measured value for τ_3 is remarkably influenced by the purity, while for τ_1 no significant dependence on the impurity concentrations was measured [48].

The relative intensity of the singlet and triplet component I_1/I_3 depends on the interacting particle. The ratio I_1/I_3 increases with increasing linear energy transfer (LET). The LET is the energy per unit path deposited along the particle track. Super-elastic collisions between singlet state excimers and thermalised electrons which change the singlet state to a triplet state excimer, may be responsible for the dependence of the ratio I_1/I_3 on the LET. For high LET the thermalised electrons combine faster with the ionised argon molecules than for low LET. Thus, for low LET the probability for a superelastic collision with a singlet state excimer is higher and more singlet state excimers are transformed to triplet state excimers [1].
The ratio I_1/I_3 can be used to determine the type of the interacting particle. It has been measured to be 0.3, 1.3 and 3 for electrons, α particles and fission fragments, respectively, [1] and depends slightly on the energy of the interacting particle. The particle discrimination based on the ratio I_1/I_3 is called pulse shape discrimination (PSD). For dark matter experiments this pulse shape discrimination is important. It allows to distinguish between electronic recoil background from β and γ radiation with low LET and nuclear recoil signals from WIMPs with higher LET.

The measured value of the average energy required to produce an electron ion pair in liquid argon is $W = 23.6$ eV [39]. The ratio of the number of excited argon atoms over the number of ionised argon atoms N_{ex}/N_i is 0.19 – 0.21 [44]. From these two values the average energy required for the production of one photon W_{ph} can be calculated [46]:

$$W_{ph} = \frac{E}{N_{ph}} = \frac{E}{N_i + N_{ex}} = \frac{E}{N_i\,(1 + N_{ex}/N_i)} = \frac{W}{1 + N_{ex}/N_i} = 19.5 \text{ eV}, \tag{2.4}$$

where N_{ph} is the maximum number of photons produced by depositing the energy E. The measured values for W_{ph} differ from the value calculated above. For 1 MeV electrons and for 5.3 MeV α particles 24.4 eV and 27.1 eV were measured [49]. The reason for the difference between calculated and measured values are several quenching processes, which suppress the photon production. As mentioned above impurities in the liquid argon lead to a reduction of the produced scintillation photons. Additionally, in the low LET region a significant number of ionisation electrons do not recombine with argon ions for several milliseconds. In the high LET

region a large number of excited argon atoms is produced. Thus, they often collide with each other and de-excite before they form excimers:

$$\mathrm{Ar}^* + \mathrm{Ar}^* \longrightarrow \mathrm{Ar} + \mathrm{Ar}^+ + \mathrm{e}^-. \tag{2.5}$$

The emitted electrons carry away the excess energy as kinetic energy [49].

Also an external electric field prevents ionisation electrons from recombining with argon ions. The number of produced photons decreases with increasing electric field strength. However, the presence of an electric drift field allows to collect the free electrons. For a given electric drift field the ratio between the produced ionisation charge and scintillation light depends on the LET und thus gives additionally to the pulse shape discrimination a second criterion for particle discrimination.

Due to the LET dependence of the quenching processes, not only the ratio $\mathrm{I}_1/\mathrm{I}_3$, but also the scintillation light yield, the mean number of photons produced per unit of absorbed energy, depends on the type of the interacting particle. For particles producing nuclear recoil events the process of nuclear quenching contributes to the reduction of the produced scintillation light. The recoiling nucleus loses its energy not only by interacting with electrons, but also by colliding with other argon nuclei. The energy lost by collisions with argon nuclei does not contribute to the production of scintillation light.
Thus, for electronic recoil events produced by β or γ radiation, the scintillation light yield is higher than for nuclear recoil events produced by neutrons or WIMPs. The scintillation efficiency L_{eff}, the ratio between the scintillation light yield for nuclear recoil events Y_{nr} and electronic recoil events Y_{e}, was measured to be about 0.25 for nuclear recoil energies up to 250 keV in the absence of an electric field [50, 51]. As for low LET the electrons recombine slower than for high LET, Y_{e} is expected to be more affected by an electric field than Y_{nr} [52]. Thus, the presence of an electric field presumably increases L_{eff}.

2.1.2 Charge Production and Electron Drift in Liquid Argon

Particles interacting with liquid argon produce free charge by ionisation of argon atoms. To generate an electron ion pair an average energy of $W = 23.6$ eV is required [39]. W is composed of the average energy expenditure E_{i} to produce a singly charged argon ion, the average energy per produced argon ion spent in excitation $E_{\mathrm{ex}}N_{\mathrm{ex}}/N_{\mathrm{i}}$ and the average kinetic energy ϵ of the ionisation electrons with energy below the lowest excitation level of argon [40]:

$$W = E_{\mathrm{i}} + E_{\mathrm{ex}}N_{\mathrm{ex}}/N_{\mathrm{i}} + \epsilon. \tag{2.6}$$

N_{i} and N_{ex} are the numbers of produced singly charged argon ions and excited argon atoms, respectively, while E_{ex} is the average energy expenditure to generate an excited argon atom.

The recombination of electrons with argon ions reduces the free charge. The fraction of recombining electrons depends on the ionisation density and on the applied electric field. For charged particles interacting in liquid argon, the effect of the ionisation density and the electric field strength $\mathcal{E}$ on the fraction R of ionisation electrons, which do not recombine, can be described by a modified Birks law [53]:

$$R = \frac{A}{1 + \frac{k}{\mathcal{E}}\frac{dE}{dx}}. \tag{2.7}$$

The stopping power dE/dx, the average energy loss per unit path length, is proportional to the ionisation density. The description of the fraction of not-combining electrons by the modified Birks law is purely phenomenological and the parameters A and k can be obtained from the fit of R to the data. The measured values for stopping muons and protons with electric field strengths between 0.2 and 0.5 kV/cm are: $A = 0.8$ and $k = 0.0347$ kV/MeV [53].

The electrons, that escape from recombination, can be collected by means of the applied electric field. In the electric field the electrons get a net velocity in the direction of the field. The drift velocity v_d, the average velocity of the electrons, depends on the electric field strength $\mathcal{E}$ and the temperature T of the liquid argon. The drift velocity increases with $\mathcal{E}$. A decrease of the drift velocity with increasing liquid argon temperature was measured [54]. The drift velocity is a linear function of the temperature and decreases with a rate of -1.72%/K. An empirical function describes the dependence of v_d on $\mathcal{E}$ and T in the range 0.5 – 13 kV/cm and 87 – 94 K [54]:

$$v_\mathrm{d}\left(T, \mathcal{E}\right) = \left(P_1\left(T - T_0\right) + 1\right)\left(P_3 \mathcal{E} \ln\left(1 + \frac{P_4}{\mathcal{E}}\right) + P_5 \mathcal{E}^{P_6}\right) + P_2\left(T - T_0\right). \tag{2.8}$$

The parameters have been determined as $P_1 = (-0.01481 \pm 0.00095)$ K^{-1}, $P_2 = (-0.0075 \pm 0.0028)$ K^{-1}, $P_3 = (0.141 \pm 0.023)$ cm/kV, $P_4 = (12.4 \pm 2.7)$ kV/cm, $P_5 = (1.627 \pm 0.078)$ (kV/cm)$^{-P_6}$ and $P_6 = 0.317 \pm 0.021$. The reference temperature T_0 was set to 90.371 K. The function gives v_d in mm/μs. The electron drift velocity reported in Reference [54] is shown in Figure 2.1 as a function of the electric field. The function (2.8) is superimposed in the figure. The measured drift velocity at 2.5 kV/cm and 87 K is $v_\mathrm{d} = 2.974$ mm/μs.

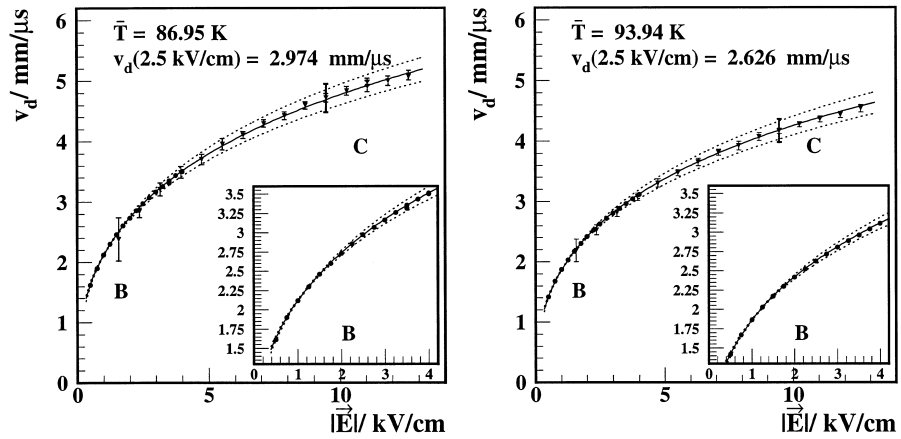

Figure 2.1: Dependence of the drift velocity v_d on the electric field strength $\mathcal{E}$ at 86.95 K and 93.94 K[1] [54].

Impurities in the liquid argon such as O_2, N_2 and CO_2 can capture free electrons and thus reduce the amount of drifting electrons. The attachment mechanism is a three body process [55]:

$$M + \mathrm{e}^- + X \longrightarrow M^- + X \tag{2.9}$$

The process does not only involve an electron and the molecule M, to which it attaches, but also an additional atom or molecule X. The electron and the molecule M form a negative molecular ion M^- in an excited state. The M^- de-excites by passing the excess energy to the additional

[1]Reprinted from Nuclear Instruments and Methods, 449, W. Walkowiak, Drift velocity of free electrons in liquid argon, 288 – 294, 2000, with permission of Elsevier

atom or molecule X [55]. The attachment mechanism leads to an exponential decrease of the number of free electrons N_e with time:

$$N_\mathrm{e}(t) = N_\mathrm{e}^0 e^{-t/\tau_\mathrm{e}}, \tag{2.10}$$

where τ_e is the lifetime of the drifting electrons and N_e^0 is the initial number of electrons that escape the recombination. The lifetime τ_e depends on the impurity concentrations $[M_i]$:

$$\tau_\mathrm{e} = \frac{1}{\sum_i k_i \, [M_i]}, \tag{2.11}$$

where k_i are the attachment rate coefficients of the electrons to the impurities M_i. The k_i are proportional to the attachment cross sections. The attachment cross sections depend on the electric field strength. For O_2 the cross section is about two orders of magnitude bigger than the ones for N_2 and CO_2 at the same field strength [55, 56]. Thus, the argon purity is often given as oxygen equivalent concentration $[O_2]_\mathrm{eq}$ assuming that the liquid argon is only contaminated by O_2. Measurements of k_{O_2} show that the electron life time can be approximated by [56, 57]:

$$\tau_\mathrm{e} \; (\mu\mathrm{s}) \;\approx\; \frac{300}{[O_2]_\mathrm{eq} \, (\mathrm{ppb})}. \tag{2.12}$$

The drifting electrons in the liquid argon are in a quasi-free state. The energy of the ground state of the quasi-free electrons in liquid argon is $V_0 = -0.2$ eV [58, 59]. To be extracted from the liquid argon to the argon gas phase the electrons have to overcome a potential barrier. In the absence of an electric field the potential barrier is $|V_0|$. However, the presence of an electric field lowers the potential barrier [58].

2.1.3 Proportional Scintillation in Argon Gas

Electrons extracted to the argon gas phase can there generate photons by exciting argon atoms. This process is called proportional or secondary scintillation. If the electric field is strong enough, that the extracted electrons gain between two collisions with argon atoms enough energy to excite the argon atoms, but not as strong, that the electrons can ionise argon atoms, the number of secondary scintillation photons is proportional to the number of extracted electrons. Thus, the ionisation charge can be detected by measuring the proportional scintillation light.
The thresholds on the electric field strength for excitation and ionisation of the argon atoms depend on the density of the argon gas. Between these two thresholds the number of photons is also proportional to the length of the drift path of the extracted electron in the gas and to the electric field strength. The excitation and ionisation thresholds are indicated in terms of the reduced electric field $\mathcal{E}/n$, defined as the electric field $\mathcal{E}$ divided by the number density n of the argon gas, in order to take into account their dependence on the argon gas density. The measured excitation and ionisation thresholds for argon gas are $\sim 2.7 \times 10^{-17}$ and $\sim 12 \times 10^{-17}$ $\mathrm{V\,cm^2\,atom^{-1}}$, respectively [60]. Between the excitation and the ionisation thresholds the reduced secondary scintillation yield Y/n, the number of photons produced per electron per path length divided by n, can be given by [60]:

$$\frac{Y}{n} = 0.081 \frac{\mathcal{E}}{n} - 0.190, \tag{2.13}$$

where Y/n is given in 10^{-17} photons $\mathrm{electron^{-1}\,cm^2\,atom^{-1}}$ and $\mathcal{E}/n$ in 10^{-17} $\mathrm{V\,cm^2\,atom^{-1}}$. At the normal boiling point of argon and an electric drift field in the argon gas of 3 kV/cm an electron produces about 80 photons per cm of drift path.

As for the primary scintillation light produced in liquid, the emission spectrum is in the VUV range and peaked at 128 nm [61]. The main process leading to the emission of the proportional scintillation light is [61]:

$$\begin{aligned} \mathrm{Ar}^* + 2\,\mathrm{Ar} &\longrightarrow \mathrm{Ar}_2^{**} + \mathrm{Ar} \\ \mathrm{Ar}_2^{**} + \mathrm{Ar} &\longrightarrow \mathrm{Ar}_2^{*} + \mathrm{Ar} \\ \mathrm{Ar}_2^{*} &\longrightarrow 2\,\mathrm{Ar} + h\nu. \end{aligned} \tag{2.14}$$

An argon atom excited by a drifting electron forms in a three-body collision with two other argon atoms the vibrationally unrelaxed excimer Ar_2^{**}. By collision with an argon atom the Ar_2^{**} falls back to the vibrationally relaxed excimer state Ar_2^{*}, which then decays to the chemically not bound ground state by emitting a VUV photon with energy $h\nu$.

2.1.4 Charge Multiplication in Argon Gas

The average energy required to generate an electron ion pair in argon gas is 26.4 eV [40]. If the reduced electric field is above the ionisation threshold, the drifting electrons gain enough energy between two collisions to ionise argon atoms and produce new free electrons, that again ionise argon atoms. This mechanism leads to a multiplication of the free charge, called avalanche multiplication.

The number of electron ion pairs produced by one electron per unit drift path is called first Townsend coefficient α. The dependence of the first Townsend coefficient on the density ρ of the gas and the electric field strength $\mathcal{E}$ can be approximated by [62, 63]:

$$\alpha = A\rho e^{-\frac{B\rho}{\mathcal{E}}}. \tag{2.15}$$

The coefficients A and B are gas-specific constants. The total number of produced electrons N_e in an avalanche starting from N_e^0 electrons is

$$N_\mathrm{e} = N_\mathrm{e}^0 e^{\int \alpha ds}, \tag{2.16}$$

where the first Townsend coefficient is integrated along the drift path of the electron avalanche.

For a uniform electric field, α is constant along the path and the total number of produced electrons can be written as

$$N_\mathrm{e} = N_\mathrm{e}^0 e^{\alpha x}, \tag{2.17}$$

where x is the length of the drift path. In this case the gas gain G, defined as $N_\mathrm{e}/N_\mathrm{e}^0$, is

$$G = \frac{N_\mathrm{e}}{N_\mathrm{e}^0} = e^{\alpha x}. \tag{2.18}$$

Charge multiplication in the argon gas allows to detect ionisation charge directly.

2.2 Design of the ArDM Detector

The ArDM detector is a double phase argon calorimeter and TPC. It is operated at the argon boiling point so that a liquid and a vapour phase coexist in the detector. The detector vessel, a 200 cm high cylindrical stainless steel dewar with a torispherical bottom, contains almost 2 tons of liquid argon. It has an inner diameter of 100 cm and is filled with liquid argon up to 187 cm above its lowest point. All the detector components are mounted to the top flange of the detector vessel. This allows to move them out of the vessel easily.

The working principle of the ArDM detector is shown in Figure 2.2. The scintillation light and the ionisation electrons generated by particles interacting with the liquid argon can both be detected with the ArDM experiment. For this purpose the ionisation electrons are drifted in an electric field of about 1 kV/cm to the liquid surface where they are extracted to the vapour phase. The drift field is generated by a Greinacher high-voltage multiplier, which is also known as Cockcroft-Walton high-voltage multiplier. Thirty circular field shaping electrodes ensure the uniformity of the drift field. They are fixed to polyethylene pillars, which support the whole inner detector. The distance between two field shaping electrodes is 40 mm. A cathode, consisting of a stainless steel grid, terminates the drift field region on the lower end. The maximum drift length from the cathode to the liquid surface is 120 cm. For this distance Equation (2.8) gives a drift time of 570 μs at an electric field strength of 1 kV/cm and at the normal boiling temperature of argon.
To extract the electrons from the liquid to the gas phase a stronger electric field is needed. Two extraction grids, the first one located 5 mm below and the second one located 5 mm above the liquid surface, provide an electric drift field of 4 kV/cm across the liquid surface and ensure the extraction of the drifting electrons.

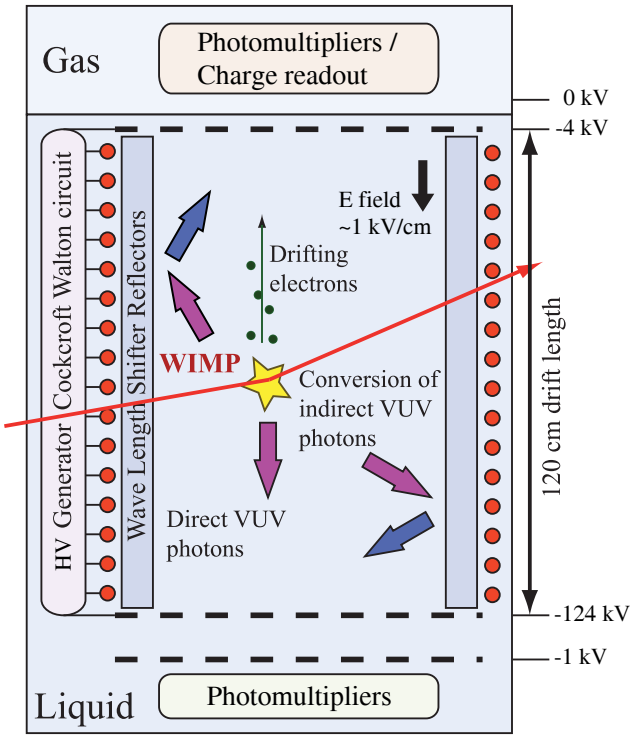

Figure 2.2: Conceptual layout of the ArDM detector. The figure is modified from [64].

Two possibilities exist to detect the extracted electrons: They can be detected directly using charge multiplication in argon gas or indirectly by detecting the photons produced by proportional scintillation in the argon gas. Both options can be implemented in ArDM. In the first case a double-stage Large Electron Multiplier (LEM) located in the vapour phase would be part of the detector. A LEM is a metal cladded epoxy plate with drilled holes. The electric field in the holes of the LEM is strong enough to multiply the charge and produce an electron avalanche. The electron avalanches induce then a signal in a two-dimensional readout anode. Alternatively, an array of photomultiplier tubes (PMTs) can be installed at the top of the detector to detect the proportional light. Both alternatives are shown in the drawings in Figure 2.3a and 2.3b. Currently, the two alternatives are still under development and a preliminary charge readout system [65] is installed in the detector. It consists of an anode with 16 segments and does not allow for charge multiplication.

For the detection of the primary scintillation light produced by the particles interacting with the liquid argon, an array of 14 PMTs is installed below the cathode at the bottom of the detector. Reflector foils covering the whole cylinder barrel defined by the field shaping electrodes improve the light collection efficiency. The reflector foils define the active volume, which has a radius of 80 cm and contains ∼850 kg of liquid argon. The bottom PMTs and the reflector foils are well visible in Figure 2.3c.

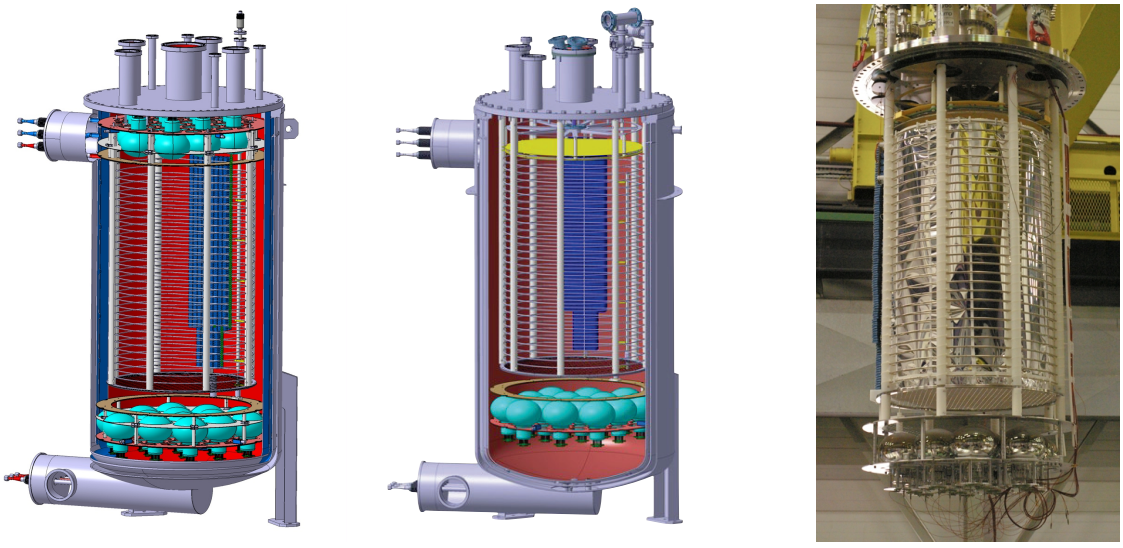

(a) **(b)** **(c)**

Figure 2.3: The ArDM detector. In (a) and (b) the detector setup is shown for the two alternative methods to measure the charge: an array of PMTs in (a) and the double-stage LEM with two-dimensional readout anode in (b). The current detector setup with the 14 bottom PMTs and a preliminary charge readout system is shown in (c).

2.3 Detector Components

The main components of the ArDM detector are the charge readout system and the high voltage system as well as the PMT array at the bottom of the detector and the reflector foils forming the light readout system. In this section these key components are described.

2.3.1 Light Readout System

The light readout system consists of 14 PMTs at the bottom of the detector and the reflector foils. The PMTs are completely immersed in liquid argon and thus have to be suitable for cryogenic use. The Hamamatsu R5912-02MOD, hemispherical 8" PMTs with bialkali photocathode and platinum underlay, were chosen. The platinum underlay below the photocathode is needed because at liquid argon temperature the bialkali photocathode becomes insulating and thus the electrons emitted by the photoelectric effect can not be replaced quickly. The platinum underlay can provide electrons and avoid the accumulation of positive charges. The PMTs are produced with low radioactive borosilicate glass to reduce the background.

Every PMT is installed on a 3 mm thick printed circuit board (PCB) base. The bases do not only provide mechanical support, but also the high-voltage supply and the signal extraction. The PCB bases are fixed to a stainless steel frame. A grid at the same potential as the photocathode shields the PMTs from the cathode high voltage. The grid and the stainless steel frame are attached to the lower end of the polyethylene pillars, which support the entire detector.

The gain of the PMTs is defined as the number of electrons collected at the anode per electron emitted at the photocathode. By adjusting the voltages on the dynodes the PMT gain was set to 2.5×10^7 for the measurements presented in Chapter 6 of this thesis.
The quantum efficiency, the probability of a photon, that reaches the photocathode, to undergo the photoelectric effect and produce a free electron, depends on the wavelength. The quantum efficiency of the Hamamatsu R5912-02MOD PMTs is maximal for wavelengths around 420 nm. As photons in the VUV range are absorbed by the PMT glass, the argon scintillation light, whose spectrum is peaked at 128 nm, has to be shifted towards longer wavelengths. For this purpose the PMTs and the reflector foils are coated with Tetraphenyl butadiene (TPB, IUPAC name: 1,1,4,4-tetraphenyl-1,3-butadiene). TPB is an organic chemical compound used as wavelength shifter. It absorbs light in the UV range and emits light in the visible range by fluorescence. Its re-emission spectrum is peaked around 420 nm [66, 67] and thus matches well the sensitive region of the bialkali photocathode. The fluorescence decay time of TPB is of the order of 1 ns [68]. The coating of the PMTs and the reflector foils with TPB was done by evaporation [69]. Figure 2.4 shows the array of 14 PMTs illuminated by day light and by UV light, demonstrating the fluorescence of the TPB.

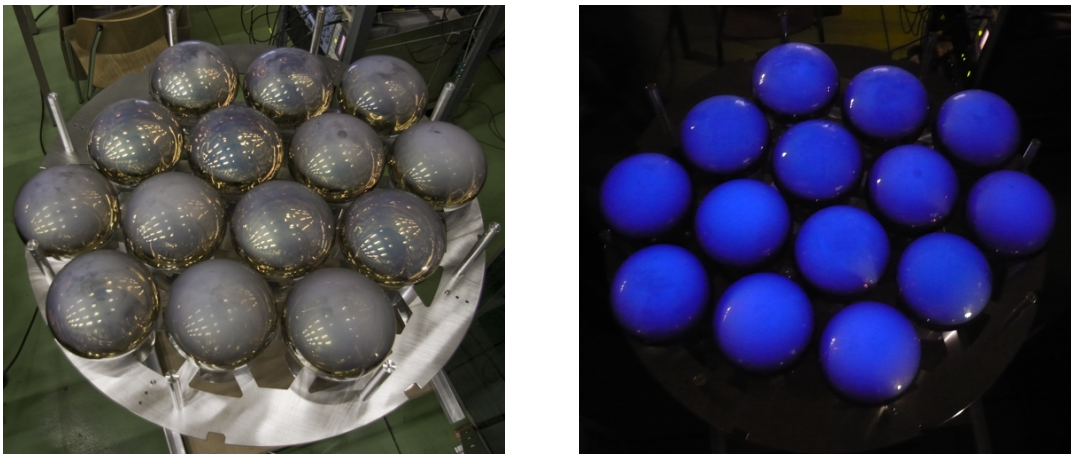

Figure 2.4: Bottom PMT array illuminated by day light (left) and by UV light (right) before the installation in the detector.

The reflector foils, which define the cylinder barrel of the active volume, consist of 254 μm thick white Tetratex®[2] membranes mounted on polyester foils[3] giving the reflectors a metallic luster which can be seen in Figure 2.3c. The polyester foils serve as mechanical support for the Tetratex® foils and reflect light produced outside the active volume. Tetratex® is a polytetrafluoroethylene, which reflects the incident light diffusely. To increase the wavelength shifting efficiency in the detector not only the PMTs but also the Tetratex® foils have been coated with TPB: 1 mg/cm^2 of TPB has been evaporated on the reflectors.

2.3.2 Charge Readout System

Two different charge readout systems can be implemented in the ArDM detector:

- a second array of PMTs to detect the proportional scintillation light produced by the electrons drifting in the gas phase or
- a double-stage LEM with a two-dimensional readout anode for multiplying and detecting the electrons.

Both alternatives are briefly described in this section.

Top PMT array
For the top PMT array in the argon gas phase, the Hamamatsu R5912-02MOD, the same PMTs as for the bottom array detecting the primary scintillation light, were chosen. They will also be coated with TPB by evaporation and installed on PCB bases which provide all the electrical connections. The PMTs will be fixed to a steel frame similar to the one of the bottom PMTs. Presumably, the top PMT array will be installed in the ArDM detector for a first operational phase in Canfranc and will later be replaced by the double-stage LEM with a two-dimensional readout anode.

Double-stage LEM with a two-dimensional readout anode
The development of the LEM for the ArDM experiment is in progress. Extensive studies were made with a small LEM with an active area of 10 cm $\times$ 10 cm in a dedicated setup [70]. The epoxy plate of the tested LEM has a thickness of 1.0 mm. The LEM holes have a diameter of 500 μm and the distance between them is 800 μm. To avoid oxidation, the copper layer of the LEM was gold plated. In total, the metal coating is 30 μm thick. Figure 2.5 shows a picture of the tested LEM and a close up view of the LEM holes.

The electron avalanche produced in the LEM holes is detected with a two-dimensional readout anode installed above the LEM. The anode consists of two sets of orthogonal copper strips on top of each other, which are separated by an insulating foil. It provides two independent readout views. To distribute the collected charge equally between the two sets of electrodes, the lower strips, facing the LEM, have to be thinner than the upper ones. The width of the lower and the upper strips is 120 and 500 μm, respectively [70]. The geometry of the anode allows to reconstruct the position of an interaction in the x-y-plane, defined as the plane perpendicular to the drift direction of the electrons. The z-position, the position along the drift direction, is determined by the drift time of the electrons. As the fast component of the scintillation light is instantaneous, the drift time is given by the time difference between the light and the charge signal $t_{\text{charge}} - t_{\text{light}}$. Thus, the drift distance d, indicating the z-position of the interaction, is

$$d = v_{\text{d}} \left(t_{\text{charge}} - t_{\text{light}} \right), \tag{2.19}$$

[2] Donaldson, Tetratex® ePTFE membrane
[3] 3M Vikuiti™ Enhanced Specular Reflector Film (ESR)

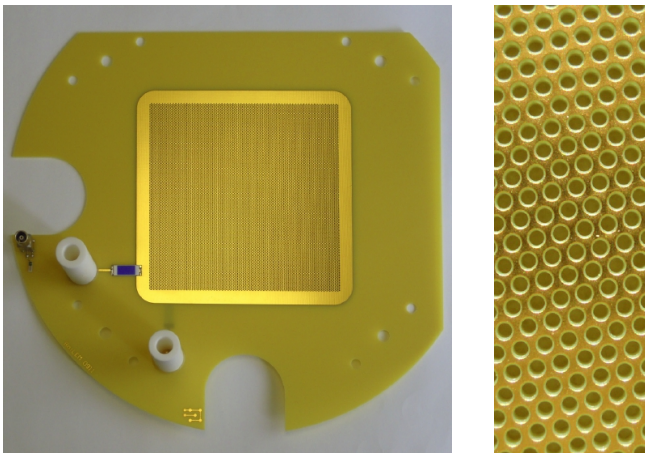

Figure 2.5: LEM prototype with an active area of 10 cm × 10 cm (left) and close up view of the LEM holes (right). The pictures are taken from [70].

where v_d is the drift velocity of the electrons. As described in Section 2.1 the drift velocity depends on the electric field strength and the temperature and can be described by Equation (2.8).

The effective gain of the LEM setup was measured. The effective gain does not only take into account the gain of the LEM but also the efficiency of the charge extraction at the liquid surface and the transparencies of the extraction grids and the LEM. These effects can not be measured separately. The highest effective gain measured with the setup described above is 27. It was reached with a voltage of 3.55 kV across the LEM [70].

Due to the very low recoil energies expected from WIMP interactions, for the ArDM LEM a higher effective gain is needed, than reached with the tested setup. To estimate the effective gain required for dark matter search, we assume here that the lower limit for the signal to noise ratio allowed by the analysis is 10. In Reference [70] it is shown that the typical noise of the charge readout is equivalent to the amplitude of the signal of about 1250 electrons. Thus, a minimum of 12 500 electrons should reach the anode after a WIMP scattered on an argon nucleus.

The exact amount of ionisation charge produced by nuclear recoils in liquid argon has not been measured for the energies and electric fields which are considered here. The WARP collaboration measured the fraction of proportional over primary scintillation light S_2/S_1 as a function of the ratio $I_1/(I_1 + I_3)$ [71], where I_1 and I_3 are the intensities of the singlet and the triplet components of the scintillation light. This data can be used to roughly estimate the number of electrons produced by nuclear recoils. The measurement shows that for an electric field strength of 1 kV/cm and for energies equivalent to nuclear recoil energies of 40 – 60 keV the ratio S_2/S_1 is about 10 times higher for electronic recoils than for nuclear recoils. That means, that nuclear recoil events produced 10 times less ionisation charge than electronic recoil events, which generate the same amount of light. To make use of this information, the scintillation efficiency L_{eff}, the ratio of the scintillation light yield for nuclear events Y_{nr} over the scintillation light yield for electronic recoil events Y_e, has to be estimated for an electric field of 1 kV/cm.

As reported in Section 2.1, L_{eff} was measured to be about 0.25 for nuclear recoil energies up to 250 keV in the absence of an electric field [50, 51]. The presence of an electric field is expected to increase L_{eff}, because for high LET the electrons recombine faster than for low LET

and thus Y_e is presumably more affected by the electric field [52]. By measuring the ratio of the scintillation light to the collected ionisation charge for ∼1 MeV electrons and extrapolating it to infinite electric field strengths, the fraction of scintillation light produced by self-trapped exciton luminescence in absence of an electric field could be estimated to be about 30% [44]. Thus, without electric field about 70% of the scintillation light is due to recombination luminescence. If an electric field is applied a fraction of the electrons escapes recombination and the recombination luminescence part of the scintillation light is reduced. At an electric field of 1 kV/cm the total scintillation light yield for electronic recoil events Y_e is reduced to about 55% of the value without electric field [44]. Assuming that Y_{nr} is not affected by the electric field, L_{eff} is about 0.45 for an electric field of 1 kV/cm. Thus, a nuclear recoil of 30 keV produces the same amount of light as an electronic recoil event of 13 keV.

An electron of this energy has a stopping power of the order of 20 MeV/cm [72]. The fraction R of electrons escaping recombination can be calculated with Equation (2.7). For a stopping power of 20 MeV/cm and an electric field of 1 kV/cm, R is about 0.47. The average energy to produce an electron ion pair in liquid argon is 23.6 eV [39]. Thus, a 13 keV electron produces about 200 electrons. As the stopping power increases when the electron slows down, the here evaluated number of produced electrons is rather overestimated.

This very rough estimation shows that a nuclear recoil of 30 keV produces less than 20 electrons. Thus, an effective gain of more than 600 is required for dark matter search. If only 10 electrons are produced, the gain has to be even higher than 1200. A more detailed description of this estimation can be found in [70].
A possibility to reach such a high gain is to use two LEM plates on top of each other forming a so-called double-stage LEM. In a double-stage LEM the electrons multiplied in the lower LEM would undergo a second multiplication in the upper LEM.

Another research project is the production of a LEM of bigger size. The LEM for ArDM should have a diameter of 80 cm, which corresponds to the diameter of the active volume. The scalability of the LEM technology has been proven with the operation of a LEM and a two dimensional readout anode with an active area of 40 cm × 80 cm, as described in References [70, 73]. The 40 cm × 80 cm LEM was tested in the ArDM detector vessel using the entire cryogenic system of ArDM. Very clear tracks could be recorded. As an example, a track of a cosmic muon emitting δ rays is presented in Figure 2.6. Delta rays are electrons, which are produced by ionisation of argon atoms and have enough energy to ionise further argon atoms on their own. The figure shows, for the x- and the y-view, the channel number versus the drift time. The grey scale indicates the signal amplitude. The gaps in the track are caused by the

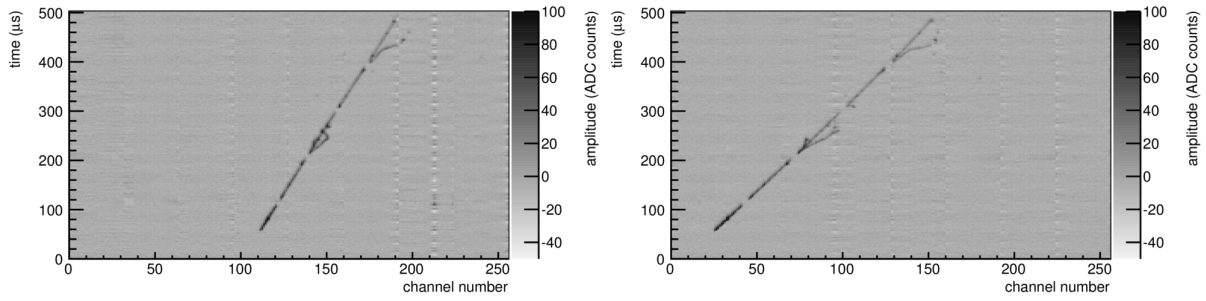

Figure 2.6: Track of a cosmic muon emitting δ rays recorded with a LEM and a two dimensional readout anode with an active area of 40 cm × 80 cm. The figure is taken from [70].

division of the LEM into several sectors. The LEM is sub-divided to ensure, that a short circuit in one of the holes affects only the particular sector, but not the entire LEM. On the edges of the sectors the charge is not multiplied.
The evaluation of the effective gain of the tested LEM setup is still ongoing. A signal to noise ratio of about 30 could be reached for minimum ionising particles [70].

2.3.3 High Voltage Generator

The electric drift field in the ArDM detector is generated by a Greinacher high-voltage multiplier [74], also known as Cockcroft-Walton high-voltage multiplier [75]. The Greinacher high-voltage multiplier is a circuit that converts low AC input voltages into high DC output voltages. It consists of a chain of capacitors and diodes and can be composed of a variable number of equal stages. Each stage consists of two capacitors and two diodes. The arrangement of the capacitors and diodes is shown in Figure 2.7. The Greinacher circuit is charged up by an AC voltage source. The upper row of the capacitors in Figure 2.7 are called charging capacitors C_c. They are charged during one half of the AC period and discharged during the second half of the AC period. In contrast, the lower row of capacitors is only charged during the first half of the AC period, while during the second half of the AC period the diodes prevent them from discharging. The lower capacitors store the transferred charge and are thus called storing capacitors C_s. Ideally, the voltage across each storing capacitor reaches the peak-to-peak value of the AC input voltage V_pp, if the Greinacher circuit is fully charged. The potential at the nth stage of the Greinacher circuit is thus $V_n = nV_\mathrm{pp}$. The sign of the output voltage is determined by the polarity of the diodes. In Figure 2.7 the output voltage is negative. For a positive output voltage the polarity of all the diodes has to be reversed. The charging mechanism of the Greinacher circuit is described in more detail in Reference [76].

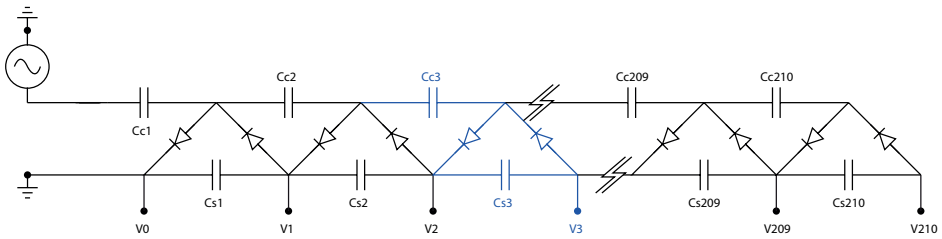

Figure 2.7: Diagram of a Greinacher circuit with 210 stages. One stage consists of two capacitor symbols (C_c and C_s) and two diode symbols. The structure of one stage is shown by means of the third stage sketched in blue. The figure is slightly modified from [77].

The ArDM Greinacher circuit consists of 210 stages. The stages 1 to 170 consist of eight 82 nF polypropylene capacitors[4] and six diodes[5] each. For these stages every capacitor symbol in Figure 2.7 stands for four capacitors connected in parallel, every diode symbol for three diodes connected in series. For the stages 171 to 210 the number of diodes stays the same, but the number of capacitors per stage is reduced to two charging capacitors and two storing capacitors. The Greinacher circuit is installed inside the detector vessel and connected to the field shaping electrodes. The last stage is connected to the cathode. Figure 2.8 shows the Greinacher circuit installed on the ArDM detector. The blue components are the polypropylene capacitors. When the detector is operated, all the stages are completely immersed in liquid argon. Liquid argon is a good insulator. Its dielectric strength is of the order of 1 MV/cm [78]. Thus, immersing the

[4]KEMET Electronics S.A., Evox Rifa PHE450
[5]Philips Semiconductors, BY505

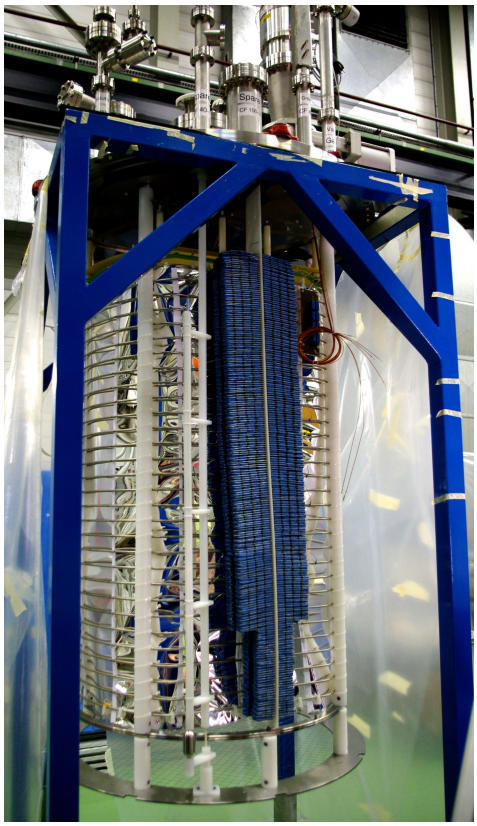

Figure 2.8: The ArDM detector during the assembling. The Greinacher circuit (blue) and its discharging system are shown.

circuit in liquid argon reduces the possibility of an electrical breakdown. A detailed description of the ArDM Greinacher circuit can be found in References [77, 79].
The ArDM Greinacher circuit is charged up by an AC power supply, which was specially developed for this purpose and is described in Section 4.6. It provides an AC output voltage with a peak-to-peak value up to 2.7 kV, a maximum current of 10 mA (r.m.s.) and a fixed frequency of 50 Hz.

Under real conditions the output voltage of the Greinacher circuit is not equal to the peak-to-peak value of the input voltage times the number of stages, but it is reduced due to the capacitances of the diodes and stray capacitances. As a uniform electric field is important for the drift of the electrons, this non-linearity has to be compensated. In order to get a uniform drift field, the stages, which are connected to a field shaping electrode, are chosen in such a way, that the potential difference between two consecutive electrodes is constant.

Although the ArDM Greinacher circuit is designed to generate up to -400 kV, it will be operated at -120 kV to generate an electric drift field of 1 kV/cm. The potential of the whole circuit is shifted by -4 kV by adding a DC voltage source. This shift allows to apply a voltage of -4 kV to the lower extraction grid. The electric field between the two extraction grids is then 4 kV/cm and allows the extraction of the drifting electrons to the vapour phase. In September 2010 the Greinacher circuit was operated successfully in liquid argon up to -70 kV, which corresponds to a drift field of about 0.6 kV/cm.

The Greinacher circuit is designed to store the charge also if the AC voltage source is switched off. Thus, after operation the Greinacher circuit has to be discharged before emptying the

detector vessel. For this purpose a discharge system was developed. The whole circuit can be discharged through a grounded resistor chain by touching the cathode with an oval stainless steel contact. The resistor chain consists of nine 200 MΩ high voltage resistors connected in series. The discharging system is brought into contact with the cathode by rotating the oval contact around a polyethylene rod. The rotation can be performed using a rotary motion vacuum feed through on the top flange of the detector vessel. The oval stainless steel contact and the polyethylene rod are shown in Figure 2.8 beside the Greinacher circuit. The discharging system has also been tested in September 2010 and worked properly.

2.4 The Cryogenic System

2.4.1 Overview of the Cryogenic System

The ArDM detector is housed in a detector vessel filled with almost two tons of liquid argon. As mentioned in Section 2.1 the purity of the liquid argon is very important, because impurities can de-excite argon excimers non-radiatively or reduce the amount of drifting electrons. Thus, the purification of the liquid argon is essential. As the attachment cross section of the electrons is bigger for O_2 than for other impurities, such as N_2 and CO_2, the cryogenic system of ArDM includes a purification cartridge filled with Cu that filters the oxygen out of the argon. The purification cartridge is located outside the detector vessel. Two stainless steel tubes connect it to the detector vessel. A custom-made membrane pump circulates the liquid argon from the detector vessel to the purification cartridge and back to the detector vessel.
Additionally, the argon gas at the top of the detector is purified in a second purification cartridge, that filters not only O_2, but also other impurities such as N_2 and CO_2, out of the argon.

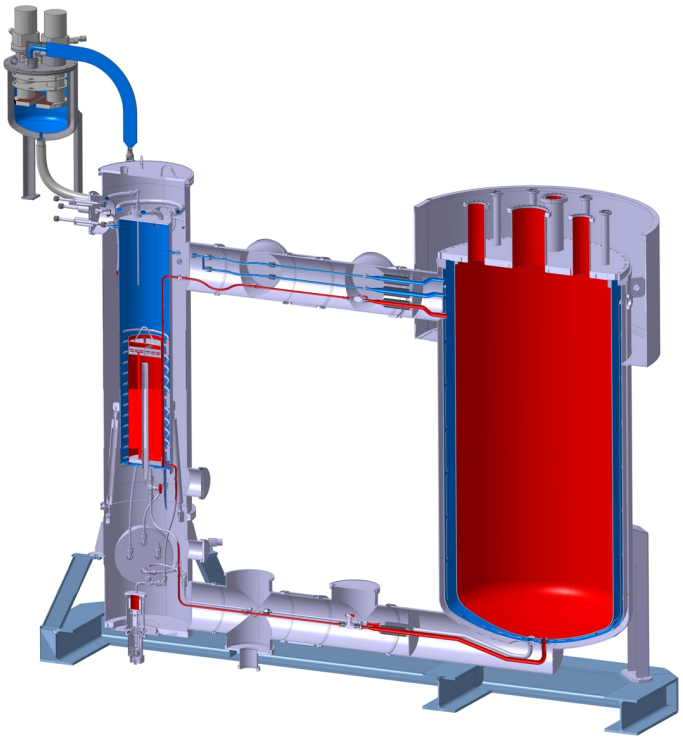

Figure 2.9: Vertical section through the cryogenic system. The detector vessel is shown on the right, the liquid argon purification cartridge and the condenser unit on the left side. The pure liquid argon circuit and the liquid argon bath are marked in red and in blue, respectively.

The ArDM detector vessel is surrounded by a jacket of liquid argon. This jacket belongs to a second argon circuit, called the liquid argon bath. The function of the liquid argon bath is to cool the detector vessel. Also the purification cartridge is completely surrounded and cooled by the argon bath. As in the pure liquid argon circuit, which contains the ArDM detector, the two parts of the liquid argon bath are connected with stainless steel tubes. The total volume of the liquid argon bath is about 200 l.
While cooling the closed pure liquid argon circuit, the liquid argon in the bath continuously evaporates. During the first four test runs the cryogenic system was operated with the bath open to the atmosphere and the evaporated argon was automatically refilled, when the liquid level reached a critical height. In spring 2011 the cryogenic system was upgraded with a condenser unit containing two Gifford-McMahon cryocoolers, which are described in more detail in Section 4.4. They have a total cooling power of 600 W at 80 K and turn the cryogenic system into a closed system. Two insulated cryogenic lines connect the condenser unit to the liquid argon bath.

All the components containing liquid argon are enclosed by a stainless steel shell, which is evacuated for thermal insulation. By continuous pumping the pressure in the vacuum insulation is kept below 10^{-4} mbar. The vacuum insulation is divided into two volumes. Vacuum insulation 1 surrounds the detector vessel, while vacuum insulation 2 reduces the heat input to the purification cartridge and the tubes connecting it to the detector vessel. Figure 2.9 gives an overview of the cryogenic system. It shows a vertical section through the setup. The pure liquid argon circuit and the liquid argon bath are marked in red and in blue, respectively.

The cryogenic system is permanently monitored and regulated by the ArDM control system, which is extensively described in Chapter 4. It controls all the vacuum and cryogenic processes, such as the operation of the vacuum pumps, the cooling of the liquid argon or the recirculation of the pure liquid argon circuit.

2.4.2 Argon Purification Systems

In the ArDM detector the drifting electrons have to cover remarkable distances up to 120 cm. To avoid losing too many electrons due to attachment to impurities, such as O_2, N_2 or CO_2, very high purity argon is needed. The oxygen equivalent concentration $[O_2]_{eq}$ has to be below 1 ppb, to drift electrons over such long distances. Thus, purification of the argon in the detector vessel is essential.
Two independent purification systems are included in the ArDM experiment. One purification system filters the oxygen out of the liquid argon, the other one purifies the argon vapour. They are called liquid argon and argon gas purification systems. Both purification systems are described in this section.

Liquid Argon Purification System

As the attachment cross section of electrons to O_2 is about two orders of magnitude bigger than the cross section for attachment to other impurities, such as N_2 or CO_2, it is particularly important to filter the O_2 out of the argon in the ArDM detector. Thus, the liquid argon purification system is based on a cartridge filled with copper powder. Oxygen molecules passing the cartridge oxidise the copper and get trapped. As the copper powder is very reactive and would react strongly with the oxygen in the air, the cartridge had to be filled with cupric oxide (CuO) powder. Before operation the cupric oxide had to be reduced by the reaction

$$CuO + H_2 \longrightarrow Cu + H_2O. \tag{2.20}$$

For this purpose the cartridge was flushed with an argon-hydrogen mixture and heated up to about 200 °C in order to provide the activation energy for the reaction. After the reduction, the cartridge was closed airtight and only opened before filling with argon.

A custom-made membrane pump circulates the liquid argon through the purification system. A piston moves the membrane of the pump and thus expands and contracts the volume of the pump. When the volume is expanded, liquid argon flows through the input valve into the pump. The contraction of the pump pushes the liquid out through the output valve. The input and output valves of the pump are check valves which prevent the liquid argon from flowing against the circulation direction. The piston is moved pneumatically by the ArDM control system. The control of the membrane pump is described in Section 4.5.

The pump was tested during several test runs of the ArDM cryogenic system. The functionality of the purification cartridge was proven and the circulation speed was measured to be of the order of 10 l/h [80]. Although the control of the pump worked perfectly, the pump could not be operated as stable as needed for a dark matter run lasting several weeks. Thus, it might be replaced for future underground operation.

Argon Gas Purification System
In addition to the liquid argon purification system the ArDM experiment includes a second, completely independent purification system, that filters impurities out of the argon vapour phase at the top of the detector. A double membrane pump[6] circulates the argon through a purification cartridge[7], which filters not only O_2, but also H_2O and CO_2 out of the argon. The maximum flow through the double membrane pump is 250 l/min at standard temperature and pressure (STP). After purification the argon gas is condensed in a helix inserted in the liquid argon bath and then it flows back to the detector vessel. The gas flow is measured and regulated with a high flow thermal mass flow controller[8]. The pump and the flow controller are integrated in the ArDM control system, which also monitors temperature and pressure in the gas purification system. All the processes to control the gas purification system and a precise description of the system can be found in Section 4.5.

2.5 Background Radiation

The commissioning of the cryogenic system and the control system as well as tests of the bottom PMT array were performed on the surface at CERN. The small WIMP-nucleon cross section predicted by the experimental limits summarised in Section 1.2 requires very little background radiation or the capability to distinguish background events from WIMP events. Thus, the ArDM experiment will be operated in the Canfranc Underground Laboratory (Laboratorio Subterráneo de Canfranc, LSC) in the Pyrenees, which provides good shielding from cosmic muons and a low background environment.

In the Canfranc Underground Laboratory two different types of background radiation are expected:

- β and γ radiation, mainly caused by the isotope ^{39}Ar and radioactive contaminations of the detector material, and

[6] KNF, N 0150.1.2.AN.12
[7] SAES Pure Gas Inc., MC4500
[8] MKS Instruments, MC20 ALTA mass flow controller

- neutrons, mainly caused by radioactive contaminations of the detector material and the rock surrounding the experiment.

The neutrons produce nuclear recoil events in the ArDM detector, which are difficult to distinguish from WIMP events. In contrast to the neutrons, two different discrimination criteria exist for the β and γ radiation:

- pulse shape discrimination and
- the ratio of the amount of ionisation charge over the amount of scintillation light produced by an event.

The mechanisms which underlie these two discrimination criteria are discussed in Section 2.1. A more detailed overview of the different background types and expected background rates in the Canfranc Underground Laboratory is given in Section 6.7. A first estimation of the rejection power from the pulse shape discrimination can be found in Section 6.8.

Chapter 3

Development of Temperature and Liquid Argon Level Measurement for the ArDM Control System

As described in Chapter 2 the pure liquid argon circuit and the liquid argon bath can contain together up to 1600 l of liquid argon. At the normal boiling point the volume of argon gas is 241 times bigger than the volume of the same mass of liquid argon [38]. Thus, the evaporation of only a small fraction of the liquid argon enclosed in ArDM would lead to a dangerous pressure increase. Hence, a continuous observation of the cryogenic system of ArDM is required. The cryogenic system is monitored by measuring the temperature, the pressure and the liquid level in the pure liquid argon circuit and in the liquid argon bath.

The sensors monitoring the cryogenic system have to be suitable for operation in vacuum and at cryogenic temperatures. To satisfy these requirements self-made sensors, readout devices and installation methods for the temperature and liquid level measurement were developed for ArDM.
Underground operation of the ArDM experiment necessitates a control system which does not only monitor the experiment but also actively regulates the vacuum system, the cryogenic system and the high voltage system. For this reason, after three test runs on the surface, ArDM has been upgraded with a control system based on a programmable logic controller (PLC) that allows for process control. All the temperature sensors and self-made level meters described in this chapter were integrated into the ArDM control system which is presented in Chapter 4. For monitoring the pressure of the cryogenic system commercial piezoresistive silicium pressure sensors were used before and after the commissioning of the ArDM control system. These sensors and their integration into the ArDM control system are also described in Chapter 4.

3.1 Temperature Measurement

The temperatures of the liquid argon circuits are measured with Pt10k platinum temperature sensors[1]. One of these sensors is shown in Figure 3.1. They are thin film sensors deposited on a ceramic substrate. The dimensions of the substrate are 5 mm × 2 mm × 1.05 mm. According to the DIN EN 60751 standard the electrical resistance of the platinum sensors depends on the temperature as

$$R(T) = R_0 \cdot (1 + A \cdot T + B \cdot T^2 + C \cdot T^3 + D \cdot T^4) \tag{3.1}$$

[1] IST AG, P10K.520.4W.B.015.D

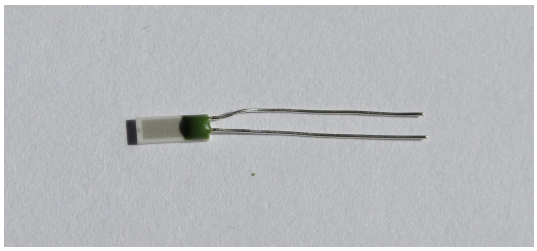

Figure 3.1: Pt10k temperature sensor before installation in the cryogenic system. The thin film sensor is deposited on a ceramic substrate. The dimensions of the ceramic substrate are 5 mm × 2 mm × 1.05 mm.

for temperatures from -200 °C to 0 °C and

$$R(T) = R_0 \cdot (1 + A \cdot T + B \cdot T^2) \tag{3.2}$$

for temperatures between 0 °C and 400 °C, where $A = 3.9083{\cdot}10^{-3}$ °C^{-1}, $B = -5.775{\cdot}10^{-7}$ °C^{-2}, $C = 4.183 \cdot 10^{-10}$ °C^{-3}, $D = -4.183 \cdot 10^{-12}$ °C^{-4}, $R_0 = 10$ kΩ is the resistance of the sensors at 0°C and T is the temperature in °C.

The Pt10k sensors are of the tolerance class B according to the DIN EN 60751 standard. The deviation limit of sensors of this tolerance class is ± (0.3°C + 0.005·|T|). The resistances of the sensors are measured with the two-point method. A readout device, which was designed and built at ETH Zurich, supplies the sensors with a constant current of 100 μA and measures the voltage drop across the platinum resistances. For the first three test runs of ArDM on the surface, the output signals of the readout device were sent via a USB interface to a computer where they were processed by a LabVIEW program. The processed data were stored in a MySQL database.

In total 41 Pt10k sensors are installed in ArDM to survey the experiment. They give a good overview of the temperature distribution in ArDM and are essential for understanding the behaviour of the argon in the experiment, in particular during the filling of the detector vessel. The positions of the temperature sensors are shown in Figure 3.2. Twelve out of the total of 41 Pt10k sensors are mounted directly in the liquid argon, measuring the temperature in the detector vessel (TE 00 – 09) and in the bath around the liquid purification cartridge (TE 20, 21). The 3 Pt10k sensors monitoring the gas purification system (TE 39 – 41) are installed inside the tubes of the system so that they measure directly the temperature of the argon gas. All the remaining Pt10k sensors are mounted on stainless steel surfaces, such as the tubes of the liquid argon circuits (TE 10, 14 – 19, 29 – 38), which connect the detector vessel with the purification system, and the cylindrical vessel of the bath around the liquid purification cartridge (TE 11 – 13).

To ensure a good thermal contact between the Pt10k sensors and the argon, the sensors are glued with STYCAST[2] on the stainless steel surfaces. STYCAST 2850 FT is a two-component epoxy adhesive with a high thermal conductivity $\lambda = 1.119$ W/(m·K). Furthermore, it is a good electrical insulator (dielectric constant $\epsilon = 6.4$).
In order to protect the fragile sensors on tubes with small radii from mechanical stress, a special holder was developed. The Pt10k sensors are glued into a small anticorodal block of the shape of a half cylinder barrel, whose inner surface fits exactly on the tube. The anticorodal, an

[2]Emerson & Cuming, STYCAST 2850 FT

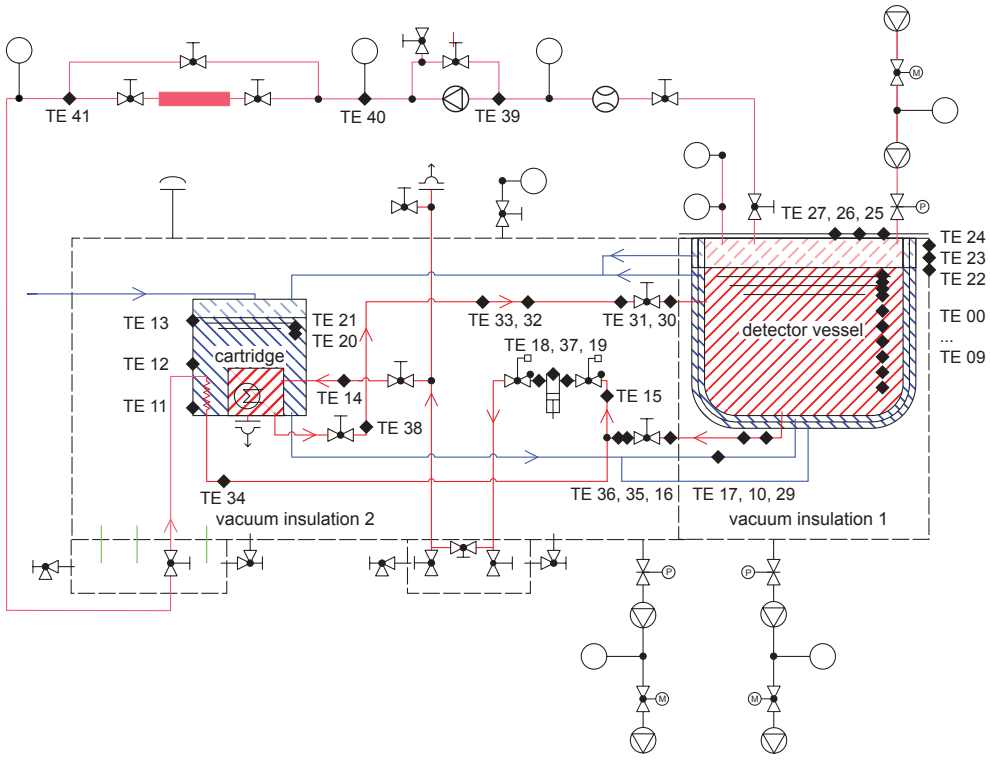

Figure 3.2: Positions of the Pt10k temperature sensors. All these sensors were integrated into the ArDM control system. The red (from bottom left to top right) hatched circuit is the pure liquid argon circuit, the blue (from bottom right to top left) hatched circuit is the liquid argon bath. The areas hatched with solid lines symbolise the liquid argon, the areas hatched with dashed lines symbolise the argon gas.

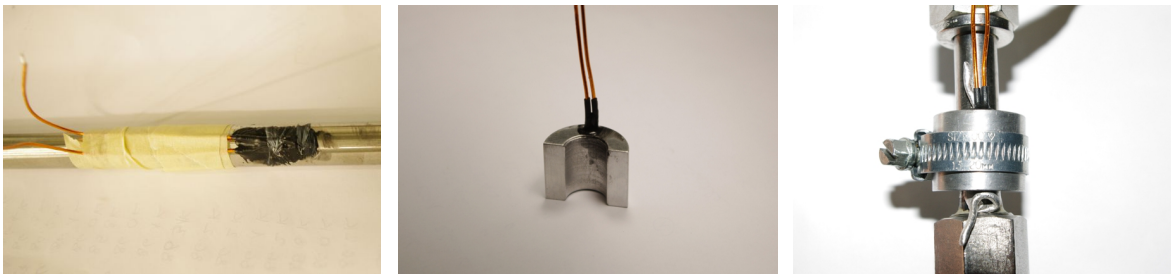

Figure 3.3: Methods for fixing Pt10k temperature sensors on tubes: Pt10k sensor glued with STYCAST on a tube (left), special holder for Pt10k sensor (center) and holder for Pt10k sensor fixed to a tube with a metal clamp (right).

aluminium alloy, and a thin layer of indium between the holder and the tube ensure a good thermal contact between the sensor and the tube. Two of the holders for the Pt10k sensors are shown in Figure 3.3.

In spring 2009, when the ArDM detector was filled for the first time with liquid argon, all the Pt10k temperature sensors were tested at liquid argon temperature. Figure 3.4 shows the temperature profile during the whole run monitored by the 10 temperature sensors in the detector TE 00 to TE 09 (from top to bottom). All the temperature sensors worked well and

clearly indicated the filling of the liquid argon bath on April 24, the following cool down of the evacuated detector, the sudden temperature decrease when the detector was filled with argon gas on April 27, the filling of the detector with liquid argon in two steps on April 30 and May 7 and the warm-up phase starting on May 22.

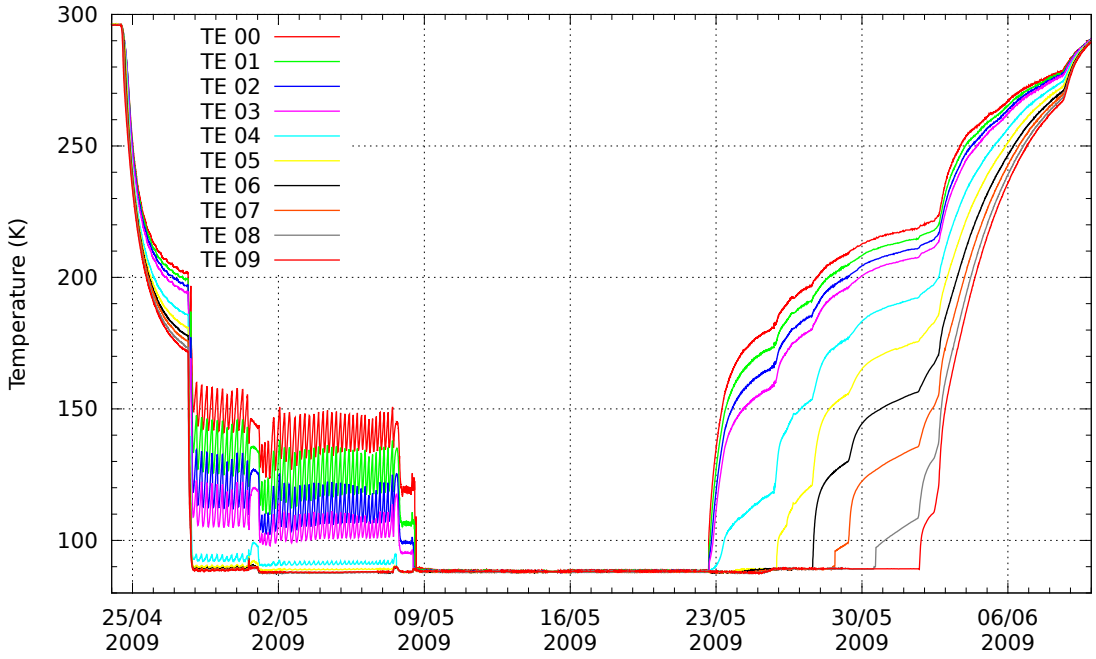

Figure 3.4: Temperature profile in the detector during the test run on the surface in spring 2009. All the temperature sensors in the detector (TE 00 – TE 09) worked well in liquid argon.

3.2 Measurement of the Liquid Argon Level

3.2.1 Level Meters

The liquid argon level in the detector vessel and in the liquid argon bath is measured with a commercial and four self-made capacitive level meters. In the liquid argon bath two cylindrical level meters are installed. A commercial one with a measuring length of only 30 cm and a self-made one (LE 00 in Figure 3.5 and Table 3.1) covering the entire height of the liquid argon bath around the cartridge. The commercial cylindrical level meter is part of a liquid level controller[3] which also includes an electromagnetic valve that allows the automatic refilling of the liquid argon bath. The valve is opened if the liquid level falls below a first set-point and closed if it exceeds a second set-point. In Figure 3.6 the resulting refilling cycles are shown. The level is indicated in % of the measuring length of the commercial level meter. The change of slope at around 60 % is due to argon which evaporates in the inlet line when the filling is stopped and then enters the bath as warm gas when the valve is re-opened. This warm gas accelerates the evaporation in the bath for a short time.
The two cryocoolers installed in spring 2011 superseded the liquid level controller which therefore was not included in the ArDM control system.

The self-made cylindrical level meter (LE 00) has a measuring length of 1370 mm and consists of three concentric tubes. The outermost tube acts as a shielding for the two inner tubes which

[3] American Magnetics Inc., Model 186 Liquid Level Controller

Name	Description	Type
LE 00	level meter in the liquid argon bath	self-made capacitive level meter
LE 02	level meter in the detector	self-made capacitive level meter
LE 03	level meter in the detector	self-made capacitive level meter
LE 04	level meter in the detector	self-made capacitive level meter

Table 3.1: Level meters for monitoring the cryogenic system. These sensors were integrated into the ArDM control system.

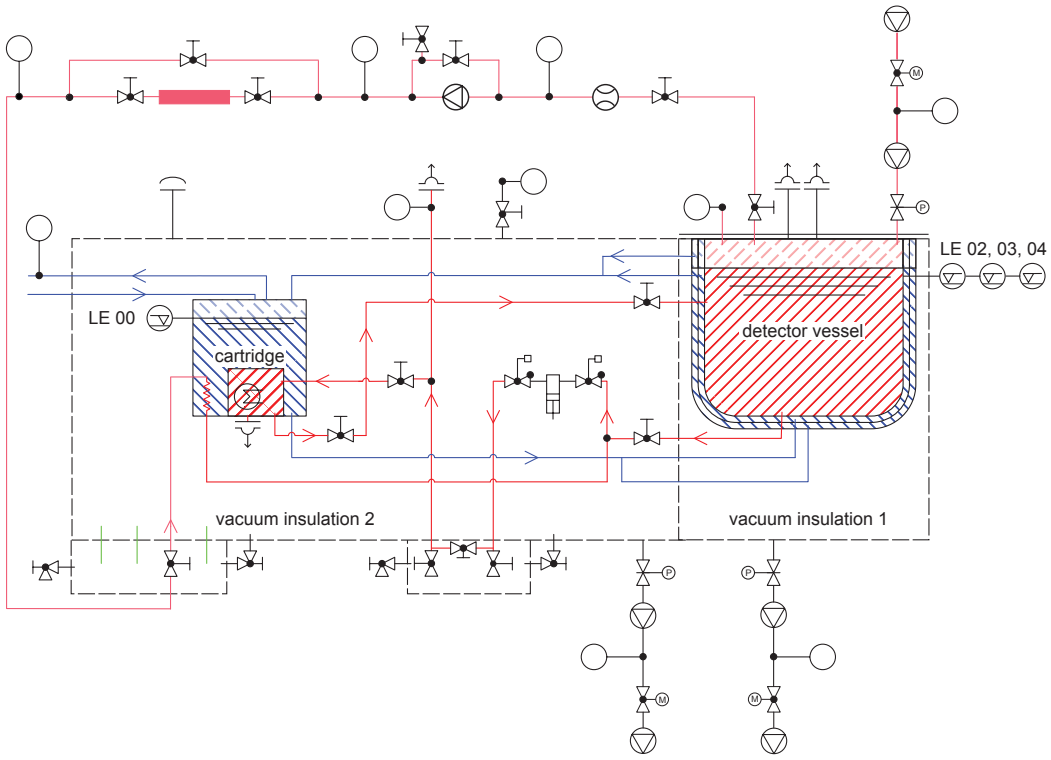

Figure 3.5: Positions of the level meters for monitoring the cryogenic system. These sensors were integrated into the ArDM control system.

form the capacitor. In the detector vessel three 20 mm high plate capacitors (LE 02, 03, 04 in Figure 3.5) are installed on the extraction grids. As there is no space for a long level meter covering the entire height of the detector vessel, the only indication of the level during the filling procedure is given by the temperature sensors TE 00 – TE 09. Each of the three plate capacitors is composed of 9 equally spaced plates which form a parallel circuit of 8 plate capacitors. The capacitance of one of these plate capacitors is very small and difficult to measure. In order to get a well measurable signal the capacitors are connected in parallel. As the self-made cylindrical capacitor, the 9 plates are shielded to reduce stray capacitances. All the self-made level meters were manufactured in the workshops of ETH Zurich. One of the plate level meters and the cylindrical level meter are shown in Figure 3.7.

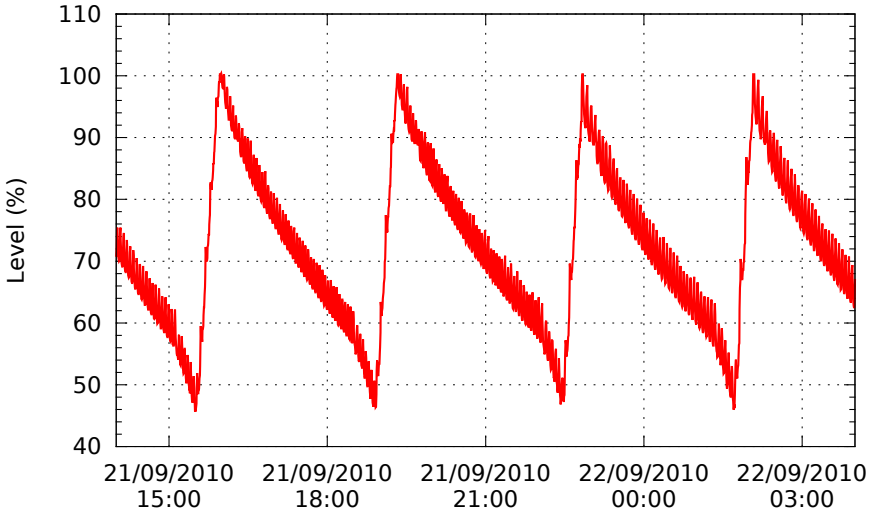

Figure 3.6: Level in the liquid argon bath in % of the measuring length of the commercial level meter showing the cycles of the automatic refilling of the liquid argon bath.

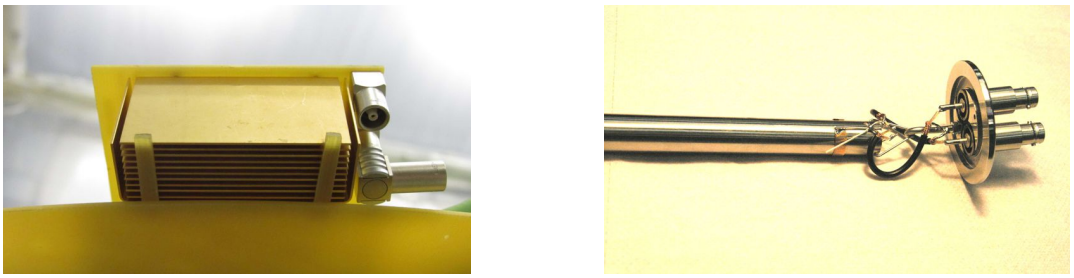

Figure 3.7: Self-made level meters: plate level meter (left) and detail of the cylindrical level meter with feed through (right).

The volume of all the capacitors can be filled with liquid argon. Since the dielectric constant of argon gas is different from the one of LAr, the capacitance of a level meter is a linear function of the percentage of the measuring length immersed in liquid argon. This allows to detect the liquid level by measuring the capacitance of the level meters. The dielectric constant of liquid argon at the normal boiling point is $\epsilon_{\mathrm{LAr}} = 1.496$ [38]. For argon gas the dielectric constant is given by the Clausius-Mosotti equation [81]

$$\frac{\epsilon - 1}{\epsilon + 2} = \frac{\rho}{M} \cdot \frac{4\pi N_{\mathrm{A}} \alpha}{3}, \tag{3.3}$$

which applies to nonpolar gases (gases without permanent dipole). The variable ϵ is the dielectric constant, ρ is the density, M is the molar mass, N_{A} is Avogadro's number and α is the molecular polarizability. As the density ρ of the argon gas at the normal boiling point is 5.774 kg/m^3 and the molecular polarizability α of argon is $1.6411 \cdot 10^{-24}$ cm^3 [38], the Clausius-Mosotti equation yields a dielectric constant of argon gas at the boiling point of $\epsilon_{\mathrm{GAr}} = 1.0018$.

The capacitance of the empty self-made cylindrical capacitor is 120 pF, the one of the empty plate capacitors is 65 pF. Taking into account the ratio $\frac{\epsilon_{\mathrm{LAr}}}{\epsilon_{\mathrm{GAr}}}$, the capacities of the full level

meters are expected to be 49% higher than the capacities of the empty level meters. This yields a sensitivity of 0.04 pF/mm for the cylindrical level meter and 1.61 pF/mm for the plate capacitors. The measured capacities of the full level meters are slightly smaller than expected. For the plate capacitors the measured difference between the capacitance of the empty and the full level meter is for example only 47%. This is due to spacers in the capacitors, which ensure the mechanical stability of the sensors, and other fixed capacitances. Therefore, a precise calibration of the level meters is essential.

3.2.2 Capacitance Meter

The capacities of the non-commercial sensors are measured with a self-made capacitance meter (Figure 3.8 (left)), which has the advantage to be almost insensitive to the capacitance of the cables connecting the sensors to the capacitance meter. Figure 3.8 (right) shows a schematic diagram of the capacitance meter. It measures the capacities by charging up the capacitors with a rectangular shaped current with constant amplitude I and variable period T. The amplitude of the current is

$$I = \frac{V_{\mathrm{cc}}}{2R_0}. \tag{3.4}$$

The position of the resistance R_0 is indicated in Figure 3.8 (right). During the first half period of the current signal the capacitor is charged up with the current $+I$ and the voltage U_C across the capacitor increases linearly with time. For the second half period the current is $-I$ and U_C decreases linearly with time. The period T is determined by the time it takes to increase U_C by a fixed potential difference ΔU and is thus proportional to the capacitance C:

$$T = \frac{2C\Delta U}{I} = \frac{4CR_0\Delta U}{V_{\mathrm{cc}}}. \tag{3.5}$$

Figure 3.9 illustrates the behaviour of the current I and the voltage U_C. The potential difference ΔU is defined by the ratio of the resistances R_1 and R_2. For $R_1 = 4 \cdot R_2$ this difference amounts to $\Delta U = V_{\mathrm{cc}}/4$ and the period of the current is

$$T = R_0 C. \tag{3.6}$$

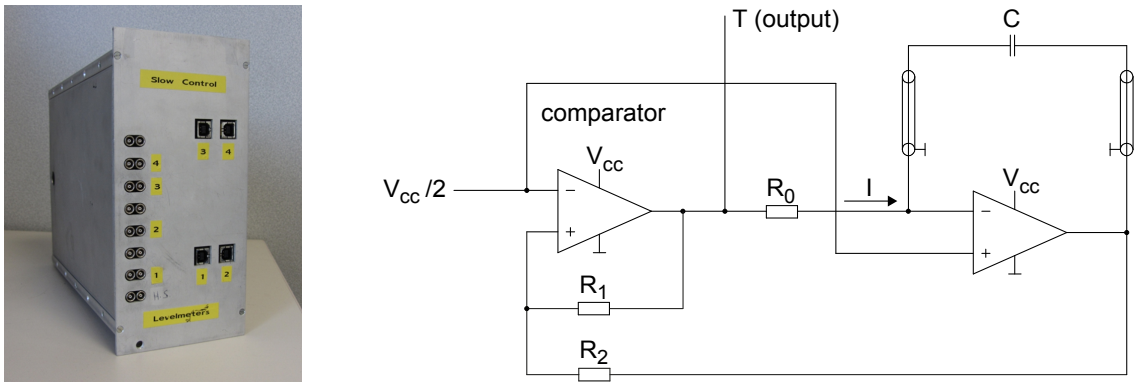

Figure 3.8: *Left*: Self-made capacitance meter with eight input channels and four output channels from the USB interfaces. *Right*: Schematic diagram of the capacitance meter. On the right the capacitive level meter C is charged up by the current I. On the left the comparator inverts the direction of the current I when the potential difference across the sensor reaches the value ΔU.

The measured period T is sent via a USB interface to a computer running a LabVIEW based program which calculates the liquid level from T. The liquid level data are stored in a MySQL database.

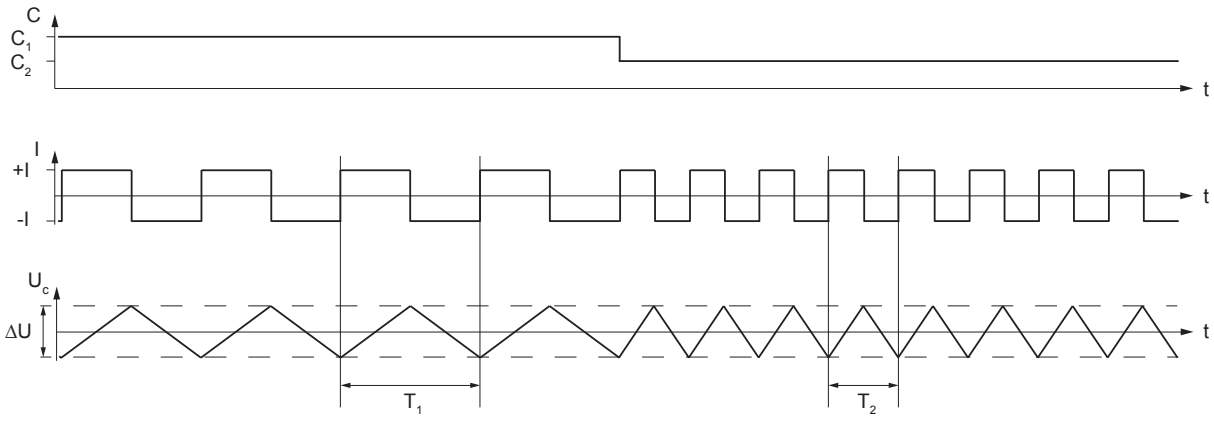

Figure 3.9: Schematic illustration of the current I charging up the capacitive level meters and the corresponding voltage U_C across the capacitors. The period of I and U_C is proportional to the capacitance C.

3.2.3 Measurement of the Heat Input to the Liquid Argon Bath

The level measurement allows to evaluate the evaporation rate of the liquid argon bath and thus the heat input to the bath. Figure 3.10 shows the heat input to the liquid argon bath during the test run in September 2010. For each refilling cycle the average evaporation rate was evaluated for the time interval between closing and opening of the valve. Then the heat input was calculated using the molar enthalpy of vaporisation at the normal boiling point $\Delta_{\text{vap}}H = 6.43$ kJ/mol and the liquid density at the normal boiling point $\rho = 1395$ kg/m^3 [38]. Three time intervals

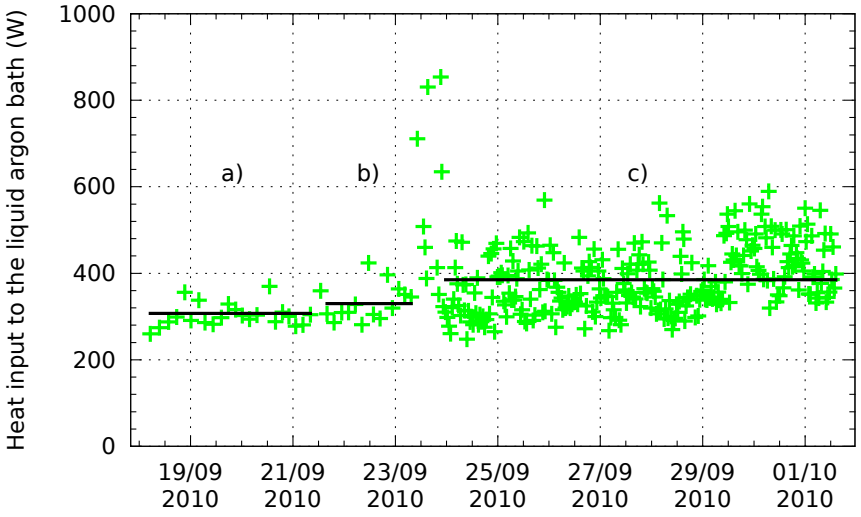

Figure 3.10: Heat input to the liquid argon bath calculated from the evaporation of the bath. For the time interval a) (1.0 bar of argon gas in detector) the average heat input is (307±5)W, for b) (half full detector) (330±11)W and for c) (full detector) (385±5)W. The data points above 600 W correspond to the heat input during the filling of the detector with liquid argon.

are visible in Figure 3.10: During the first few days of the run, only the bath was filled with liquid argon and the detector was filled with argon gas at 1.0 bar. In this interval a) the average heat input was (307±5)W. For the half full detector in time interval b) the average heat input was (330±11)W and for the full detector in interval c) it was (385±5)W. The heat input is not only defined by the condition of the detector but also by the temperature in the experimental hall. On 29/09/2010 the heating of the hall was turned on. This lead to a temperature rise of 4°C in the hall and consequently increased the heat input to the liquid argon bath by 70 W, what is clearly visible in Figure 3.10.
The same figure also shows data points above 600 W. They were recorded while the detector was filled with liquid argon and the stainless steel of the detector vessel as well as the top flange had to be cooled down. During the filling, the heat input to the liquid argon bath rose above 5000 W.

The data of the heat input to the bath presented here do not correspond to the total heat input of ArDM, since during the run in September 2010 the top flange has been cooled with the evaporated, but still cold argon from the exhaust of the bath. In Section 4.4 it is shown that the cooling power needed to keep the experiment at liquid argon temperature, exceeds the here calculated power of 385 W by more than 120 W.

Chapter 4

The ArDM Control System

After several test runs on the surface at CERN, the cryogenic system of the ArDM experiment has been moved to the Canfranc Underground Laboratory in February 2012. As soon as the ArDM detector will arrive at the Canfranc Underground Laboratory, background measurements and subsequent dark matter runs will be performed. The underground operation sets completely new requirements on the monitoring and control of the experiment. It necessitates a control system which does not only monitor the experiment, but also regulates actively the various subsystems of the experiment.

4.1 Design of the ArDM Control System

The main function of the ArDM control system is the monitoring of the condition of the ArDM detector and the regulation of the ArDM vacuum, cryogenics and high voltage systems in order to allow a save operation of the detector. In addition, the ArDM control system is a safety monitor that alerts people in case of an imminent danger, such as oxygen deficiency or fire.

The ArDM control system allows for process control and is based on a programmable logic controller (PLC). A PLC is a computer specially designed for process automation with a large number of inputs and outputs for sensors and actuators. PLCs possess a high reliability due to specialised hard- and software and therefore the ArDM control system serves as a safety system.

The core piece of the ArDM PLC is a high performance processor[1] with an execution time of less than 0.06 μs for one instruction [82]. It manages all input and output modules and a PCMCIA card for connecting to a CANopen network. The properties of the input and output modules are summarised in Tab. 4.1. The ArDM PLC reads out more than 100 sensors, most of them via interfaces which convert the signals provided by the sensors into signals accepted by the PLC. (See Table 4.1 for the signals accepted by the PLC.) Based on the data of the sensors and programmed processes, the PLC controls more than 50 actuators. It performs operations on demand and regulates the subsystems of the ArDM experiment automatically. The processor module also features an Ethernet connection that allows the communication with a supervisory computer on which the monitoring software is running.

The ArDM monitoring and control software is based on PVSS (Prozessvisualisierungs- und Steuerungssystem, process visualisation and control system) [83]. PVSS is a SCADA (supervisory control and data acquisition) system used by CERN. It includes a human-machine interface

[1] Schneider Electric Modicon Premium TSX P57 5634M

Type of module	Modicon Premium reference number	Number of modules	Channels per module	Accepted signals	Resolution
analog input	TSX AEY 1600	7	16	$0-10$ V/ $4-20$ mA	12 bit
analog output	TSX ASY 800	1	8	$0-10$ V/ $4-20$ mA	13 bit
digital input	TSX DEY 64D2K	1	64	0/24 V	
digital output	TSX DSY 64T2K	2	64	0/24 V	

Table 4.1: Properties of the input and output modules of the ArDM PLC [82].

(HMI), that allows the ArDM users to view the condition of the experiment and control the system manually via five user panels dedicated to the different subsystems of the ArDM detector. These panels are:

- The vacuum panel which is used for pressure monitoring in the vacuum insulations as well as for starting and stopping the vacuum pumps.
- The temperature panel that shows all the temperatures measured in the ArDM experiment.
- The cryogenics panel which gives an overview over the cryogenic system and allows the control of the argon purification systems.
- The cyocooler panel used for the control of the cooling system.
- The Greinacher circuit panel that allows the operation of the AC power supply unit for the Greinacher circuit.

PVSS also archives the data of the sensors and actuators for more than 2 months. The archived data can be displayed in PVSS and exported in a CSV (comma separated values) file. With the PVSS alarm management tool, threshold values for triggering an alarm can be set for all the sensors. The alarms can be sent via e-mail or text message. All the alarms are archived and displayed in an alarm list.

The PVSS data of the analog and digital inputs are backed up in a MySQL database for permanent storage. PVSS checks every 5 seconds for all the analog and digital inputs if the value has changed since the last entry to the database. Only if there is a change in value the new value is written to the database. Every 10 minutes all the active values are written to the database regardless of whether there was a change in value since the last entry or not. This selection of the stored data allows to reduce the used storage place. During the first 9 months of operation 7 GB of data have been stored in the MySQL database.

The ArDM control system is located in 7 standard 19" racks next to the ArDM detector together with the high voltage supply for the PMTs (HV rack in Fig. 4.1) and the data acquisition system (DAQ rack in Fig. 4.1). The PLC modules are installed in the PLC1 and PLC2 racks. The processor module and the analog input and output modules are in the PLC1 rack, the digital input and output modules are in the PLC2 rack. The INT1 and INT2 racks contain the

Figure 4.1: The seven standard 19" racks containing the ArDM control system (COM, PLC1, PLC2, INT1 and INT2 rack), the high voltage supply of the PMTs (HV rack) and the data acquisition system (DAQ rack).

interfaces for the sensors and actuators and displays for pressure and vacuum sensors whereas the COM rack contains the supervisory computer and its accessories.

For safety reasons every rack contains its own power distribution unit that provides the power for the entire rack and allows to cut the power of the complete rack with one single circuit breaker. The main power line of ArDM (three-phase, 400 V, 80 A per phase) arrives to the power distribution unit in the INT1 rack. From there all the power distribution units in the other racks, with the exception of the PLC1 and PLC2 racks, are supplied with single-phase current (230 V, 20 A). The PLC1 and PLC2 racks are supplied with 24 VDC which are delivered by a rectifier in the COM rack. Also all the sensors and actuators installed in the ArDM experiment are powered from the racks of the control system. To protect the ArDM control system from short power cuts, all the equipment, with exception of the devices supplied by the INT1 rack, are connected to two UPSs (uninterruptible power supplies), UPS 1[2] and UPS 2[3] , with a total power of 6300 W. The two UPSs can cover the power consumption of the connected equipment for about 15 min. In case of a power cut, the UPS 1 supplies the equipment in the INT2, the DAQ and the HV rack, the UPS 2 supplies the COM rack and thus also the PLC1 and PLC2 racks.

[2]APC, Smart-UPS RT 6000
[3]APC, Smart-UPS RT 3000

4.2 Vacuum Control System

The control of the ArDM vacuum system is essential for a safe operation of the ArDM experiment. As already described in Section 2.4.1, the loss of one of the vacuum insulations would lead to a huge heat input to the liquid argon chambers resulting in a dangerous pressure increase in the liquid argon chambers due to evaporation. For this reason an entire subsystem of the ArDM control system, the vacuum control system, is dedicated to control the ArDM vacuum system. A list of the instruments monitored by the vacuum control system can be found in Table 4.2. The arrangement of these instruments in the experimental setup is shown in Figure 4.2.

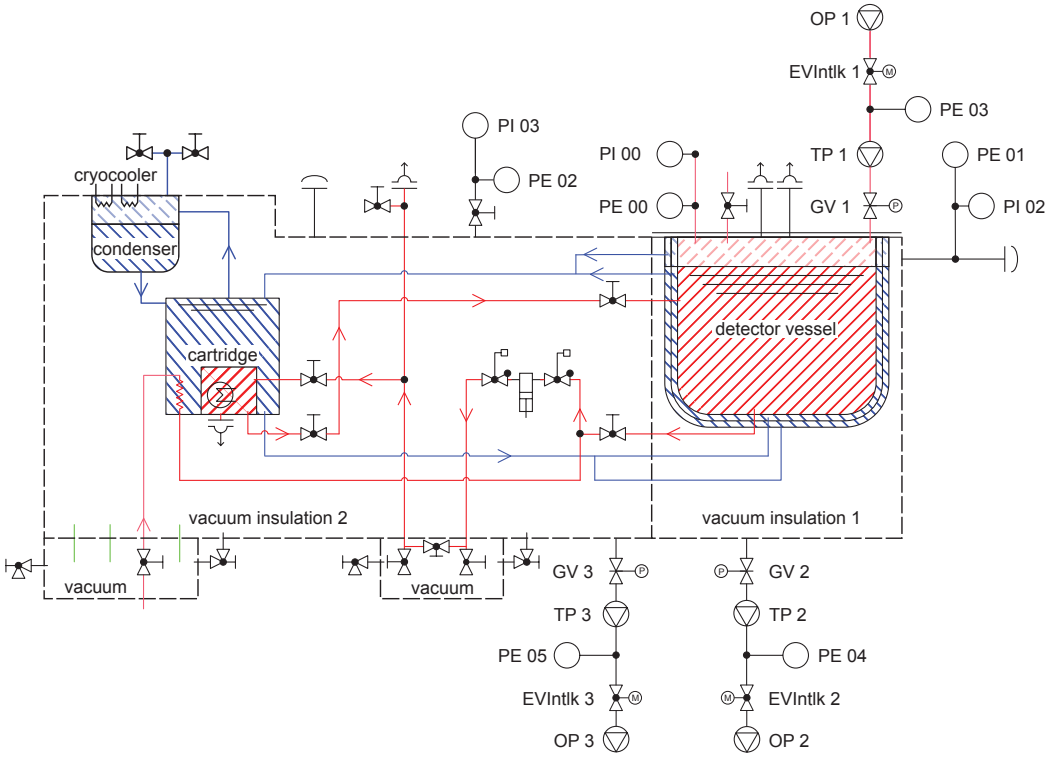

Figure 4.2: Schematic diagram of the instruments monitored by the vacuum control system. The abbreviations are explained in Table 4.2. The red (from bottom left to top right) hatched circuit is the pure liquid argon circuit, the blue (from bottom right to top left) hatched circuit is the liquid argon bath. The areas hatched with solid lines symbolise the liquid argon, the areas hatched with dashed lines symbolise the argon gas.

4.2.1 Pressure Monitoring

The most important function of the vacuum control system is the surveillance of the pressure in the two vacuum insulations. The vacuum control system also monitors the pressure in the detector vessel, when it is evacuated as a preparation for filling it with argon. The pressure in the vacuum insulations and in the detector vessel is measured with two different types of sensors: Each of the three vessels is equipped with a piezoresistive silicium pressure sensor (PI 00, PI 02 and PI 03 in Table 4.2 and Figure 4.2) and a vacuum sensor (PE 00, PE 01 and PE 02). The pressure sensors have a measurement range of 0 to 2 bar and an accuracy of $\pm 1.0\%$ over the full range. The vacuum sensor of the vacuum insulation 1 (PE 01) is a Pirani gauge with

Name	Description	Type
TP 1	turbomolecular pump of the detector vessel	Pfeiffer Vacuum, TMH 521 YP
TP 2	turbomolecular pump of the vacuum insulation 1	Pfeiffer Vacuum, TMH 261 YP
TP 3	turbomolecular pump of the vacuum insulation 2	Pfeiffer Vacuum, TMH 261 YP
OP 1	primary pump of the detector vessel	Edwards, RV 12
OP 2	primary pump of the vacuum insulation 1	Edwards, RV 5
OP 3	primary pump of the vacuum insulation 2	Edwards, RV 5
PI 00	pressure sensor of the detector vessel	Keller, PAA-21S
PI 02	pressure sensor of the vacuum insulation 1	Keller, PAA-21S
PI 03	pressure sensor of the vacuum insulation 2	Keller, PAA-21S
PE 00	vacuum sensor of the detector vessel	Pfeiffer Vacuum, PKR 251
PE 01	vacuum sensor of the vacuum insulation 1	Pfeiffer Vacuum, TPR 280
PE 02	vacuum sensor of the vacuum insulation 2	Pfeiffer Vacuum, PKR 251
PE 03	vacuum sensor between TP 1 and OP 1	Pfeiffer Vacuum, TPR 280
PE 04	vacuum sensor between TP 2 and OP 2	Pfeiffer Vacuum, TPR 280
PE 05	vacuum sensor between TP 3 and OP 3	Pfeiffer Vacuum, TPR 280
GV 1	gate valve of the detector vessel	VAT, 48240-CE74
GV 2	gate valve of the vacuum insulation 1	VAT, 12140-PA44
GV 3	gate valve of the vacuum insulation 2	VAT, 12040-PA44
EVIntlk 1	interlock valve between TP 1 and OP 1	Oerlikon Leybold Vacuum, 215 067
EVIntlk 2	interlock valve between TP 2 and OP 2	Oerlikon Leybold Vacuum, 215 067
EVIntlk 3	interlock valve between TP 3 and OP 3	Oerlikon Leybold Vacuum, 215 067
PE AComp	pressure sensor for the compressed air line	Druck, PTX 1400

Table 4.2: Instruments monitored by the vacuum control system

a measurement range of 5×10^{-4} – 10^3 mbar and an accuracy of ±15% of the measured value in the range of 10^{-3} – 10^2 mbar. The vacuum sensors of the vacuum insulation 2 (PE02) and the detector vessel (PE 00) consist of two measurement systems: a Pirani gauge and a cold cathode ionisation gauge. By combination of the two measurement systems these sensors have a wider measurement range of 5×10^{-9} mbar to 10^3 mbar. The accuracy of the sensors PE 00 and PE 02 is ±30% of the measured value in the range of 10^{-8} – 10^2 mbar.

As the accuracy of both types of vacuum sensors gets worse above 100 mbar the PLC switches automatically from the vacuum sensor to the pressure sensor if the pressure exceeds 100 mbar. The vacuum sensors of the vacuum insulation 2 and of the detector vessel can be switched on and off. Since they have a stabilising time of about 10 minutes, they are already switched on when the pressure falls below 500 mbar, but the PLC does not switch from the pressure sensor to the vacuum sensor until the pressure falls below 100 mbar and the vacuum sensor is switched on for at least 10 minutes. The Pirani gauge used for measuring the pressure in vacuum insulation 1 can not be switched off, but for consistency reasons the PLC waits for the same conditions to be fulfilled before it switches from the pressure sensor of the vacuum insulation 1 to the vacuum sensor of the vacuum insulation 1.

In order to detect a dangerous pressure increase in one of the vacuum insulations as soon as possible, the PVSS alarm management tool allows to set threshold values for the pressure in the vacuum insulations. If the pressure exceeds the chosen threshold, PVSS triggers an alarm. To ensure that also slow pressure increases in the vacuum insulations are detected in time, PVSS also generates an alarm if the pressure rises by more than 10^{-4} mbar within an hour.

4.2.2 Starting and Stopping the Pumping Systems

To protect the sensitive equipment of the vacuum system, the procedure for the evacuation of the vacuum insulations and also the detector vessel has been standardised. Activated by a command issued by means of the PVSS vacuum panel, the PLC executes the entire evacuation process for the chosen vacuum insulation or the detector vessel. First of all the evacuation process checks if a venting of the turbomolecular pump (TP 1, TP 2 or TP 3 in Table 4.2 and Figure 4.2) is necessary before the pumping system is started. As the pressure difference across the gate valve has to be smaller than 30 mbar to open the gate valve (GV 1, GV 2 or GV 3) without risk of damaging the valve, the turbomolecular pump has to be vented if the pressure between the primary pump (OP 1, OP 2 or OP 3) and the turbomolecular pump is smaller than the pressure in the vacuum vessel by more than 30 mbar. In this case, the venting of the turbomolecular pump and subsequent pumping is the only way to reduce the pressure difference across the gate valve. After the PLC released the venting, it waits for the pressure between the primary pump and the turbomolecular pump to exceed 800 mbar before it moves on to the next step. This ensures that the venting was executed properly. The pressures between the primary pumps and the turbomolecular pumps are measured with Pirani gauges (PE 03, PE 04 and PE 05) of the same type as the vacuum sensor of the vacuum insulation 1.
In both cases, if the venting of the turbomolecular pump was necessary or not, next the venting of the turbomolecular pump is disabled and the pumping station of the turbomolecular pump is turned on. The pumping stations of the turbomolecular pumps contain all the electronics needed to ramp up the motors of the pumps. Then the primary pump is turned on and the electric interlock valve (EVIntlk 1, EVIntlk 2 or EVIntlk 3) between the primary pump and the turbomolecular pump opens. Next the PLC checks simultaneously if the turbomolecular pump can be turned on and if the gate valve separating the pumps from the vacuum vessel can be opened.

If the pressure in the vacuum vessel is above 5 mbar, the gate valve is opened as soon as the pressure difference across it is smaller than 30 mbar. If the pressure in the vacuum vessel is below 5 mbar, it would be a pity to ruin the vacuum by opening the gate valve. For this reason the PLC waits in this case for the pressure on the other side of the gate valve being below 1 mbar before it opens the gate valve.

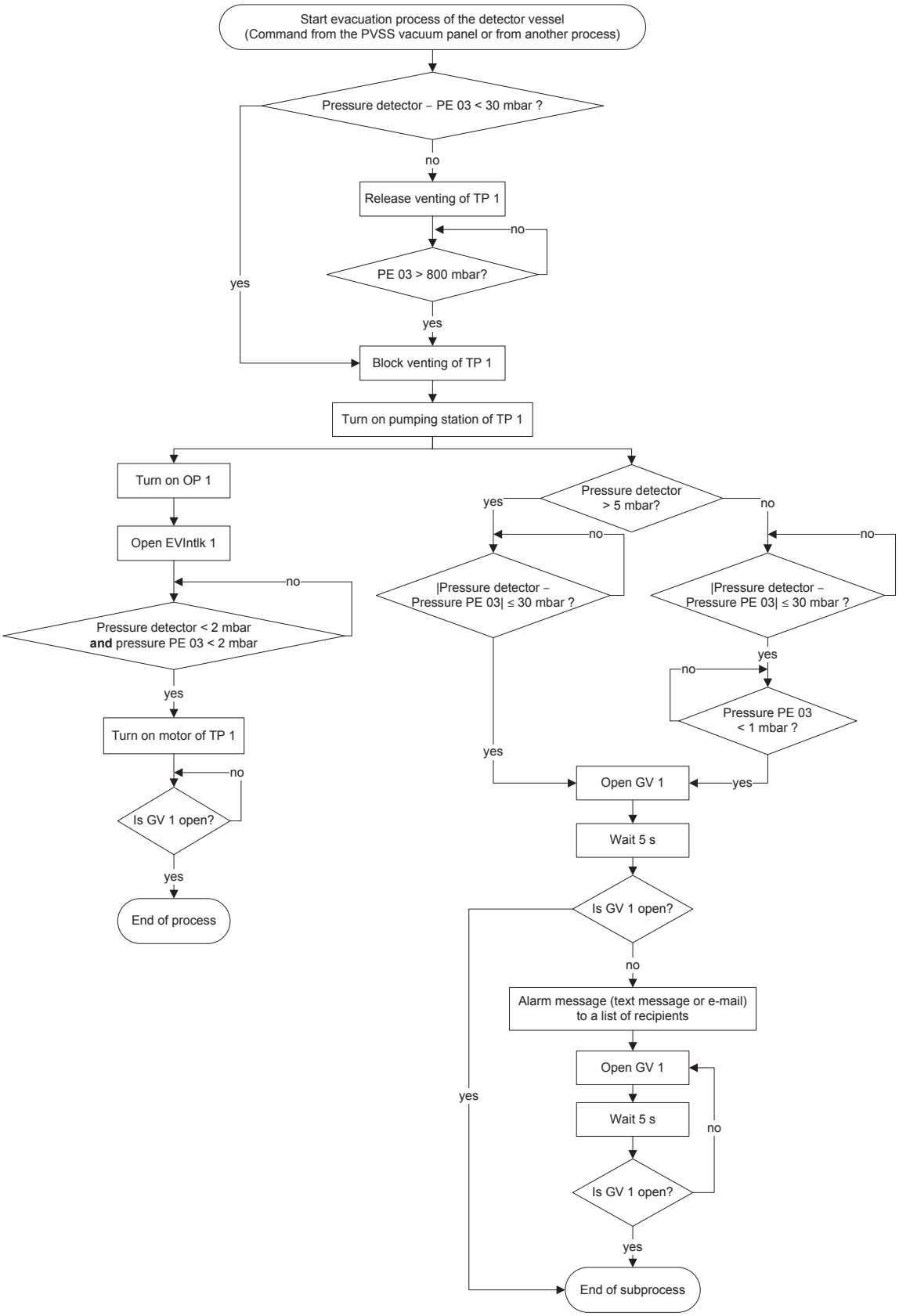

Figure 4.3: Flow diagram of the evacuation process of the detector vessel. The evacuation processes for the two vacuum insulations are identical. The abbreviations are explained in Table 4.2

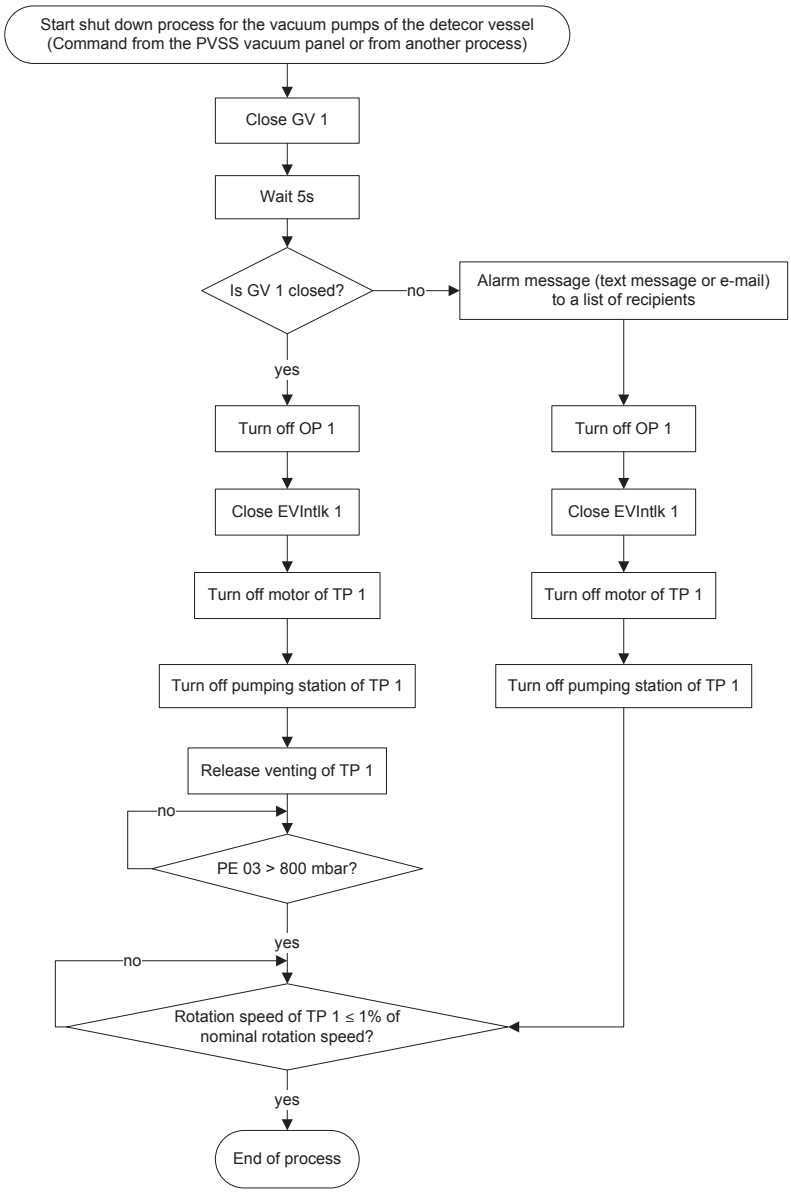

Figure 4.4: Flow diagram of the shut down process for the vacuum pumps of the detector vessel. The shut down processes for the vacuum pumps of the two vacuum insulations are identical. The abbreviations are explained in Table 4.2

The gate valves feature a position indicator. The PLC can distinguish between three different states of the position indicator: open, closed and undefined status in case of a problem with the connection of the position indicator to the PLC. Five seconds after the PLC has sent the command to open the gate valve it checks the state of the position indicator. In case the gate valve is not open the PLC causes an alarm and keeps trying to open the gate valve.
As soon as the pressure in the vacuum vessel and the pressure between the primary pump and the turbomolecular pump fall both below 2 mbar, the turbomolecular pump is turned on. To protect it from damage the turbomolecular pump should not be turned on at higher pressure. Once the turbomolecular pump is on and the gate valve is open, the PLC finishes the evacuation process.

The evacuation process is designed in such a way that it can be started for all possible pressures in the vacuum insulation and between the primary and the turbomolecular pump. A flow diagram showing the evacuation process of the detector vessel can be found in Figure 4.3.

In order to stop the vacuum pumps safely a shut down process has to be activated using the PVSS vacuum panel. This process closes the gate valve, then turns off the primary pump, closes the electric interlock valve, stops the motor of the turbomolecular pump and turns off the pumping station of the turbomolecular pump. If the gate valve was properly closed, the process now enables the venting of the turbomolecular pump and waits for the pressure to exceed 800 mbar to ensure that the venting was executed before it moves on to the next step. If the position of the gate valve is not indicated as closed, the venting of the turbomolecular pump is not enabled, in order to not ruin the vacuum, and an alarm message is sent. In both cases the PLC waits until the turbomolecular pump stops turning before it finishes the process. This ensures that the evacuation process can not be restarted and hence the gate valve will not be opened before the turbomolecular pump stopped turning. Opening the gate valve while the turbomolecular pump is still turning would endanger the pump in case the pressure in the vacuum vessel is above 0.5 mbar.

4.2.3 Measures in Case of a Power Cut

One of the most critical situations for a safe operation of the vacuum system is a power cut. A power cut affecting the vacuum system is detected if the status of the UPS 1 changes from “not on battery” to “on battery”. For short power cuts of less than 15 min the power consumption of the vacuum system is covered by the UPS 1. For longer power cuts the PLC distinguishes between two different states of the ArDM detector.
If the detector vessel is not filled with liquid argon and the vacuum insulations are evacuated for preparation of the filling of the detector vessel with liquid argon, the main aim in case of a power cut is to shut down the vacuum pumps safely in order to protect them from any damage. Already 7 minutes after the beginning of the power cut, the PLC starts the shut down process for the vacuum pumps described above. The battery of the UPS 1 should then last for about 8 more minutes which is more than enough to shut down the vacuum pumps safely. A flow diagram showing this process can be found in Figure 4.5.

The UPSs feature a digital output for a warning in case they have a low battery. If this warning is activated for the UPS 1, the PLC does not wait 7 minutes after the beginning of the power cut, but starts the shut down process for the vacuum pumps immediately.

If the detector vessel is filled with liquid argon, it is more important to maintain the vacuum insulations as long as possible than to protect the vacuum pumps. For this reason the PLC does not start the shut down process for the vacuum pumps 7 minutes after the beginning of the power cut in this case. For the full detector the shut down process is only started if the low battery warning of the UPS 1 is activated. The flow diagram of the process shutting down the vacuum pump in case of low UPS battery is shown in Figure 4.6.

As soon as the power supply for the vacuum system is re-established, the vacuum pumps can be restarted. For the restarting procedure two processes were designed. One process has to restart the vacuum pumps in case the detector vessel is filled with liquid argon, the other one has to be activated if the detector vessel is empty. Both of them are not yet implemented in the control system for lack of time of the person programming the processes. They will be integrated in the control system at the next opportunity. Nevertheless, the two processes are presented below.

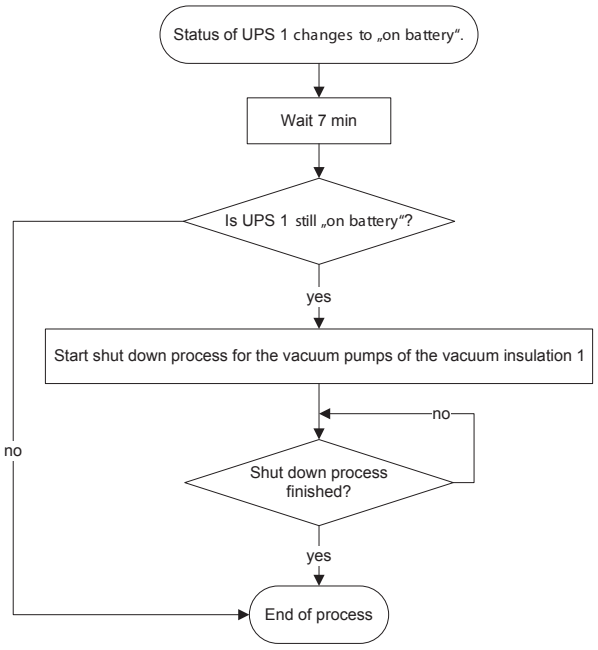

Figure 4.5: Flow diagram of the process for shutting down the vacuum pumps of the vacuum insulation 1 in case of a power cut if the detector is not filled with liquid argon. The shut down process for the vacuum pumps of the vacuum insulation 2 is identical. The abbreviations are explained in Table 4.2.

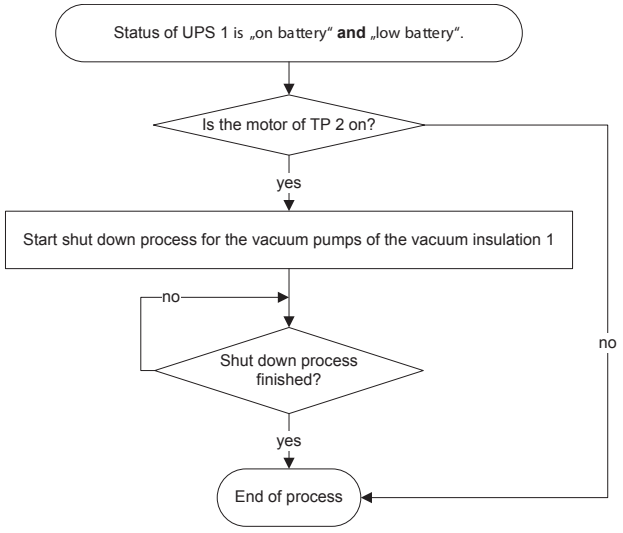

Figure 4.6: Flow diagram of the process for shutting down the vacuum pumps of the vacuum insulation 1 in case of low UPS battery. The process for the vacuum pumps of the vacuum insulation 2 is identical. The abbreviations are explained in Table 4.2

If the detector vessel is filled with liquid argon, the PLC will initiate the restarting process for the vacuum pumps as soon as the power supply for the vacuum system is re-established. For this purpose it stops all the still running shut down processes for the vacuum pumps and closes the gate valves, if not already done by the shut down processes. The evacuation process described in Section 4.2.2 is now started for both vacuum insulations. The flow diagram of the process for restarting the vacuum pumps after a power cut in case of the filled detector is shown in Figure 4.7.

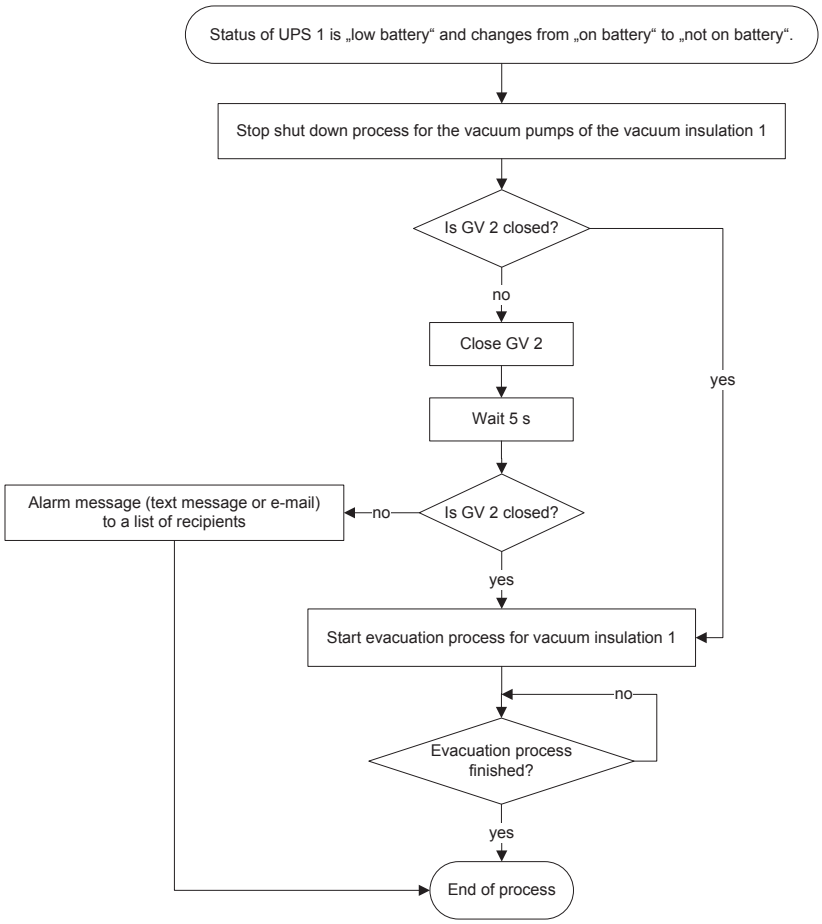

Figure 4.7: Flow diagram of the process for restarting the vacuum pumps of the vacuum insulation 1 after a power cut for the filled detector. The process for the vacuum pumps of the vacuum insulation 2 is identical. The abbreviations are explained in Table 4.2.

In case the detector vessel is not yet filled with liquid argon one of the evacuation processes could have been started only some minutes before the power cut occurred and the pressure in the affected vacuum insulation can still be above 0.5 mbar. To protect the turbomolecular pump the gate valve should not be opened if the pressure in the vacuum insulation is higher than 0.5 mbar and the turbomolecular pump is still turning. For this reason the PLC distinguishes for the not filled detector vessel between two different cases. If the pressure in the vacuum insulation is smaller than 0.5 mbar, the evacuation process is started immediately. Otherwise the PLC first turns off the motor of the turbomolecular pump if not already done by the shut down process. Then it waits until the turbomolecular pump stops turning before it restarts the evacuation process. The flow diagram showing the restarting process in the case the detector is not filled with liquid argon can be found in Figure 4.8.

As the two UPSs are essential for a safe operation of the ArDM detector the states of both UPSs are monitored by the PLC. For the following states of the two UPSs alarms are triggered:

- One of the UPSs is on battery.
- One of the UPS batteries is low.
- One of the UPSs indicates a fault.

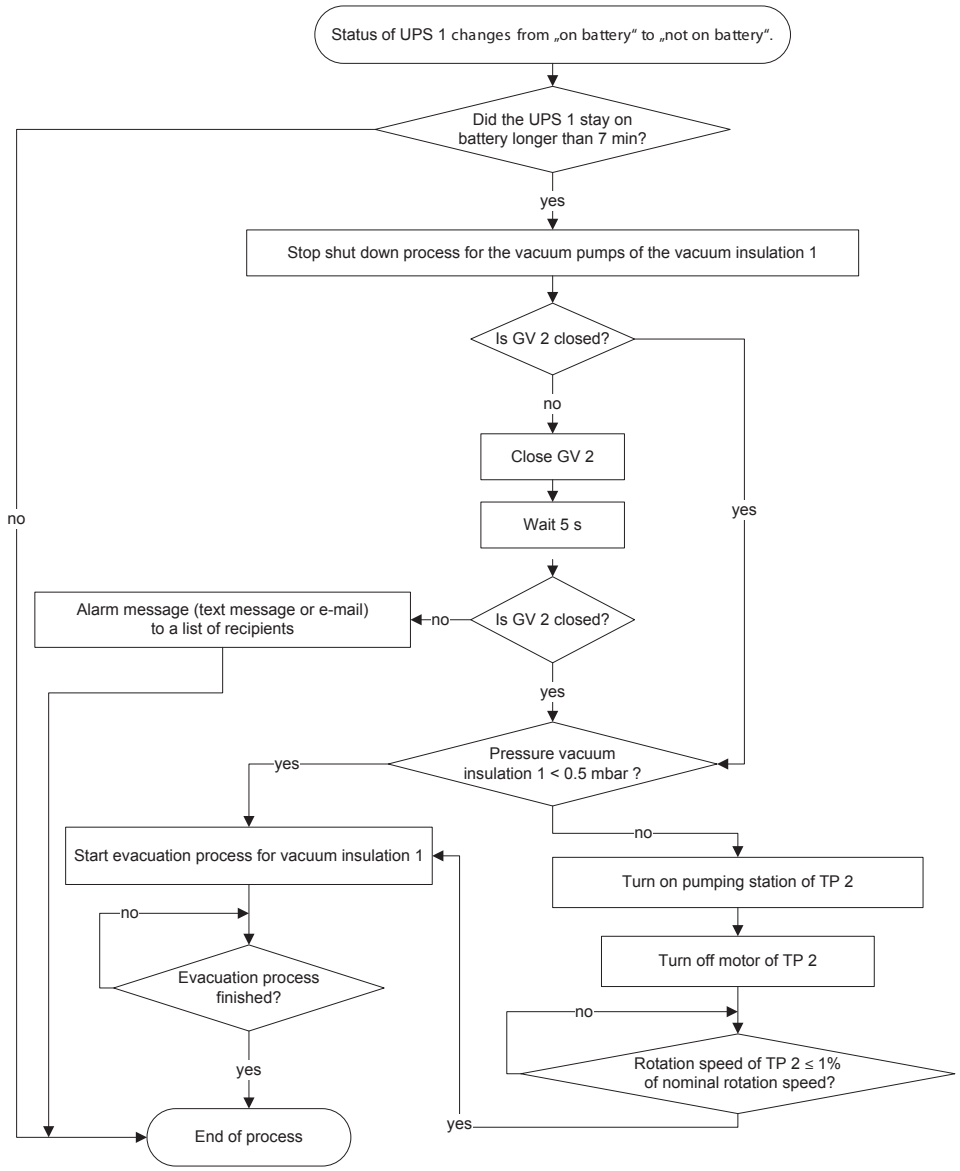

Figure 4.8: Flow diagram of the process for restarting the vacuum pumps of the vacuum insulation 1 after a power cut if the detector is not filled with liquid argon. The process for the vacuum pumps of the vacuum insulation 2 is identical. The abbreviations are explained in Table 4.2.

4.2.4 Protection of the Turbomolecular Pumps

Two processes have been designed to protect the turbomolecular pumps from damage due to unexpected pressure increase. Both of these processes send an alarm message and initialise the shut down process for the vacuum pumps described in Section 4.2.2. The conditions for starting the protection processes for the turbomolecular pumps are the following:

- The pressure in the evacuated vessel exceeds 5.5 mbar.
- The backing pressure of the turbomolecular pump exceeds 8 mbar.

The thresholds for these conditions have been determined experimentally. They are chosen high enough that the protection process is not activated during the evacuation process due to small

pressure fluctuations in the evacuated vessel or due to the increase of the backing pressure when the turbomolecular pump starts, but they are also chosen small enough to not endanger the turbomolecular pump.

If, in spite of all the measures mentioned above to protect the turbomolecular pumps from any damage, a problem with a turbomolecular pump arises and the pump sends a malfunction message, the corresponding gate valve closes immediately. Then the PVSS sends an alarm message and the PLC starts the shut down process for the vacuum pumps as shown in Figure 4.9.

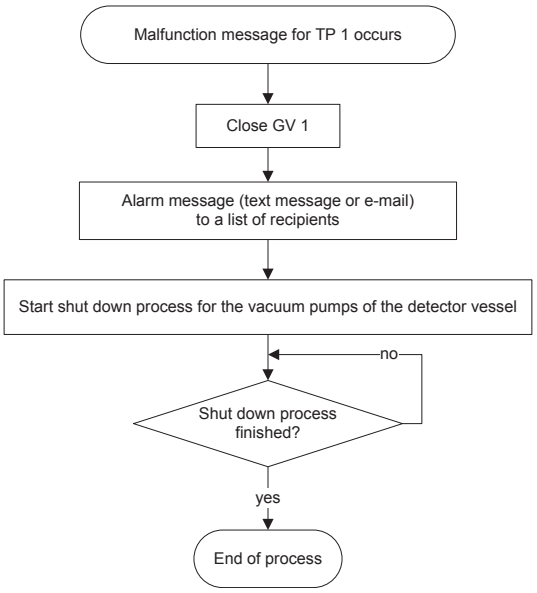

Figure 4.9: Flow diagram of the malfunction message process for the turbomolecular pump of the detector vessel (TP 1). The malfunction message processes for the turbomolecular pumps of the two vacuum insulations (TP 2 and TP 3) are identical. The abbreviations are explained in Table 4.2.

4.2.5 Monitoring of the Compressed Air Pressure

Compressed air with a minimal pressure of 5 bar absolute is needed to open and close the gate valves as well as to keep them open. The pressure in the compressed air line is measured by a piezoresistive silicon pressure sensor (PE AComp in Table 4.2) with a range of $0 - 16$ bar overpressure and an accuracy of $\pm 0.15\%$ over the full range. The PVSS sends an alarm if the pressure in the compressed air line falls below 5 bar.

4.2.6 Commissioning of the Vacuum Control System

The commissioning of the vacuum control system was carried out successively. It started in summer 2010 with the first test of the evacuation processes of the vacuum insulations and the detector vessel and ended with a final successful check of all the processes described in this section in autumn 2011. In between every process was carefully tested for all possible initial conditions, debugged and revised for several times.

As an example the result of the final check of the most crucial processes, the starting and stopping processes for the pumping system, is presented here for the vacuum insulation 1 and

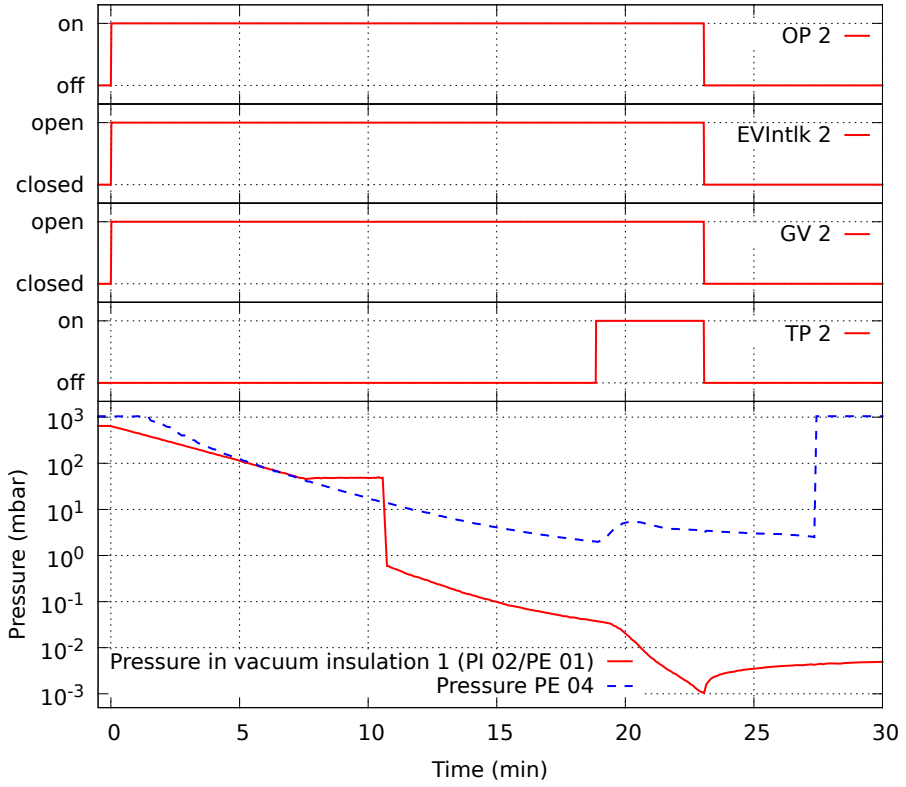

Figure 4.10: Status of the pumps and valves as well as pressure curves during the final test of the processes for starting and stopping the pumping system of the vacuum insulation 1.

one of the various tested combinations of initial pressures in the vacuum insulation and between the pumps. The test is summarized in Figure 4.10. As the process starting the pumping systems is designed for any combination of initial pressures and follows different branches of the flow diagram, depending on the initial pressures, the process has to be tested for several combinations of initial pressures to make sure that all the branches are working. For the here presented test the atmospheric pressure was chosen as initial pressure for the vacuum insulation (PI 02) as well as for the pressure between the primary and the turbomolecular pump (PE 04). The small difference between the initial pressures, which can be observed in Figure 4.10, is due to the imprecision of the vacuum sensor PE 04 at atmospheric pressure. The evacuation process was started at time $t = 0$. For the here chosen initial pressures the turbomolecular pump does not have to be vented and the PLC turns on immediately the primary pump (OP 2) and opens the interlock valve (EVIntlk 2) between the two pumps and the gate valve (GV 2) as shown in the figure. As a consequence of this, the pressures in the vacuum insulation and between the pumps decrease continuously. The step in the pressure curve of the vacuum insulation is caused by the automatic change from the pressure sensor (PI 02) to the vacuum sensor (PE 01) described in Section 4.2.1. During the stabilising time of the vacuum sensor of ten minutes the pressure sensor is still displayed even though it already reached the lower limit of its measurement range. Ten minutes after the vacuum sensor has been turned on, the PLC switches correctly from the pressure sensor to the vacuum sensor. As soon as both pressures are below 2 mbar, the PLC turns on the turbomolecular pump, which results in a slight increase of the pressure behind the turbomolecular pump and completes the successful test of the evacuation process. The shut down process was started 23 minutes after the evacuation process. As expected, the gate valve is closed immediately, then the primary pump is turned off, the interlock valve is closed and

the turbomolecular pump is turned off. Also the venting of the turbomolecular pump worked properly. Hence, the evacuation and the shut down processes passed the here presented test. Furthermore, the shut down process was also tested successfully when activated by a malfunction message of the turbomolecular pump, a power cut or one of the two conditions specified in Section 4.2.4, that ensure the protection of the turbomolecular pump.

4.3 Monitoring of the Cryogenic System

The cryogenic system of ArDM is monitored by measuring the temperature, the pressure and the liquid level in the pure liquid argon circuit and in the liquid argon bath. The sensors used for these measurements have to be suitable for operation in vacuum and at cryogenic temperatures. The self-made sensors, readout devices and installation methods for temperature and liquid level measurement developed to satisfy these high requirements are described in Chapter 3. As monitoring the cryogenic system is crucial for safe underground operation, all the temperature sensors and the self-made level meters have been integrated into the ArDM control system. Furthermore, the integration of these sensors allows to set alarms and define automated processes based on the current temperature and liquid level measurements.

4.3.1 Temperature Measurement

The ArDM control system monitors the temperature of the liquid argon circuits by means of 41 Pt10k temperature sensors. All the sensors described in Section 3.1 were included in the ArDM control system. As for the first three ArDM test runs without the control system, the resistances of the sensors are determined with the two-point measurement, but instead of the self-made read out device, now a transducer[4] measures for each Pt10k resistor the voltage drop across the sensor. The transducers supply the platinum resistances with a known current. The current is of the order of 20 μA, the exact value depends on the resistance. The analog transducer output signals of 4 – 20 mA are proportional to the temperature and correspond to 80 – 480 K. These output signals can be read out directly by the analog input modules of the PLC, which is the main advantage of the transducers over the self-made readout device described in Section 3.1.

As mentioned in Section 3.1 the Pt10k sensors used for ArDM are of the tolerance class B according to the DIN EN 60751 standard. The deviation limit of sensors of this tolerance class is $\pm(0.3°\text{C} + 0.005 \cdot |T|)$, where T is measured in °C. Additionally, also the transducers induce an error on the measured temperature. By adjusting the gain and the offset the transducers can be calibrated for two specific temperatures. For ArDM the transducers were calibrated for 80 K and 293 K. This allows a precise measurement of temperatures around the liquid argon temperature and at room temperature. The error on the temperature induced by the transducers calibrated for 80 K and 293 K is shown in Figure 4.11 as a function of the temperature. For the whole temperature range the error stays between -1 and 1 K. The error was measured for three randomly selected transducers using a resistance decade box and a Keithley 2100 multimeter for the reference measurement. The uncertainties of the error originate from the accuracy of the Keithley 2100 multimeter and the 12-bit resolution of the analog input module of the PLC.

The control of the cooling system is based on the measurement of the temperatures on the heat exchangers of the cryocoolers. These temperatures are measured with Pt1000 sensors[5] which are also included in the ArDM control system. The used Pt1000 sensors allow to measure

[4] Soclair Electronic, ISOR 80C
[5] IST AG, PW1K0.216.7W.Y.007

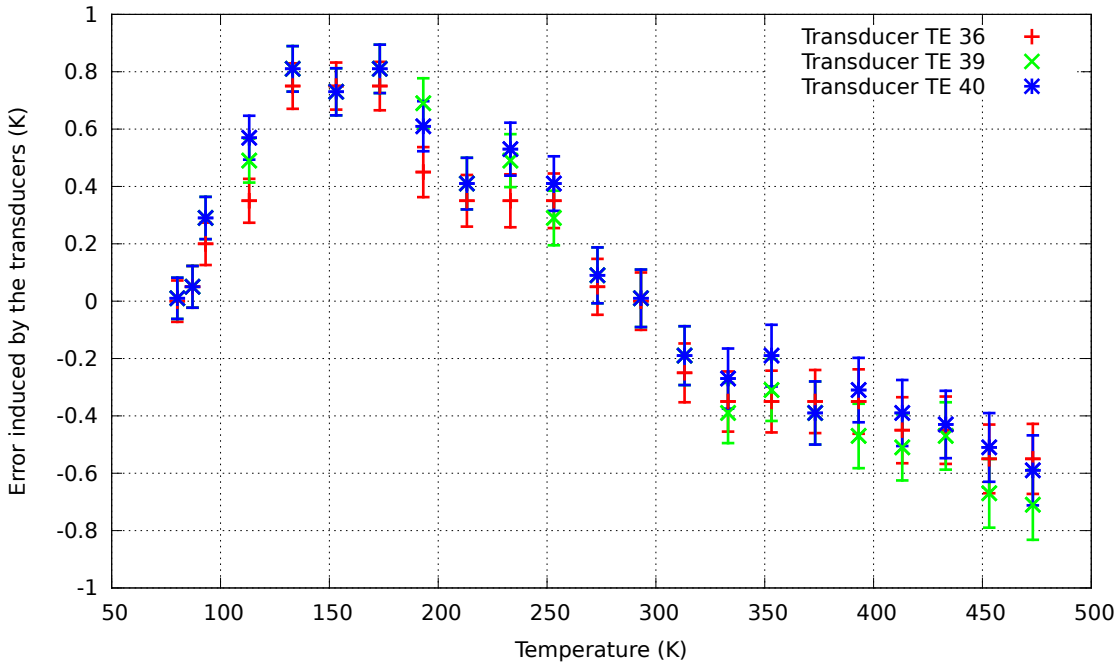

Figure 4.11: Error induced by the transducers ISOR 80C on the temperatures measured with Pt10k sensors. For the whole temperature measurement range the error stays between -1 and 1 K.

the temperature with a higher precision than the Pt10k sensors because they belong to the tolerance class 1/3 B according to the DIN EN 60751 standard. Additionally, the transducers have a better performance for resistances of the order of 1 kΩ than for resistances of the order of 10 kΩ. The resistances of the Pt1000 sensors are measured with the four-point method to avoid including the resistance of the cables between the sensors and the transducers in the measurement. The control of the cooling system is described in Section 4.4.

For all temperature sensors a threshold for triggering an alarm can be set using the PVSS alarm management tool.

4.3.2 Pressure Measurement

The pressure in the cryogenic system is measured with piezoresistive silicium pressure sensors[6]. The sensors have a measurement range of 0 to 2 bar, 0 to 4 bar or 0 to 5 bar, depending on the place of installation, and an accuracy of ±1.0% over the full range. In total 6 pressure sensors (PI 00, PI 01, PI 04, PI 06, PI 07, PI 08) are installed on the ArDM experiment to keep track of the pressure in the cryogenic system. The sensors are read out by displaying devices[7] which are located in the INT2 rack and feature an analog 4 – 20 mA output that is connected to an analog input module of the PLC. The positions of the sensors are shown in Figure 4.12.

As the stability of the pressure in the detector vessel is essential for a successful double phase operation of ArDM and indispensable for safety reasons, the pressure in the detector vessel is continuously monitored by a pressure sensor (PI 00 in Figure 4.12). In case of a significant change in pressure an alarm is triggered. As for all the sensors, the threshold for the alarm can

[6]Keller, PAA-21S and PAA-21Y
[7]Keller, EV-06

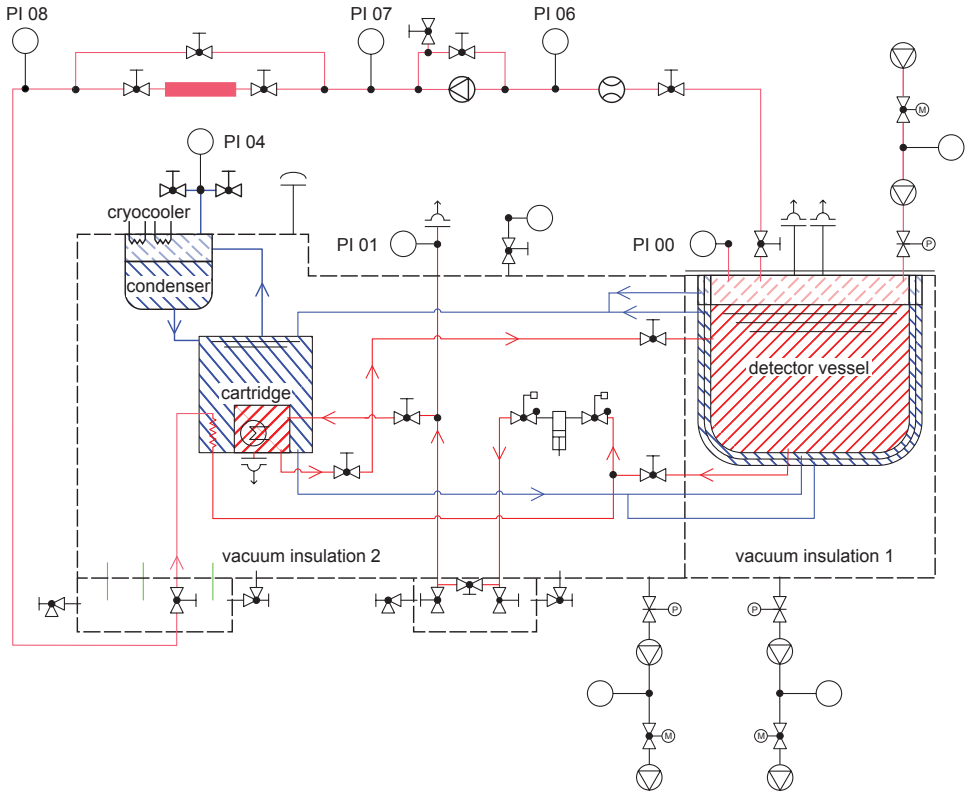

Figure 4.12: Positions of the pressure sensors for monitoring the cryogenic system. The red (from bottom left to top right) hatched circuit is the pure liquid argon circuit, the blue (from bottom right to top left) hatched circuit is the liquid argon bath. The areas hatched with solid lines symbolise the liquid argon, the areas hatched with dashed lines symbolise the argon gas.

Name	Description	Type	Range
PI 00	pressure sensor of the detector vessel	Keller, PAA-21S	0 – 2 bar
PI 01	pressure sensor in front of the liquid purification cartridge	Keller, PAA-21S	0 – 4 bar
PI 04	pressure sensor of the liquid argon bath	Keller, PAA-21S	0 – 2 bar
PI 06	pressure sensor gas purification system, between flow meter and pump	Keller, PAA-21Y	0 – 5 bar
PI 07	pressure sensor gas purification system, between pump and purification cartridge	Keller, PAA-21Y	0 – 5 bar
PI 08	pressure sensor gas purification system, after purification cartridge	Keller, PAA-21Y	0 – 5 bar

Table 4.3: Pressure sensors for monitoring the cryogenic system.

be set using the PVSS alarm management tool. Additionally to the ArDM control system a mechanical burst disk secures the detector vessel from too high pressures and provides a second level of safety.

The pressure in front of the liquid purification cartridge is measured with the sensor PI 01. The monitoring of this pressure is mainly needed during the filling of the detector vessel as the pressure in front of the cartridge easily rises during the filling due to evaporation of the argon and due to the impedance of the cartridge.
The sensor PI 04 is installed on the re-condensing unit to monitor the pressure in the liquid argon bath. Based on this pressure measurement the PLC controls two electrical valves which act as overpressure valves. The regulation of the pressure in the liquid argon bath is described in Section 4.4.
The pressure in the gas purification system is measured by the three pressure sensors PI 06, PI 07 and PI 08. PI 06 is located between the flow meter and the pump, PI 07 between the pump and the purification cartridge and PI 08 after the purification cartridge.

4.3.3 Measurement of the Liquid Argon Level

As already mentioned in Section 3.2, the liquid argon level in the detector vessel as well as in the liquid argon bath is measured with capacitive level meters. All the self-made capacitive level meters described in that section have been integrated into the ArDM control system, since the liquid argon level is a good indicator for the stability of the system and a decrease of the liquid level in the bath can have fatal consequences. Therefore, the surveillance of the liquid level is indispensable. Furthermore, the possibility to set a threshold for triggering an alarm for high and low level using the PVSS alarm management tool is very convenient.

To integrate the capacitance meter into the ArDM control system a change in its design was necessary. The measurement technique stayed the same but the measured period T could not be read out anymore via a USB interface due to the restricted input signal options of the PLC. Thus, the capacitance meter was upgraded with a time-to-voltage converter that, every $16T$, charges up a fixed capacitance with a constant current for $15T$. Then the capacitance is again discharged. The maximum voltage across this capacitance $U_{\max}$ is thus proportional to T. The output signal of the capacitance meter is a voltage between 0 and 10 V, which can be read out by the analog input modules of the PLC. The signal is a linear function of $U_{\max}$ and therefore also of T and hence of the liquid level. The capacitance meter allows to adjust the offset and the slope of this function by measuring the capacitance of the empty and of the full level meter.

The upgraded capacitance meter has one more new feature. It allows to switch off each of its eight measuring channels separately so that the unused channels can be turned off in order to reduce crosstalk between the channels.

4.4 Cooling Control System

After four test runs with the liquid argon bath open to the atmosphere, the cryogenic system of ArDM has been upgraded in spring 2011 with a condenser unit (see Figures 2.9 and 4.12) which supersedes the automatic refilling system for the liquid argon bath described in Section 3.2. The condenser unit is connected to the liquid argon bath by two insulated cryogenic lines. The liquid argon, which evaporates in the bath, is re-condensed inside the unit by two Gifford-McMahon cryocoolers[8] with a total cooling power of 600 W at 80 K. The condensed argon is then driven back to the bath by gravity. By drawing heat from the detector and by evaporation the liquid argon bath keeps the detector cold. To ensure a good cooling efficiency, the cold heads of the

[8] Cryomech, AL300 cryorefrigerator

condensers are equipped with lamellar aluminium heat exchangers. As refrigerant pure helium is used.
With the condenser unit the cryogenic system of ArDM is a closed system and decoupled from atmospheric conditions. This allows to keep the pressure in the detector stable within a few mbar, which is crucial for a successful double phase operation. Furthermore, the bath can be cooled below the atmospheric boiling point to cool the detector more efficiently.

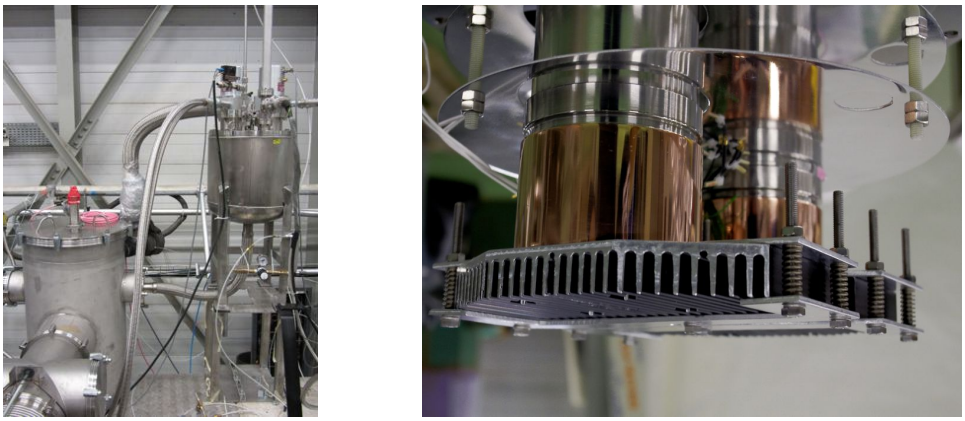

Figure 4.13: Condenser unit (left) and aluminium heat exchangers on the cold heads of the cryocoolers (right).

4.4.1 Regulation of the Cooling Power

Since the pressure in the detector depends strongly on the temperature in the bath, the cooling power has to be adjusted in order to keep the temperature in the bath constant. Since the cryocoolers run at fixed power, the cooling power has to be regulated by heaters. On top of both heat exchangers electric etched-foil heaters are installed. The foil consists of Kapton, which has a high thermal stability down to very low temperatures and a high thermal conductivity. Each heater has a maximal heating power of 250 W. The regulation of the heaters is based on the temperature measured on the corresponding heat exchanger. For each heater a proportional-integral-derivative (PID) controller regulates the heating power by pulse width modulation. This results in a rectangular shaped function for the heating power. The duty cycle, i.e. the ratio between the duration of the pulse and the period of the heating power function, is proportional to the PID controller output

$$u(t) = K_\mathrm{p} \cdot \left(e(t) + \frac{1}{T_\mathrm{i}} \int_0^t e(\tau) d\tau + T_\mathrm{d} \frac{d}{dt} e(t) \right), \tag{4.1}$$

where $e(t) = T_{\text{set-point}} - T(t)$ is the deviation, calculated as the difference of the set-point temperature $T_{\text{set-point}}$ and the measured temperature $T(t)$. The three parameters K_p, the proportional gain, T_i, the time constant of the integral action, and T_d, the time constant of the derivative of the deviation, have to be adjusted to the response of the system to the heater. The tuning of these parameters is described in Section 4.4.2.

The temperature in the condenser unit is measured with four Pt1000 temperature sensors described in Section 4.3. Besides the two temperature sensors on the heat exchangers (TE 42 and TE 43) used for the regulation of the heating power, two more Pt1000 sensors are installed in the condenser unit. The sensor TE 44 is hanging in the gas phase 5.5 cm below the bottom of the heat exchangers, whereas the sensor TE 45 is glued on the bottom of the condenser unit where it detects immediately the condensed argon dropping down from the cold heads.

4.4.2 Tuning of the Parameters of the PID controller

The right choice of the parameters K_p, T_i and T_d is essential for a good stability of the temperature in the bath and the pressure in the detector vessel. The tuning of the parameters has to be done carefully: Oscillations of the temperature should be reduced to a minimum and, in case of an increase of the set-point, the rise time of the temperature should not be too long while the overshoot should be kept as small as possible.
For tuning the parameters the Broïda method [84] was chosen. It allows to adjust the parameters by knowing the response of the system to a step ΔP in the heating power from 0% to 100% in an open loop. According to Reference [85] the step-response of a stable system with dead time τ can be approximated with the function

$$y(t) = 1 - e^{-\frac{t-\tau}{\theta}}, \tag{4.2}$$

where θ is the time constant of the system. The response of our system is the temperature of the heat exchanger. Thus, τ and θ can be determined by monitoring the step-response of this temperature in an open loop. Once τ, θ and the temperature increase ΔT induced by the change of heating power are known, the gain $G = \Delta T/\Delta P$ can be calculated and the PID controller parameters can be determined using Table 4.4 [84]. The parameters proposed in this table were found empirically.

Controller	$\mathbf{K_p}$	$\mathbf{T_i}$	$\mathbf{T_d}$
P	$\frac{0.8\cdot\theta}{G\cdot\tau}$		
PI	$\frac{0.8\cdot\theta}{G\cdot\tau}$	$\frac{G\cdot\tau}{0.8}$	
PID	$\frac{\theta/\tau+0.4}{1.2\cdot G}$	$\theta + 0.4\cdot\tau$	$\frac{\theta\cdot\tau}{2.5\cdot\theta+\tau}$

Table 4.4: Controller settings according to the Broïda method [84].

In order to take into account the heat transfer between the argon and the heat exchangers when tuning the PID controller, the step-response of the temperature of the heat exchanger has to be measured when the experiment is filled with liquid argon. This requires that the system is heated only for a short time. A big heat input would lead to a dangerous pressure increase in the detector vessel. Therefore, the heater had to be switched off before the temperature of the heat exchanger visibly levelled off, i.e. before the final temperature increase ΔT is known. To determine ΔT and θ in this case, the function

$$T(t) = \Delta T \cdot \left(1 - e^{-\frac{t-\tau}{\theta}}\right) + T_\mathrm{start} \tag{4.3}$$

can be fitted to the temperature data. T_start is the starting temperature before the heater is turned on. The data and the fit are shown in Figure 4.14 for heater 1 and in Figure 4.15 for heater 2. The parameters θ and ΔT resulting from the fit and the values for τ and T_start are listed in Table 4.5. While both heaters show similar time constants θ, heater 1 has a four times longer dead time τ than heater 2. This could be due to a difference in installation of the heaters. Heater 2 was glued and screwed on the heat exchanger whereas heater 1 was only screwed on the heat exchanger.

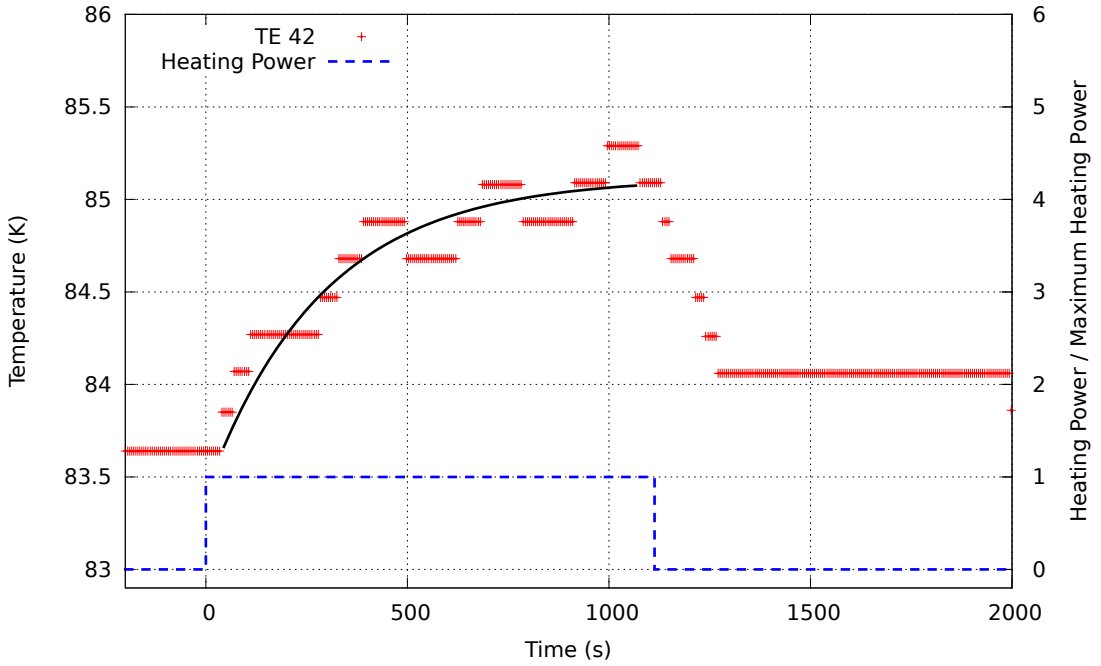

Figure 4.14: Step-response of the temperature of the heat exchanger 1 (TE 42). The Function (4.3) was fitted to the data points. The results for the parameters θ and ΔT are shown in Table 4.5. The dashed blue curve represents the relative heating power.

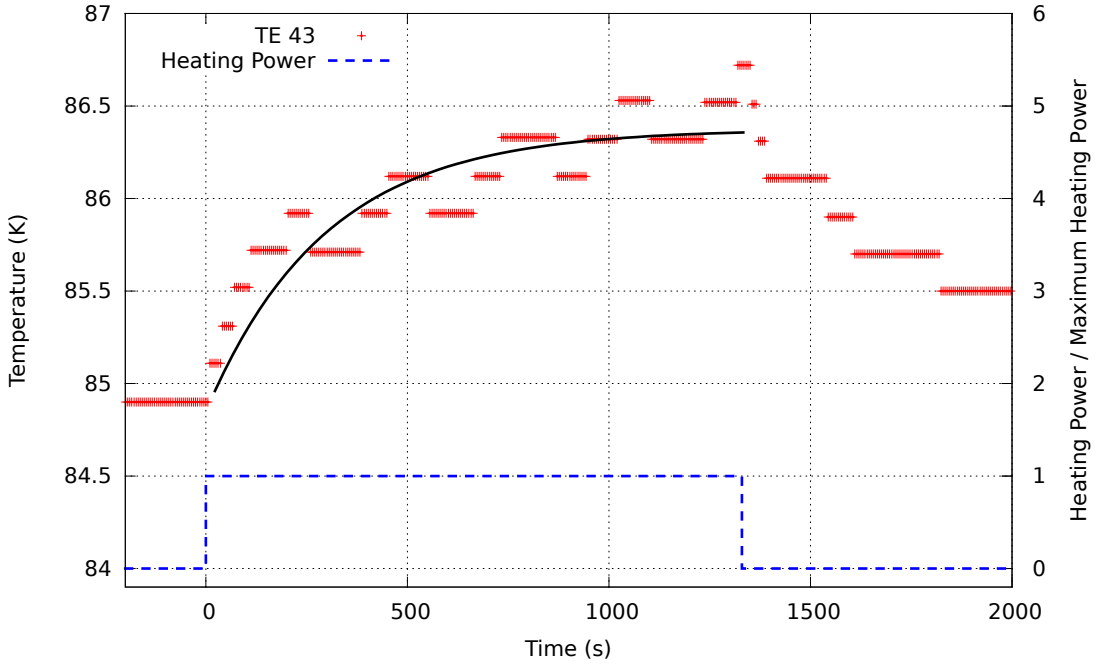

Figure 4.15: Step-response of the temperature of the heat exchanger 2 (TE 43). The Function (4.3) was fitted to the data points. The results for the parameters θ and ΔT are shown in Table 4.5. The dashed blue curve represents the relative heating power.

For both heaters is $\theta/\tau > 5$. In this case it is recommended to use only a pure PI controller instead of a PID controller [84]. The parameters K_p and T_i calculated from τ, θ and ΔT using Table 4.4 are presented in Table 4.5.

	Heater 1	**Heater 2**
τ (s)	40	10
T_start (K)	83.64	84.90
θ (s)	289 ± 14	297 ± 15
ΔT (K)	1.48 ± 0.02	1.47 ± 0.02
K_p (K^{-1})	391 ± 26	1611 ± 104
T_i (s)	0.739 ± 0.012	0.184 ± 0.003
T_d (s)	0	0

Table 4.5: Tuning of the PID controller parameters by fitting the Function (4.3) to the step-response.

The first test of the cooling control system was not done with the calculated values for K_p and T_i of Table 4.5, but with parameters derived from θ and ΔT determined by eye looking at the data for the temperature of the heat exchangers presented in Figures 4.14 and 4.15. The values of τ, T_start, θ, ΔT, K_p and T_i used for the first test are shown in Table 4.6. As above, the parameters K_p and T_i were calculated using Table 4.4. While the values for T_i are quite close to the ones calculated above and the K_p for heater 1 is even within the error of the fitted K_p for heater 1, the K_p of heater 2 differs by more than a factor two from the value resulting from the fit. For the K_p of heater 2 the identification of the time constant θ by eye failed completely. In spite of this deviation, a good stability of the temperature on the heat exchangers was achieved. After the tuning of the parameters, the temperature variations on both heat exchangers stayed within 0.1 K for a fixed set-point. During the first test of the cooling control system the controllers also kept the pressure in the detector stable within a few mbar as shown in Section 4.4.4.

	Heater 1	**Heater 2**
τ (s)	40	10
T_start (K)	83.6	84.9
θ (s)	260	100
ΔT (K)	1.3	1.1
K_p (K^{-1})	400	727
T_i (s)	0.65	0.14
T_d (s)	0	0

Table 4.6: Tuning of the PID controller parameters by eye.

4.4.3 Safety Measures

The ArDM control system also ensures the safety of the experiment in case of a failure of the cryocoolers or the heaters. The operation of the cryocoolers is permanently surveyed by monitoring the temperatures of the heat exchangers and the electrical current of the cryocoolers. The current of both cryocoolers is measured and displayed by an AC ampere meter in the INT1 rack. The analog output of the ampere meter is read out by the PLC, so that the current of the cryocoolers can also be checked using PVSS. A failure of the heaters or their regulation is immediately detected by the temperature sensors on the heat exchangers and emits an alarm.

A dangerous pressure increase in the liquid argon bath could be the consequence of a malfunction of the cryocoolers or their heaters. To avoid this scenario two electromagnetic valves (EV 23 and EV 24) are installed on the bath. They are controlled by the pressure sensor PI 04. For both electromagnetic valves two set points can be chosen on the cryocooler panel: an upper one for opening the valve and a lower one for closing the valve. The electromagnetic valves relieve the pressure in the bath in case PI 04 measures a pressure above the upper set point. As soon as the pressure falls below the lower set point, the valves close again.

4.4.4 First Test of the Cooling Control System

In spring 2011 the condenser unit and the cooling control system were commissioned at CERN on the surface. The whole cryogenic system has been operated for more than seven weeks. Apart from the tuning of the parameters of the PID controllers, described in Section 4.4.2, this test allowed to check the stability of the system and measure the cooling power needed to keep the cryogenic system at liquid argon temperature.
The condenser unit made it possible to fill the liquid argon bath by condensing argon gas. The 200 l liquid argon contained in the bath were liquefied within less than five days. Before the detector was filled with liquid argon it was precooled with argon gas. Figure 4.16 shows the cooling power delivered to the system during the entire run. The average cooling power for the detector filled with argon gas at 0.8 bar (time interval a) in Figure 4.16) was measured to be (368.7±1.0) W. The cooling power was determined by subtracting the power applied to the heaters from the cooling power of the cryocoolers, which is fixed by the temperature of the cold heads. For temperatures around the normal boiling point of argon the cooling power of the cryocoolers is about 600 W. As the power applied on the heaters is highly fluctuating, every data point in Figure 4.16 indicates the cooling power averaged over 1 h.

Besides the condenser unit and the cooling control system also the membrane pump for the recirculation of the liquid argon was tested during this run. Figure 4.16 distinguishes between three time intervals for the detector filled with liquid argon: b) and d) indicate the operation of the cryogenic system with liquid argon recirculation, c) indicates the operation without liquid argon recirculation. The average cooling power is (541.3±0.3) W, when the membrane pump is running (b) and d)), and (512.6±0.5) W, when the membrane pump is not running (c)). The liquid argon recirculation leads to an additional heat input of almost 30 W. During the filling process (07/04 to 08/04/2011) the maximum cooling power of 600 W was needed and the heaters were completely turned off. The second rise in cooling power up to 600 W indicates the tuning of the PID controller of the heaters. Between the two maxima, the system was not in a stable condition and a statement about the cooling power is not possible.
Although the detector vessel has not been filled completely, but only up to the temperature sensor TE 05, corresponding to ∼60 % of the total height of the detector vessel, the here presented cooling power exceeds the heat input to the liquid argon bath measured in Section 3.2 by

more than 120 W. This shows that the heat input to the bath measured in September 2010 does not correspond to the total heat input of ArDM and that, before the upgrade of the cryogenic system to a zero loss system, the top flange has been cooled efficiently with the argon gas from the exhaust of the bath.

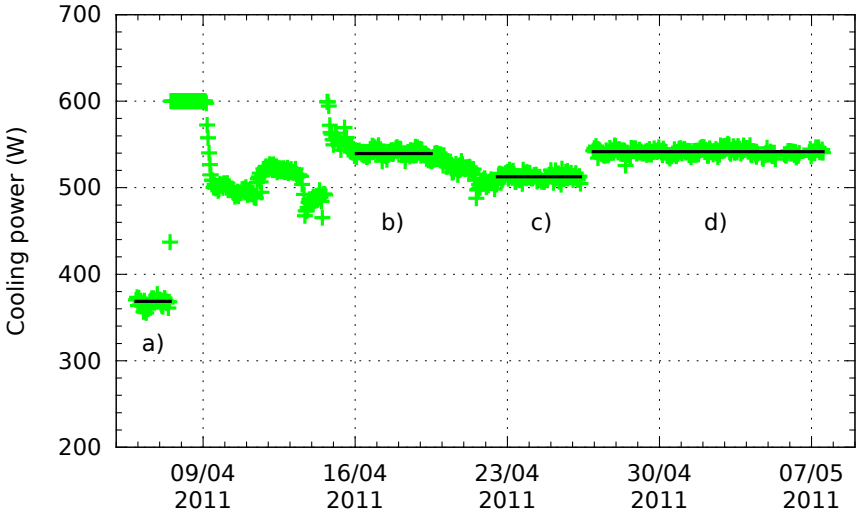

Figure 4.16: Cooling power delivered to the ArDM cryogenic system during the first test of the condenser unit and the cooling control system. For the time interval a) (0.8 bar of argon gas in detector) the average cooling power is (368.7±1.0) W. With liquid argon in the detector the cooling power amounts to (541.3±0.3) W, when the membrane pump is running (time intervals b) and d)), and (512.6±0.5) W when the membrane pump is not running (time interval c)).

For a successful double phase operation the cooling control system has to provide a good stability of the pressure in the ArDM detector. Therefore, the stability of the pressure in the detector vessel was checked during the commissioning of the cooling control system. A stability test of 6.5 days showed that the cooling control system keeps the pressure in the detector vessel stable within a few mbars. During the entire stability test, all the relevant parameters were left unchanged. The set-point temperature of the heaters was fixed to 84.5 K and the membrane pump was on. Figure 4.17 shows the pressure history of the entire stability test. The mean value of the pressure is 1022.7 mbar, the standard deviation is 1.5 mbar. A linear fit of the pressure gives a slope of (-8.7±2.6) $\cdot 10^{-8}$ mbar/s. This shows that the mean value is almost constant over time. The fluctuations stay within a range of ± 6.4 mbar around the mean value.

The repetition of the same test for different set-point temperatures of the heaters showed that the pressure in the detector is a linear function of the set-point temperature. Figure 4.18 shows the pressure distributions (green) and the mean values (black) for 84.0 K, 84.5 K, 84.7 K, 84.9 K and 85.1 K. After changing the set-point temperature the system needs about 8 h to stabilize. Only data recorded after the system stabilized are shown in Figure 4.18. For all the set-points the pressure was recorded for at least 15 h. A linear fit of the mean values gives a slope of (68.3±2.0)mbar/K and a constant of (-4749±190)mbar. As the pressure in the detector vessel does not only depend on the set-point, but also on the temperature of the top flange, which varied by about 4 K between the different measurements, the pressure has been corrected to a top flange temperature of 182 K. The correction was done assuming that the pressure depends linearly on the top flange temperature.

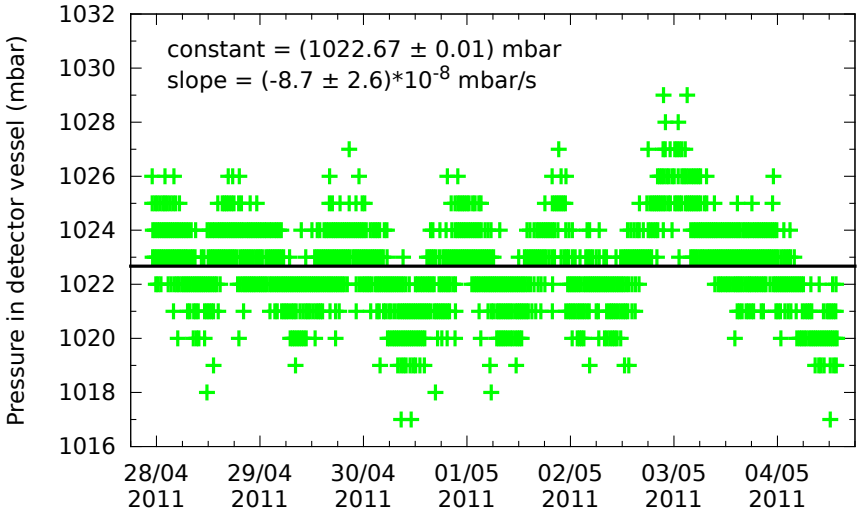

Figure 4.17: Pressure in the detector vessel during a stability test lasting 6.5 days. The pressure fluctuations stay within a range of ± 6.4 mbar around the mean value.

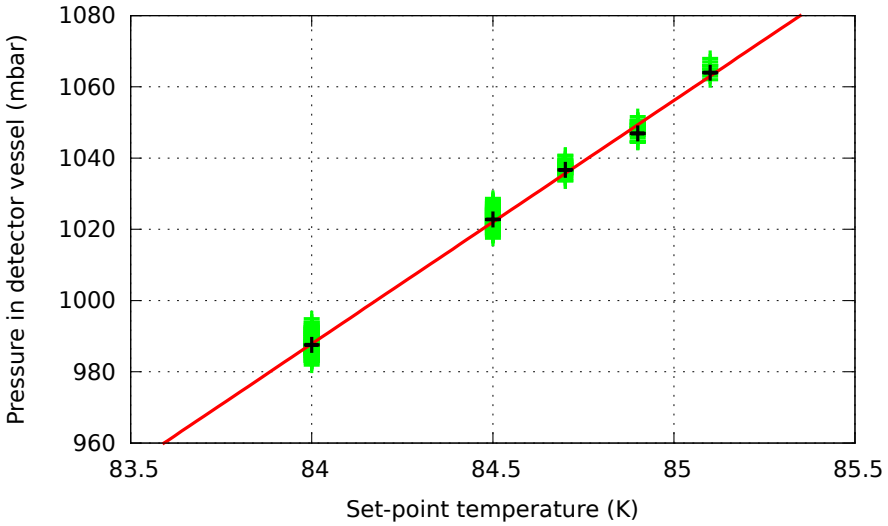

Figure 4.18: Pressure in the detector vessel as a function of the set-point temperature of the heaters. The mean values (black) are fitted with a linear function with a slope of (68.3±2.0) mbar/K and a constant of (-4749±190) mbar.

The boiling temperature of argon at 1013 mbar is 87.3 K [38]. According to the fit of the mean pressures, 84.4 K has to be chosen as set-point temperature for keeping the pressure in the detector at 1013 mbar. Thus, the difference in temperature between the cold heads and the liquid argon in the detector amounts to 2.9 K. This temperature gradient is needed to cool the detector efficiently.
The here presented relation between the pressure in the detector and the set-point temperature was measured with the detector vessel only filled up to ∼60% of the total height. As the heat input from the top flange increases with rising liquid level, for the full detector the pressure in the detector vessel at the same set-point temperatures is expected to be higher.

4.5 Control of the Argon Purification Systems

Both argon purification systems described in Section 2.4.2 have been integrated into the ArDM control system. It monitors the temperature as well as the pressure and controls the pumps of both, the liquid argon and the gas purification system. Furthermore, three heaters to warm up the argon gas, before it reaches the pump of the gas purification system, are included in the control system, which also monitors the argon gas flow in front of the pump.

4.5.1 Liquid Argon Purification System

As already mentioned in Section 2.4.2, a custom-made membrane pump was used to circulate the liquid argon in the pure liquid argon circuit during the test runs on the surface. This pump was integrated in the ArDM control system and actuated by the PLC. Since the membrane pump could not be operated as stable as needed for a dark matter run lasting several weeks, it might be replaced for future underground operation. In this case the control of the old membrane pump will become redundant, but, since the control was successfully operated during several test runs and the difficulties operating the pump were independent from the control, it will be described briefly in this section.

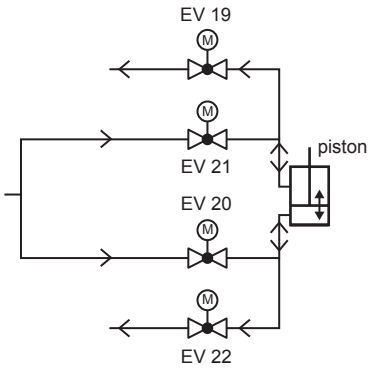

Figure 4.19: Schematic diagram of the pneumatic actuator of the membrane pump. The piston is moved by two inlet valves (EV 20 and EV 21) and two outlet valves (EV 19 and EV 22) controlling the flow of compressed air. The figure is modified from [86].

A piston moves the membrane of the pump and thus expands and contracts the volume of the pump and circulates the liquid. This piston is moved pneumatically by means of four electromagnetic valves: two inlet valves (EV 20 and EV 21) and two outlet valves (EV 19 and EV 22). A schematic diagram of the valves and the compressed air lines is shown in Figure 4.19. The actuators of all four valves are connected to the digital output modules of the PLC. By applying 24 V, the PLC opens the inlet valve on one side of the cylinder and the outlet valve on the other side of the cylinder at the same time, while the other two valves stay closed. If EV 19 and EV 20 are open the pressure in the volume below the piston is built up, the piston moves up and the air in the upper cylinder volume is pushed out through EV 19. The piston is moved down when the PLC closes EV 19 and EV 20 and opens EV 21 and 22.
The duration, for which the valves stay open, can be entered in the PVSS cryogenics panel in steps of 200 ms for each pair of inlet and outlet valves separately. On the cryogenics panel the pump can also be switched on and off.

4.5.2 Gas Purification System

To purify the evaporated argon, a gas purification system, which can be operated independently from the liquid argon purification system, is part of the cryogenic system of ArDM. A double membrane pump[9] (P 1 in Figure 4.20) circulates the argon from the gas phase of the detector through an ambient temperature purification cartridge[10] and, after condensation, back to the detector vessel. The ArDM control system allows to turn on and off the pump manually on the PVSS cryogenics panel and a LED on the front side of the INT1 rack indicates if the pump is running.

A high flow thermal mass flow controller[11] (FI 01) measures and regulates the flow in the gas recirculation system. The controller is equipped with a flow sensor, a normally closed control valve and a PID controller to regulate the gas flow. It communicates with the control system using a DeviceNet interface. DeviceNet is a network protocol used in the automation industry. The PLC reads the measured flow, which can be displayed in an additional window by choosing the symbol of the flow controller in the PVSS cryogenics panel. The set-point for the flow control can be entered into the same window and is transmitted over the DeviceNet interface to the flow controller. The measured flow and its set-point are indicated in standard liter per minute (slm) N_2 equivalent. The maximum flow through the flow controller is 200 slm N_2 equivalent and the accuracy of the flow controller is $\pm 1\%$ of the set-point.

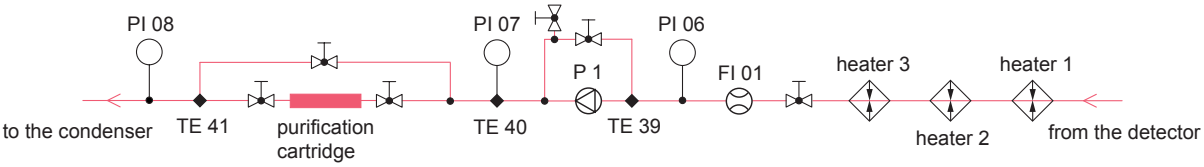

Figure 4.20: Schematic diagram of the gas purification system including the three heating bands (heater 1,2,3), the mass flow controller (FI 01), the double membrane pump (P 1), the purification cartridge, the temperature sensors (TE 39, 40, 41) and the pressure sensors (PI 06, 07, 08).

According to its specifications, the double membrane pump should not be operated with gas colder than 5°C. Thus, the evaporated argon has to be warmed up before it arrives to the double membrane pump. For this reason, up to three electrical heating bands (heater 1, 2, 3) can be installed on the tubes of the gas purification system in front of the pump. Every heating band has its own temperature controller[12] located in the INT1 rack. Between the tube and each heating band a Pt100 temperature sensor is installed, which is read out directly by the controller of the heating band. Based on the measured temperature, the controller, a PID controller with the capability of self-tuning, regulates the power of the heating bands. The controllers also transmit the measured temperatures over an analog input (4 – 20 mA) to the PLC. An analog output allows to send a set-point temperature for the heating bands to the particular controller. Over a digital output, an internal dry contact, the controller can report a general fault indication. The controllers and thus the heating bands can be switched on and off by means of an external dry contact. The output signals of the controllers are displayed in additional windows, which can be opened by clicking on the symbols of the heating bands in the PVSS cryogenics panel. As the warming up of the argon gas is not without risks, the

[9] KNF, N 0150.1.2.AN.12
[10] SAES Pure Gas Inc., MC4500
[11] MKS Instruments, MC20 ALTA mass flow controller
[12] Winkler, WRW-200

temperature and the pressure are monitored at three points in the gas recirculation system. The precise position and the type of the sensors are described in Section 3.1 and 4.3 respectively. Several processes protecting the double membrane pump, the purification cartridge and the other parts of the gas purification system from extreme temperatures and pressures are based on these temperature and pressure measurements. To prevent the pump and the purification cartridge from damage, the pump is turned off if one of the following situations occurs:

- The temperature in front of the pump (TE 39) is above 40°C.
- The temperature in front of the pump (TE 39) is below 5°C.
- One of the pressure sensors PI 06, PI 07 or PI 08 indicates a pressure above 3 bar.
- The temperature in front of the purification cartridge (TE 40) is above 40°C. (The maximum allowed temperature of the purification cartridge is 40°C.)

If the double membrane pump is not running, warming up the evaporated argon is useless. Thus, the processes turning off the double membrane pump also switch off the heating bands. In case one of the controllers of the heating bands generates a fault indication, it has to be assumed, that the regulation of the heating power of the affected heating band is not working properly anymore, and the controller and its heating band are automatically switched off. The heating bands are also switched off if the temperature measured between the heating band and the tube exceeds 150°C.
Unlike the temperature sensors, pressure sensors and the flow controller, the double membrane pump as well as the heating bands and their controllers are not connected to a UPS, as the gas purification system does not have to be kept running for safety reasons in case of a power cut. After a power cut the controllers of the heating bands restart regulating the temperature of the argon gas immediately while the pump has to be turned on manually.

The control of the gas purification system was commissioned during the last cryogenic test run of ArDM above ground in autumn 2011. All the processes, the regulation of the argon gas flow and the control of the heating bands have been tested successfully. The cryocoolers provided enough power to cool down and condense all the argon gas, that has been circulated through the gas purification system, even though the cooling power required during the test run without gas purification system in spring 2011 (see Section 4.4.4) almost reached the maximum cooling power of the cryocoolers of 600 W. Even at maximum flow rate, when the valve of the flow controller was completely open, the 600 W cooling power were sufficient.

4.6 Control of the AC Power Supply Unit for the Greinacher Circuit

The high voltage for the electrical drift field in the ArDM detector is generated with a Greinacher high-voltage multiplier, described in Section 2.3.3. The Greinacher circuit is charged up with an AC power supply unit specially developed for this purpose [87]. Up to now the power supply unit is monitored and controlled by a computer via a USB interface. An upgraded version of the power supply compatible with the inputs and outputs of the PLC is under development. The USB interface will be replaced by analog inputs and outputs of 0 – 10 V and digital signals of 24 V.

The current version of the power supply contains a power amplifier, which provides an alternating output voltage with a peak-to-peak value up to 2.7 kV, a maximum current of 10 mA

(r.m.s.) and a fixed frequency of 50 Hz. The peak-to-peak voltage can be set using a LabView based graphical user interface and is transmitted to the power supply through the USB interface. On the same user interface the ramp-up-rate of the output voltage can be chosen and the ramping up can be started or stopped. The power supply includes a peak-to-peak detector for the output voltage and an absolute peak detector for the output current. The measured values are read out via the USB interface. The waveforms of the output voltage and current can be displayed on an oscilloscope using two analog outputs of the voltage supply. A button on the front panel of the power supply allows to enable and disable the power supply manually. An unexpected discharge of the Greinacher circuit can cause an over-current in the secondary coil of the transformer of the power amplifier. By means of a potentiometer on the front panel of the power supply a limit for the current in the secondary coil can be set. If the measured peak value of the current exceeds the current limit, the power supply turns off the power amplifier.

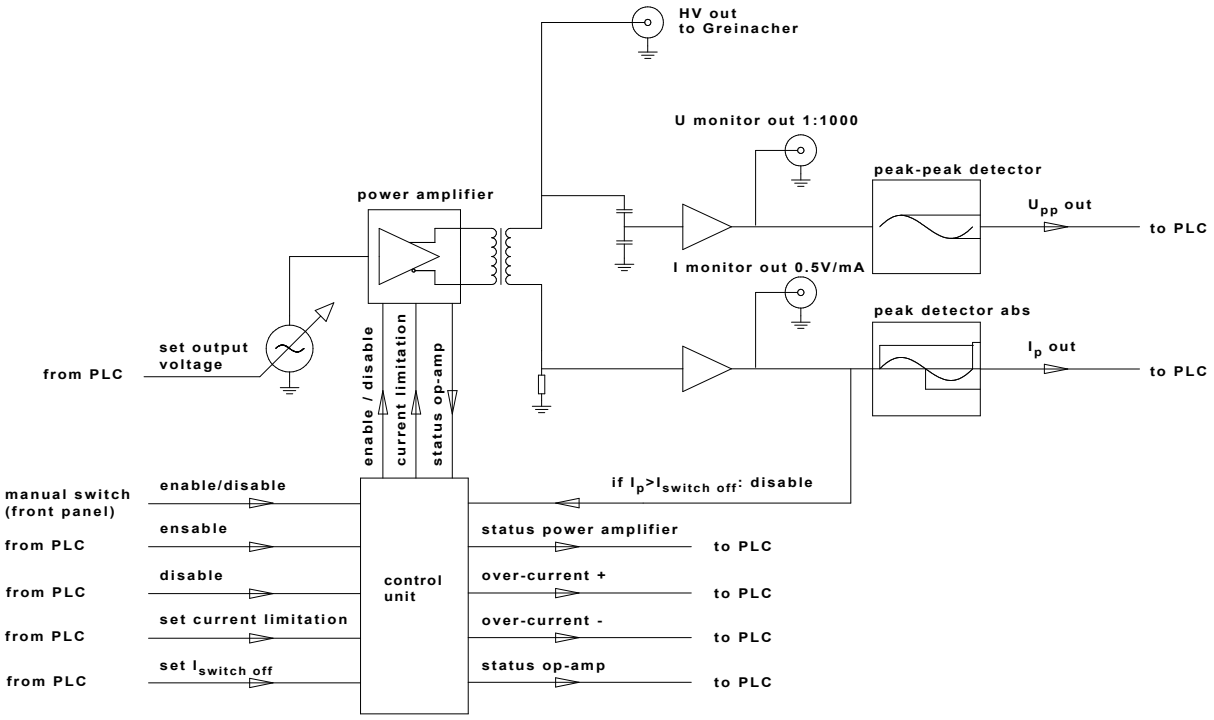

Figure 4.21: Block diagram of the Greinacher AC power supply unit compatible with the PLC. This version of the power supply unit is under development. The figure is modified from [87].

The upgraded version of the AC power supply will be based on the same power amplifier and feature all the functions described above. A block diagram of the upgraded power supply is shown in Figure 4.21. The new power supply will be controlled by the PLC. The output voltage and its ramp-up time have to be set using the PVSS Greinacher circuit panel, where also the peak-to-peak value of the voltage U_{pp} and the peak value of the current I_{p} will be displayed. The power supply can be enabled and disabled not only using a button on the front panel but also from the PVSS Greinacher circuit panel. To enable and disable the power amplifier the PLC will send a short 24 V pulse of 200 ms to the power supply. There will be no possibility anymore to set the current limit for switching off the power amplifier on the front panel, but the PVSS Greinacher circuit panel will allow to set this limit ($I_{\mathrm{switch\ off}}$ in Figure 4.21). The PLC compatible version of the AC power supply will also feature some new input and output signals. Four digital outputs will indicate the status of the power amplifier (enabled/disabled),

a positive over current, a negative over current and a shut down of the op-amp of the power amplifier for example due to overheating. A new analog input allows to set an upper limit for the current in the primary coil of the transformer.

4.7 General Safety Monitoring

In addition to its main function of monitoring and controlling the ArDM subsystems, the ArDM control system is also designed to be a general safety monitor which triggers alarms in case of oxygen deficiency or fire.
The handling of large volumes of liquid argon always involves the danger of oxygen deficiency. Thus, the oxygen concentration around the ArDM experiment is monitored by three oxygen sensors[13]. The sensors are located below the experiment as the leaking argon would concentrate on the ground of the building due to its higher density compared to air. Every sensor is connected to a display unit located in the INT1 rack. The display units feature two analog 4 – 20 mA outputs which are scaled over 0 – 100% and 0 – 25% oxygen volume fraction. The latter is connected to the PLC and the measured oxygen volume fraction is indicated on the PVSS cryogenics panel. In case of a drop of the measured oxygen volume fraction the PVSS triggers an alarm. The oxygen volume fraction in dry air is 20.95%. If the oxygen volume fraction falls below 17% the human body has first symptoms of hypoxia, such as accelerated heart beat and increased reaction time. Thus, an oxygen volume fraction of 18% was chosen as threshold for triggering an alarm.

Seven racks mainly containing cables and electrical installations are a potential source of fire. To detect a fire in the electronic racks as early as possible and prevent the fire from spreading in the underground laboratory, it is planned to install an aspirating smoke detector inside the racks. The smoke detector is supposed to communicate with the PLC and transmit the fire alarms. As the smoke detector might not only have an output for an alarm, but also for a malfunction message or a pre-alarm, three digital inputs of the PLC are reserved for the smoke detector.

An oxygen deficiency, a fire alarm or another serious alarm might affect not only the ArDM experiment, but the entire underground laboratory. Thus, three digital outputs of the ArDM PLC are reserved for communication with the PLC of the underground laboratory. The outputs, dry contacts, are assigned to the oxygen deficiency, the fire alarm and a shared output for different alarms that are of interest to the underground laboratory. In addition, a digital input is reserved to receive alarms from the laboratory. Also this signal is transmitted using a dry contact.

[13] Alpha Omega Instruments, OXY-SEN

Chapter 5

Installation of the ArDM Control System at LSC

Due to the small WIMP-nucleon cross section a good shielding from cosmic muons is essential for direct dark matter search. Therefore, the ArDM experiment will be operated in the Canfranc Underground Laboratory (Laboratorio Subterráneo de Canfranc, LSC) in the Pyrenees. The laboratory is located below the Mount Tobazo and provides 2450 meters water equivalent shielding. At sea level the average cosmic muon flux in a horizontal detector is roughly 1 $cm^{-2}min^{-1}$ [37]. The cosmic muon flux in the Canfranc Underground Laboratory is reduced to about $2 \times 10^{-7} cm^{-2}s^{-1}$ [88]. The laboratory also provides a very low radioactive environment. The neutron flux due to radioactivity of the surrounding rock is 3.8×10^{-6} $cm^{-2}s^{-1}$ [88]. This chapter gives an overview of the installation at LSC and describes the recommissioning of the vacuum control system after the transport to Canfranc.

5.1 Overview of the Setup at LSC

In February 2012 the cryogenic system and the control system of ArDM have been shipped to the Canfranc Underground Laboratory. After two days of transport, they have been installed within 10 days in the laboratory. A new working platform with two floors supports the cryogenic system, including the detector vessel, the liquid purification system and the condenser unit. Figure 5.1 shows an overview of the setup in Canfranc.

The seven racks containing the ArDM control system were shipped in one piece and are now located 1.2 m away from the platform. The distance of the racks to the detector vessel is about 5 m and thus bigger than at CERN. Therefore, it was necessary to install longer cables connecting the instrumentation with the control system. This opportunity was used to implement a new kind of cabling: Two distribution boxes were installed on the platform. One is located on the lower floor, the other one on the upper floor of the platform. All the sensors are connected with relatively short cables to one of these distribution boxes. There the signals are collected in bigger cables with up to 48 wires, that cover the longer distance from the distribution boxes to the electronic racks. This new cabling has the advantage to reduce the amount of cables between the platform and the racks drastically compared to the cabling at CERN, where all the sensors were directly connected to the racks, and facilitated the re-cabling at the Canfranc Underground Laboratory. Also the 24 V signals for actuating the electromagnetic valves as well as the power cables for the heaters of the cryocoolers are routed through the distribution boxes. To avoid noise on the signal cables, the 230 V power cables for the pumps do not pass the distribution boxes and are cabled in an analogous manner as at CERN.

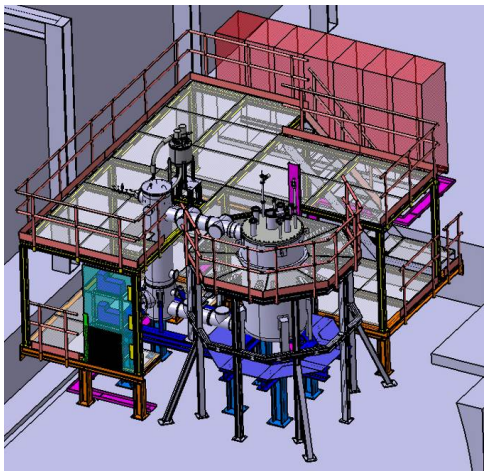

Figure 5.1: The ArDM setup in the Canfranc Underground Laboratory: The cryogenic system installed on the new working platform and the seven electronic racks containing the ArDM control system.

Instruments	**Distribution box first floor**	**Distribution box second floor**
temperature sensors	TE 10 – 19, 29 – 41, sensors heating bands 1 – 3	TE 00 – 09, 20 – 27, 42 – 45
pressure sensors	PI 06 – 08, PE AComp	PI 00 – 04
vacuum sensors	PE 02, 04, 05	PE 00, 01, 03
gate valves	status GV 2, 3 power GV 2, 3	status GV 1 power GV 1
turbomolecular pumps	control TP 2, 3	control TP 1
oxygen sensors	oxygen sensors 1 – 3	
electromagnetic valves	power EV 19 – 22	power EV 23, 24
heaters cryocoolers		power heaters 1, 2

Table 5.1: Overview of the equipment connected to the distribution boxes on the first and second floor. The positions of the equipment and the cabling are shown in Figure 5.2.

The positions of the two distribution boxes are shown in Figure 5.2 in dark green. The path of the cables connecting the distribution boxes to the racks and the cable trays for the cables between the distribution boxes and the equipment are also indicated. From these cable trays the cables branch off to reach the different instruments. When defining the path of the cables, it was paid attention to keep them as short as possible. Wherever possible, the cable trays were installed below the working platform (dashed lines in Figure 5.2) to avoid bothering people working on the platform. Table 5.1 gives an overview of the sensors connected to the distribution boxes on the first and on the second floor, respectively. The distribution box on the first floor is shown in Figure 5.3.

All the cables were prefabricated at CERN and already tested by connecting them to the equipment before shipment. Therefore, they only had to be re-connected in the Canfranc Underground Laboratory, which saved time during the installation. After the cabling and the

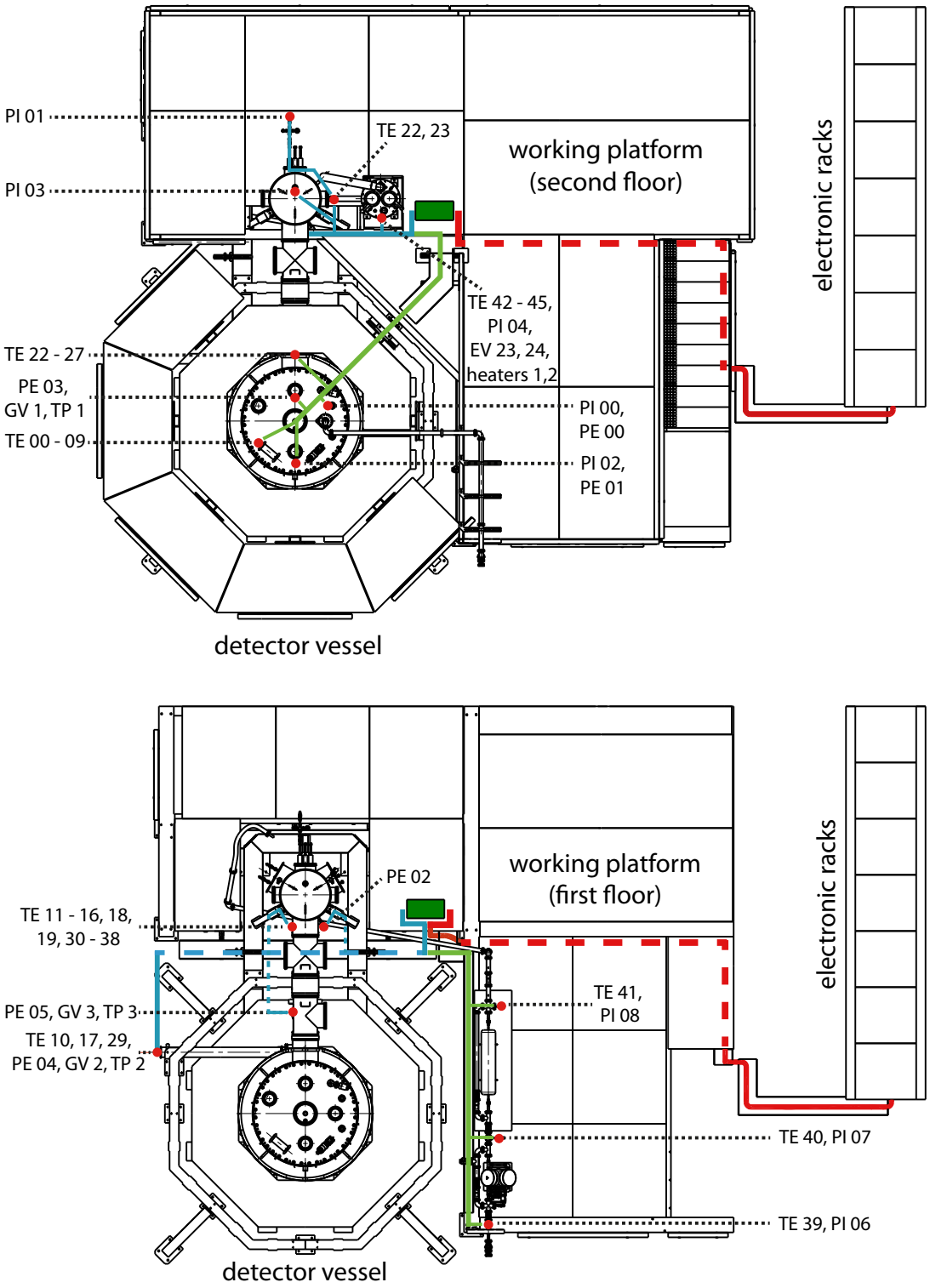

Figure 5.2: Top view on the first (bottom) and the second floor (top) of the ArDM working platform showing the position of the distribution boxes (dark green) and the cable trays. The red lines indicate the multicore cables between the distribution boxes and the electronic racks. The thick blue and light green lines show the cable trays for the cables connecting the instruments to the distribution boxes. These cables are illustrated with thin blue and light green lines. The dashed lines indicate where the cables are routed below the working platform.

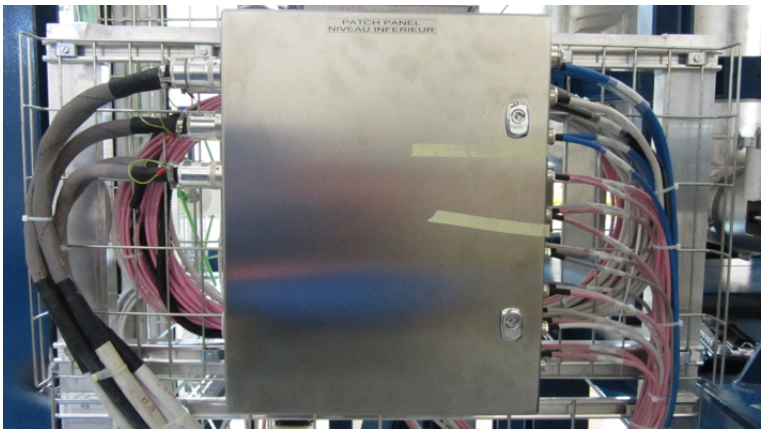

Figure 5.3: The distribution box on the first floor. The signal cables are entering from the right side and the multicore cables, which connect the distribution box to the racks of the ArDM control system, leave the distribution box on the left side.

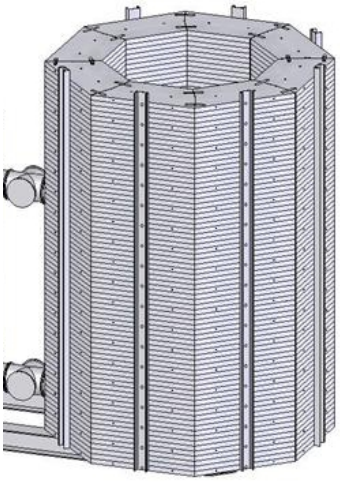

Figure 5.4: Polyethylene neutron shield surrounding the ArDM detector. The top shield is not shown. The figure is taken from Reference [80].

installation of the cryogenic and the control system, all the signals were retested and no damage from the transport was found. As a next step the commissioning of the vacuum system, which is described in the next section, followed. The monitoring of the cryogenic system and the cooling control system will be tested when the ArDM detector arrives in Canfranc and the system will be filled with liquid argon for the first time in the Canfranc Underground Laboratory.

After the commissioning of the vacuum control system, the neutron shield was installed around the detector vessel. It consists of 50 cm thick trapezoidal polyethylene blocks, which are arranged in an octagon around the detector vessel. Below and above the trapezoidal blocks a bottom and top shield close the neutron shield. The top shield is not yet in place, but will be mounted as soon as the detector is installed in the detector vessel. To cover the detector completely, also in the horizontal tubes of the vacuum insulation 2, which connect the detector vessel with the liquid argon purification system, two cylindrical polyethylene blocks were placed. They are 50 cm long and fill the tubes of the vacuum insulation over this length completely with the exception of a slit allowing the liquid argon tubes to pass. The total mass of the polyethylene shield including the top and the bottom shield is about 17 tons. A detailed Monte Carlo simulation [89] of

the neutrons from the rock of the LSC cavern showed that the neutron shield reduces the rate of neutrons hitting the detector vessel from about 12 000 neutrons per hour without shield to 0.7 neutrons per day. Only 12% of them, which correspond to 0.08 neutrons per day, have an energy above 100 keV and thus produce a nuclear recoil detectable with ArDM [89]. A drawing of the neutron shield is shown in Figure 5.4.

5.2 Commissioning of the Vacuum Control System at LSC

As the vacuum control system was already commissioned entirely at CERN, commissioning at the Canfranc Underground Laboratory could be done quickly. All the processes were designed for operation at LSC and already tested at CERN. The main items to check were to make sure that the hardware was not damaged during the transport and the new cables were connected properly. The starting and stopping processes were carried out for all the three pumping systems and worked correctly.

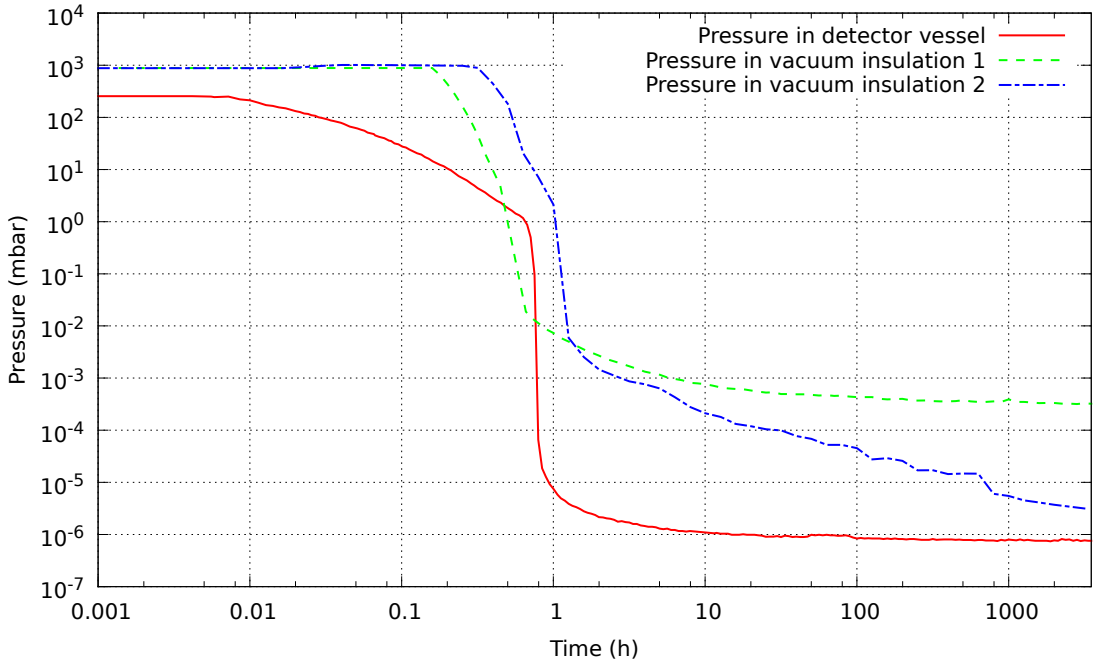

Figure 5.5: Commissioning of the vacuum control system: Pressure in the detector vessel and the two vacuum insulations from March to August 2012.

Since March 2012 the pumping systems are running without causing any problems. Figure 5.5 shows the pressure in the detector vessel and the two vacuum insulations over a period of five months starting from the commissioning in March 2012. The irregularities of the pressure in the vacuum insulation 2 are due to fluctuations of the vacuum sensor PE 02. The pressure curve of the vacuum insulation 1 is limited to 5×10^{-4} mbar, which corresponds to the lower limit of the measurement range of the Pirani vacuum sensor PE 01. In contrast to that, the sensors of the detector vessel and the vacuum insulation 2 include a Pirani and a cold cathode gauge. Thus, they have a wider measurement range with a lower limit of 5×10^{-9} mbar. The pressure in the vacuum insulation 2 decreases slower than the pressure in the detector vessel. This is due to the outgassing of the material in the vacuum insulation 2, which consists mainly of the two cylindrical polyethylene blocks of the neutron shield.

Also the process shutting down the vacuum pumps in case of a power cut was tested for the empty detector vessel under real conditions. All the pumping systems were shut down according to the processes. Also in the event of a power cut, the vacuum system is properly regulated by the control system.

The ArDM control system allows to run the pumping systems without manpower on site. The vacuum system can be monitored remotely via the PVSS user panels. The user panels also allow to actively intervene in case of an irregularity, which has not been necessary so far. The PVSS alarm management tool was tested and sends e-mails and text messages in case of irregularities. In the current situation manpower is required in Canfranc only from time to time for maintenance work.

Chapter 6

Measurement of the Electronic Recoil Contamination of Nuclear Recoil Events

As described in Section 2.1 scintillation light in liquid argon is produced by the decay of argon excimers. Two different excimer states emit scintillation light: the singlet and the triplet state. The singlet state with a lifetime τ_1 of about 7 ns emits the fast component of the scintillation light. The triplet state with a lifetime τ_3 of about 1.6 μs produces the slow component [1]. As the relative intensity of the two components depends on the ionisation density, it can be used to determine the type of particle producing an event. The pulse shape discrimination (PSD) is important for direct dark matter search experiments as it allows to distinguish between electronic recoil background from β or γ radiation and nuclear recoil signals from WIMPs.

In this chapter the response of the ArDM detector to nuclear recoils in single phase configuration is investigated using a neutron source. By means of a γ source the electronic recoil contamination, the probability of incorrectly identifying an electronic recoil event as nuclear recoil event, is measured. Pulse shape discrimination is used to distinguish between electronic and nuclear recoil events. For this purpose the component ratio CR defined as

$$CR = \frac{\text{collected light of the fast scintillation component}}{\text{total collected scintillation light}} \tag{6.1}$$

is calculated. The measured values for CR are about 0.3 and 0.7 for electronic recoils and nuclear recoils respectively and depend slightly on the recoil energy [90, 91].

6.1 Data Taking in September 2010

In September 2010 the ArDM detector was filled with liquid argon to test the cryogenic system and the light read out with the bottom PMT array. Before filling, the detector was evacuated for about two months to clean it from impurities and minimise the out-gassing of the detector components. A pressure of 5×10^{-7} mbar was achieved. The procedure to fill the detector with liquid argon was the same as during the run in spring 2009, described in Section 3.1: First the liquid argon bath was filled to cool down the detector vessel. Then the detector was filled with argon gas before filling it with liquid argon in two steps. The filling in two steps allows the system to reach a thermal equilibrium and cool down the top flange of the detector vessel, before the detector is filled to the top. As the top flange strongly contributes to the heat input of the detector, the cooling of the top flange facilitates the filling of the second half of the detector.

During the run the detector was exposed to the following external radioactive sources to test the response of the detector:

- a 20 kBq ^{22}Na source which is a β^+ emitter. By annihilation of the e^+ with an e^- two 0.511 MeV γs are emitted back-to-back. At the same time a 1.275 MeV γ from the de-excitation of the daughter ^{22}Ne* nucleus is emitted.
- an ^{241}Am-Be source emitting 3×10^4 neutrons per second. The ^{241}Am-Be source is described in more detail in Chapter 6.2.

The data recorded with the ^{241}Am-Be source are used in this chapter to investigate the detector response to nuclear recoils. By means of the ^{22}Na data the electronic recoil contamination is measured.

6.2 Recoil Energies from Neutrons emitted by the ^{241}Am-Be Source

The ^{241}Am-Be source used during the run in September 2010 is an alloy of ^{241}Am and ^{9}Be. The ^{241}Am isotope decays into ^{237}Np emitting α particles, predominantly with energies E_α = 5.486 MeV and 5.443 MeV, and γ rays, primarily with energy E_γ = 59.6 keV [92, 93]. Per α particle 0.36 γs of this energy are emitted. The half-life of the ^{241}Am is 432.2 years. The α particles absorbed by the beryllium create neutrons by the (α,n) reaction

$$^{9}\mathrm{Be} + \alpha \longrightarrow {}^{12}\mathrm{C}^* + n. \tag{6.2}$$

The neutron energy spectrum shows two broad maxima around 3.3 MeV and 5.2 MeV and extends up to 11.5 MeV (see Figure 6.1). The ^{241}Am-Be source also emits prompt 4.43 MeV γs from the de-excitation of the ^{12}C*.

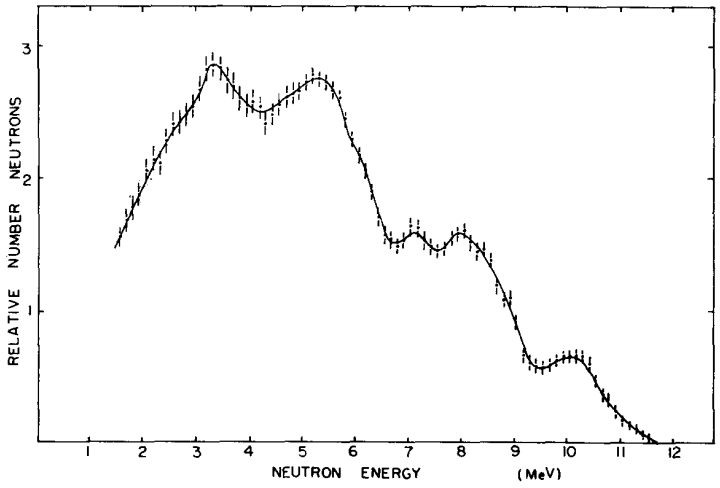

Figure 6.1: Spectrum of neutrons from ^{241}Am-Be source[1] [94].

The neutrons emitted by the ^{241}Am-Be source are detected in ArDM via elastic scattering on the argon nuclei. The recoil energy of the argon nucleus depends on the energy of the incident neutron and the scattering angle. For elastic scattering the recoil energy E_r is given by

$$E_\mathrm{r} = 2E_\mathrm{n}\frac{m_\mathrm{n}m_\mathrm{Ar}}{(m_\mathrm{n}+m_\mathrm{Ar})^2}(1-\cos\theta), \tag{6.3}$$

[1]Reprinted from Nuclear Instruments and Methods, 73, M.N. Thompson and J.M. Taylor, Neutron spectra from Am-α-Be and Ra-α-Be sources, 305 - 308, 1965, with permission from Elsevier.

where E_n is the incident neutron energy, θ is the scattering angle in the center-of-mass system, m_n is the neutron mass and m_{Ar} is the mass of the argon nucleus. This formula can be obtained by applying energy and momentum conservation to the elastic scattering. The maximum recoil energy caused by a neutron from the ^{241}Am-Be source is

$$E_{r,max} = 4E_{n,max}\frac{m_n m_{Ar}}{(m_n + m_{Ar})^2} \approx 1.1 \text{ MeV}. \tag{6.4}$$

The light collection yield of ArDM has been measured to be 0.7 photoelectrons per keV of electronic-equivalent recoil energy (p.e./keVee) [95]. As already described in Section 2.1, the light yield from nuclear recoils differs from the light yield of electronic recoils due to quenching processes. The scintillation efficiency L_{eff}, defined as the ratio of the scintillation light yield for nuclear recoil events relative to electronic recoil events, is ∼0.25 [50, 51]. For ArDM this gives a light collection yield for nuclear recoils of ∼0.18 p.e./keVnr. Thus, the maximum number of detected photoelectrons from a single scattered neutron is 193.

6.3 Trigger Configuration

The data analysed in this chapter were triggered externally with a NaI crystal. The radioactive sources were placed 23 cm from the detector vessel at four different heights. The NaI crystal was located at the same height 7 cm from the source as shown in Figure 6.2. The lowest source position (A) has been chosen to be at the height of the ArDM cathode. The other positions are 10 cm (B), 20 cm (C) and 30 cm (D) above the cathode.

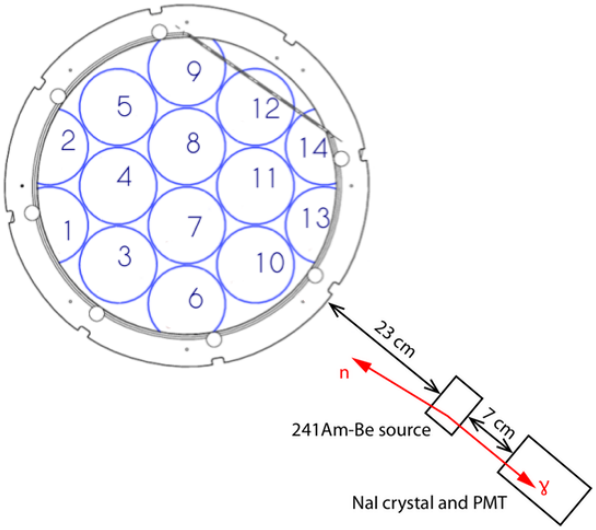

Figure 6.2: Sketch of the trigger configuration: top view on the bottom PMT array, radioactive source (here ^{241}Am-Be source) and NaI crystal used as trigger.

For the ^{241}Am-Be source the energy threshold on the NaI crystal signal for triggering an event was set to 2.5 MeV to avoid triggering on the low energetic γs from the ^{241}Am decay. During the measurements with the ^{22}Na source a lower threshold for the energy deposition in the NaI crystal of 511 keV was set to trigger an event. To estimate the number of events with pile-up or random coincidences, a background run was recorded with each source. For the background runs the events were triggered 10 μs after the energy deposition in the NaI crystal had been registered. Table 6.1 gives an overview of the data analysed in this chapter.

Type	**Trigger**	**Position**	**Number of events**
^{241}Am-Be	external trigger (2.5 MeV)	B	899467
^{241}Am-Be, background	external trigger (2.5 MeV, +10μs)	B	460774
^{22}Na	external trigger (511 keV)	A	2031220
		B	2411621
		C	598076
		D	906798
^{22}Na, background	external trigger (511 keV, +10μs)	B	281994

Table 6.1: List of September 2010 data presented in this chapter.

Figure 6.3 shows the energy spectrum of the photons from the ^{241}Am-Be source, which were detected in the NaI crystal and triggered an event. The energy calibration is taken from the 511 keV peak of the ^{22}Na source spectrum measured with the same NaI crystal, which is presented in [95]. In Figure 6.3 the peak at 4.43 MeV from the de-excitation of the ^{12}C* is well visible. Around 3.9 MeV and 3.4 MeV the single and double escape peaks can be observed.

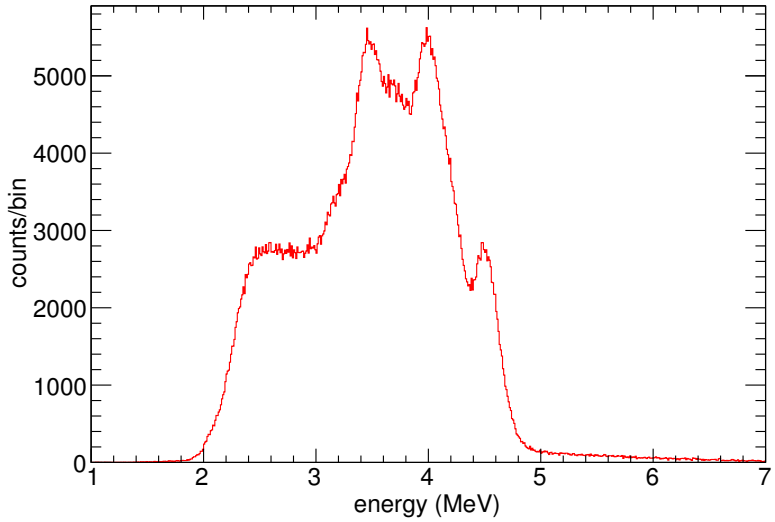

Figure 6.3: Spectrum of the photons emitted by the ^{241}Am-Be source. The spectrum was measured with the NaI crystal and shows the energy of the photons triggering an event.

6.4 Analysis of the PMT Signals

For every event the signals of the 14 PMTs have been registered for 2048 time samples starting 250 time samples before the trigger time. A time sample corresponds to 4 ns. Two typical PMT signals for neutron and γ events recorded with the ^{241}Am-Be source are presented in Figure 6.4. They illustrate the different component ratios for neutron and γ events. For both events the sum of the signals of all 14 PMTs is shown.

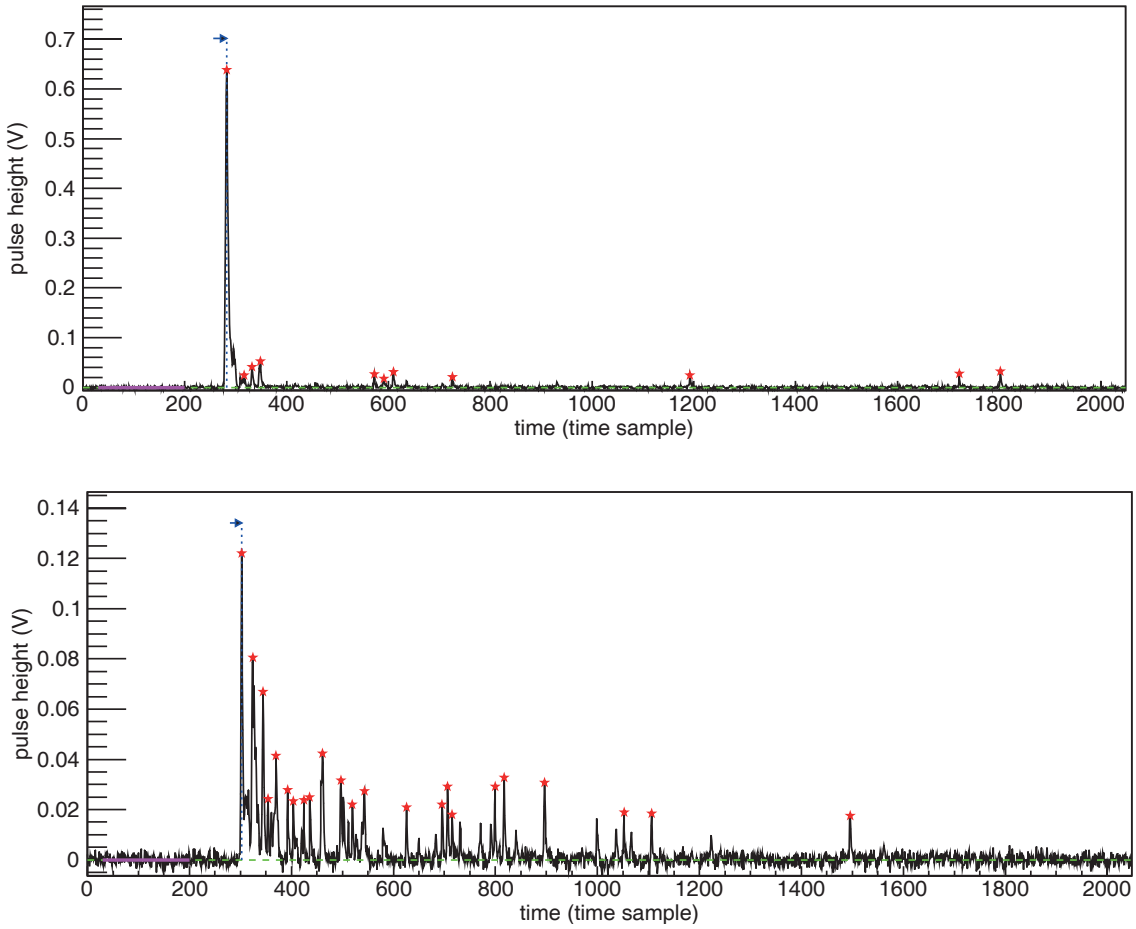

Figure 6.4: Typical PMT signals (sum of all 14 PMTs) for a neutron event (top) and a γ event (bottom). The events were recorded while the detector was irradiated with the ^{241}Am-Be source. The red stars indicate the peaks found by the peak finding algorithm while the blue arrow points to the peak time.

The PMT signals are analysed using LRAnalysis [96], a software framework especially developed for the analysis of the ArDM light readout signals. LRAnalysis is able to analyse input data stored as ROOT [97] files by the ArDM data acquisition software. It consists of a set of libraries, an analysis program and an event display program. The analysis program applies the following procedure to all the PMT signals as well as to the sum of the 14 PMT channels: First it performs a pedestal analysis, before it evaluates the integral of the signals and executes a peak finding algorithm.

The pedestal analysis evaluates the pedestal of the signal in the first 200 time samples where no event is expected. The mean of the signal and its standard deviation σ are calculated in this region. As this region can be contaminated by single photoelectrons, in a next step the signal is masked, where it exceeds the mean calculated before by more than 4σ. Then the mean and the σ are recalculated considering only not masked time samples. This procedure is repeated until the number of considered time samples does not differ by more than 1% from the number of time samples considered in the previous iteration. The final mean value of the signal in the pedestal region is then subtracted from the signal over the full signal length.

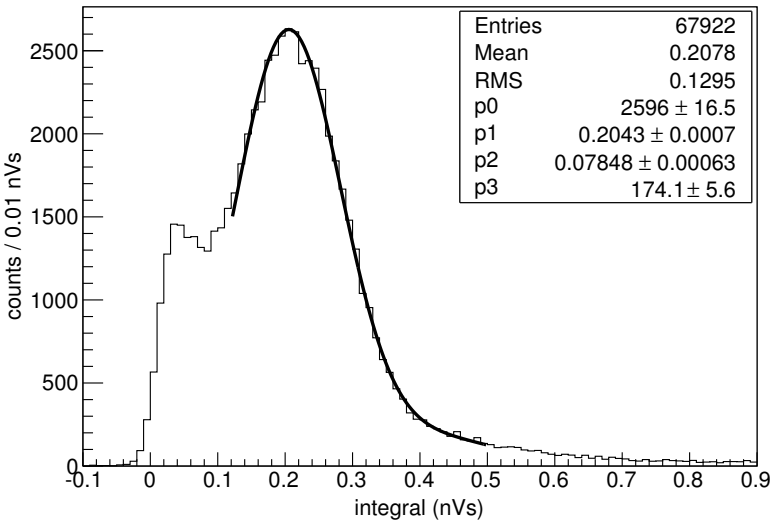

Figure 6.5: Integral of the single photoelectron signals of PMT 1. The distribution is fitted with the sum of two Gaussian functions. The parameters p0 and p3 are the amplitudes of the two Gaussian functions, p1 is the mean of the single photoelectron Gaussian, which is used as calibration of the PMT, and p2 is its standard deviation.

The signal integration algorithm first determines the peak time, the time of the maximum of the sum of the 14 PMT signals in the signal region. The signal region starts after the 200 time samples of the pedestal region and extends to 2000 time samples. The start time for the signal integration is set to the first time sample right before the peak time, where the signal falls below the mean of the pedestal plus 3σ. The signal is integrated from this start time to 4.5 μs after the peak time. Thus, the total integration time corresponds to about $3{\cdot}\tau_3$. Also here the signal is only integrated, if it is not masked. In the signal integration algorithm the mask is reversed compared to the pedestal analysis, i.e. the signal is integrated, if it exceeds the mean of the pedestal by more than 4σ. Besides the total integral, the signal integration algorithm also evaluates the integral of the fast component of the scintillation light by integrating the signal in the same manner as described above from the start time to 50 ns after the peak time, which corresponds to about $7{\cdot}\tau_1$. Due to the large difference in lifetimes the fraction of the light collected in this interval is a good estimate of the relative intensity of the fast component.

A peak finding algorithm then looks in the signal region for all the single peaks with an amplitude higher than the mean of the pedestal plus 10σ. It registers the amplitude, the time of the maximum and the integral of the peak. These characteristics of the single peaks will be used in the following section for selecting data samples of neutron and γ events, which are as clean as possible.

The PMTs are calibrated using the integral of the signals of single photoelectrons. For every run of 20 min to 1 h duration, a new calibration was done by calculating the integral outside the signal region over an interval of 100 time samples for every PMT. The distribution of these integrals is shown for PMT 1 (see Figure 6.2) in Figure 6.5. For every PMT the distribution of the integrals has been fitted with the sum of two Gaussian functions with mean values μ and 2μ and standard deviations σ and $\sqrt{2}\sigma$ to consider the possibility that some peaks may include two photoelectrons. The mean value of the first Gaussian function μ (p1 in Figure 6.5) corresponds to the mean integral of a single photoelectron and is used as calibration of the particular PMT.

The mean integral of one photoelectron is about 0.2 nVs for all PMTs. The values for the 14 PMTs were stable during the whole test in September 2010.

6.5 Selection of Nuclear Recoil Events

6.5.1 Event Selection

The recorded event samples do not only contain events caused by exactly one neutron or photon emitted by the source, but also events with pile-up or a random coincidence with other particles, which can originate from the background or also from the source. The following characteristics of the events, which are provided by LRAnalysis, are used as selection criteria to obtain a sample of events with as few as possible of such pile-up or random coincidence events:

- the peak time
- the mean and the standard deviation of the signal in the pedestal region
- the total energy of the event
- the total number of peaks
- the time of the highest peak relative to the first peak in the signal region
- the number of peaks in the integration region of the slow component of the scintillation light.

These selection criteria were applied to all the data listed in Table 6.1, i.e. to the data from the ^{241}Am-Be source and the ^{22}Na source as well as to the background runs of both sources.

The peak time of an event depends on the position of the interaction of the neutron or photon with the argon in the detector and, in case of the neutron, also on the particle energy. The peak time distribution shows that the clean neutron and γ events form a peak with a maximum around 280 time samples. Thus, only events with peak time between 270 and 320 time samples are selected. This corresponds to 80 to 280 ns after the trigger time. In Figure 6.6 (left) the peak time distribution for the ^{241}Am-Be source is shown.

A pile-up of two events or the random coincidence of a particle in the detector with a photon depositing energy in the NaI crystal can contaminate the pedestal region and lead to increased mean and standard deviation of the signal in the pedestal region. Thus, a cut is performed on both the mean and the standard deviation of the signal in the pedestal region. This cut is applied event by event on the sum of the signals of all 14 PMTs. The distribution of the standard deviation of the signal in the pedestal region is shown in Figure 6.6 (right). Only events with a mean smaller than 0.1 mV and a standard deviation smaller than 3 mV are selected.

After the three cuts described above still a lot of events with a component ratio close to one are left, which can neither be assigned to the electronic recoil events nor to the nuclear recoil events. To reject these events a cut on the time of the highest peak in the sum of the 14 PMT signals is applied. Only events with less than 50 ns between the first peak in the signal region and the highest peak are selected. Thereby overlapping events can be rejected. To identify events which are triggered by a photon in the NaI crystal, but the corresponding neutron or photon does not give any signal in the detector, two cuts on the number of peaks are applied.

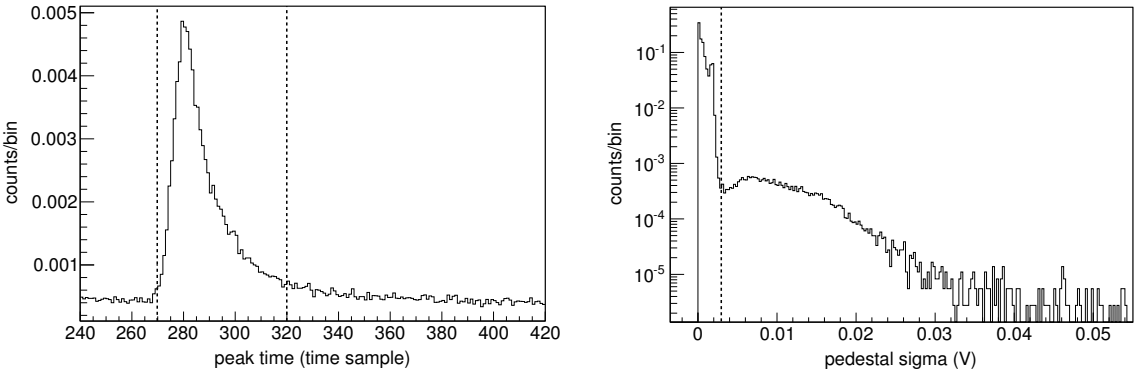

Figure 6.6: Illustration of the two first cuts applied to select neutron and γ events. *Left:* Normalised peak time distribution. The events with a peak time between 270 and 320 time samples are selected. *Right:* Normalised distribution of the standard deviation of the signal in the pedestal region. The events below 3 mV are selected.

The total number of peaks is forced to be bigger than one and at least one of the peaks has to be in the integration region of the slow component, that means more than 50 ns after the peak time.

Figure 6.7 shows the component ratio with respect to the amount of collected light for the events from the ^{241}Am-Be source, which passed all the cuts described above. Two groups of events are visible: the electronic recoil events with component ratio around 0.3 and the nuclear recoil events with component ratio around 0.7. The maximum energy of the nuclear recoil events is about 350 p.e.. This corresponds to a maximum nuclear recoil energy of 1.9 MeVnr.

To reject photons from the ^{22}Na source, which are incorrectly identified as neutrons and thus contribute to the electronic recoil contamination, a cut on the energy of the events is applied and only events with energies below 350 p.e. are selected. The fractions of events left after each cut described above are listed in Table 6.2 for both sources and all the source positions. The table shows that the fraction of selected events does not depend on the position of the ^{22}Na source.

		Peak time	**Mean and σ pedestal**	**Time first – highest peak**	**Number of peaks**	**Energy**
^{241}Am-Be	**B**	10.0 %	9.2 %	6.1 %	5.4 %	3.9 %
^{241}Am-Be, Bg	**B**	2.5 %	2.1 %	0.99 %	0.55 %	0.52 %
^{22}Na	**A**	22.1 %	16.1 %	8.5 %	8.3 %	7.1 %
	B	19.3 %	14.3 %	7.3 %	7.1 %	5.9 %
	C	21.0 %	15.3 %	8.3 %	8.1 %	6.7 %
	D	20.4 %	15.1 %	7.8 %	7.6 %	6.6 %
^{22}Na, Bg	**B**	3.5 %	2.7 %	1.2 %	0.81 %	0.77 %

Table 6.2: Fraction of events selected by the cuts described above. Bg indicates background run, A, B, C and D the source position.

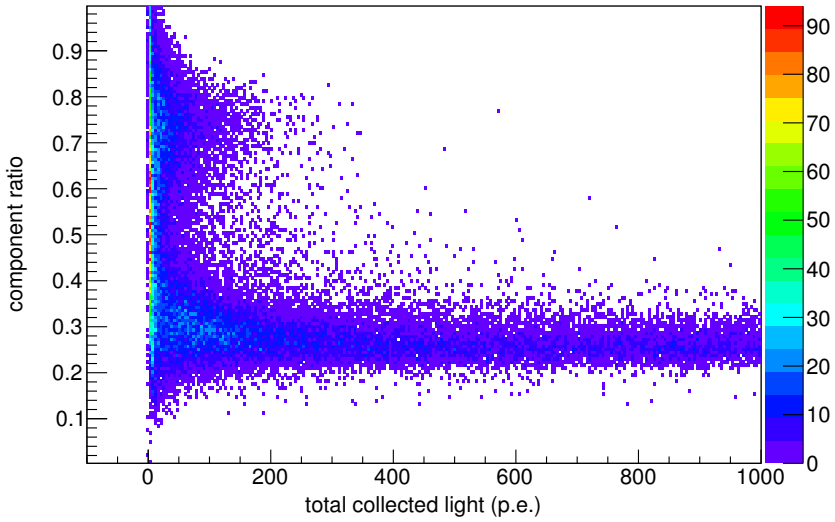

Figure 6.7: Distribution of the component ratio as a function of the integral of the collected scintillation light for the events from the ^{241}Am-Be source which passed all the cuts described above.

6.5.2 Pulse Shape Discrimination

After the event selection, a pulse shape discrimination is used to distinguish the nuclear recoil events from the electronic recoil events. For this purpose the distribution of the component ratio is analysed. The distribution of the component ratio after all the cuts, including the one on the energy, is shown in Figure 6.8 (top) for both sources. The distribution of the background runs have been normalised to the total number of events of the runs of the particular source. In the figure the normalised background distributions are superimposed over the distributions from the sources. The component ratio distribution without background events is obtained by subtracting the normalised background distribution from the distribution of the particular source. The difference is shown in Figure 6.8 (bottom). The electronic recoil peak of the distribution from the ^{22}Na source shows a tail towards the high component ratio region. This tail might be caused by γs producing extra light in one of the detector components or by photoelectron statistics. The component ratio distribution of the events from the ^{22}Na source is fitted with a Gaussian function with mean μ_{er} and standard deviation σ_{er} in the range $0.2 \leq CR \leq 0.32$ and, due to its tail, with an exponential function $\exp(a - b \cdot CR)$ in the range $0.4 \leq CR \leq 1$. Assuming that the electronic recoil events recorded with the ^{241}Am-Be source also show an exponential tail towards the high component ratio region, the component ratio distribution for this source is fitted with the sum of an exponential and a Gaussian function for the nuclear recoil events with mean μ_{nr} and standard deviation σ_{nr} in the range $0.4 \leq CR \leq 1$. The fit function in the range $0.2 \leq CR \leq 0.32$ stays the same Gaussian function for the electronic recoil events as for the ^{22}Na source. The fitted parameters are presented in Table 6.3.

The fit of the component ratio distribution for the ^{241}Am-Be source is now used to determine the component ratio region for selecting the nuclear recoil events. To reduce the contribution of the exponential tail of the electronic recoil events, only the events within the interval $[\mu_{nr} - \sigma_{nr}, \mu_{nr} + \sigma_{nr}]$ are accepted as nuclear recoil events. This corresponds to $0.635 \leq CR \leq 0.819$ and 68.27 % of the expected nuclear recoil events are selected. Table 6.4 shows the fraction of the recorded events (listed in Table 6.1), which are selected as nuclear recoil events, for the different

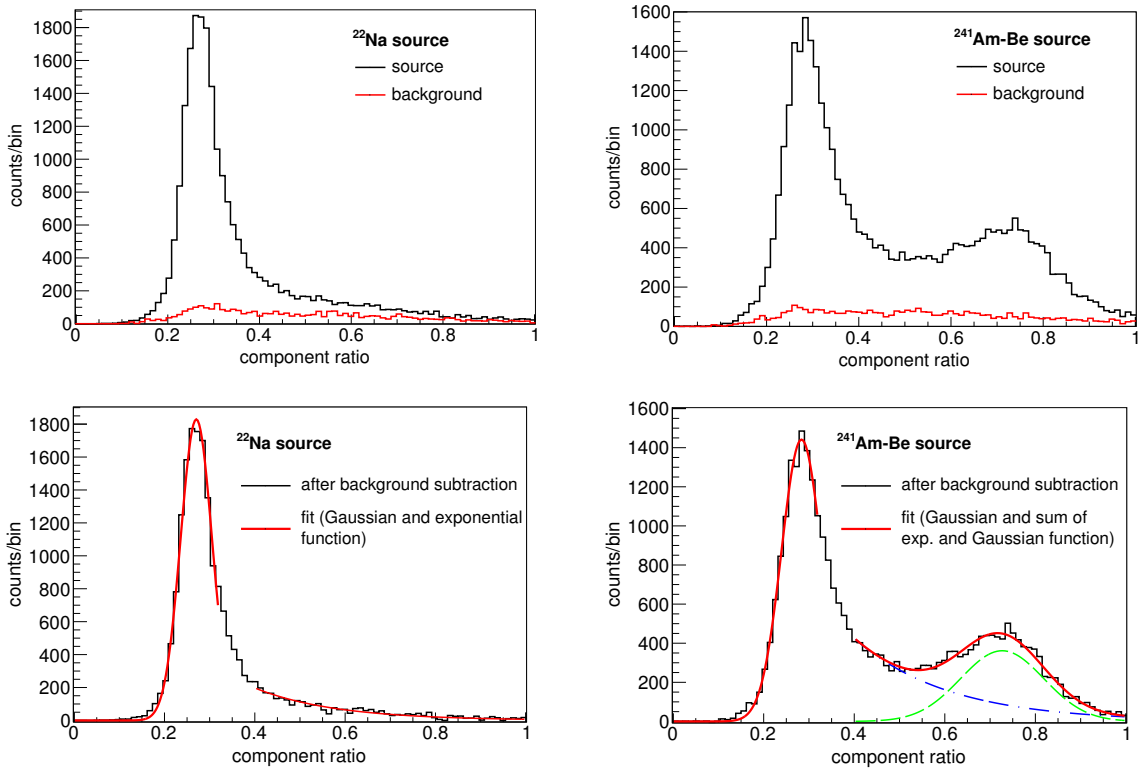

Figure 6.8: Distribution of the component ratio after all the cuts for the ^{22}Na source (left) and the ^{241}Am-Be source (right). *Top:* Superposition of the distributions from the sources (black) and the respective background runs (red). *Bottom:* Component ratio distribution after the subtraction of the background events. The distribution has been fitted with a Gaussian in the range $0.2 \leq CR \leq 0.32$ and an exponential function in the range $0.4 \leq CR \leq 1$ for the ^{22}Na source. For the ^{241}Am-Be source it is fitted with a Gaussian function in the range $0.2 \leq CR \leq 0.32$ and the sum of an exponential and a Gaussian function in the range $0.4 \leq CR \leq 1$.

	μ_{er}	σ_{er}	a	b	μ_{nr}	σ_{nr}
^{22}Na	0.270 ± 0.001	0.035 ± 0.001	7.52 ± 0.09	5.59 ± 0.18		
^{241}Am-Be	0.284 ± 0.001	0.044 ± 0.001	7.98 ± 0.05	4.83 ± 0.11	0.727 ± 0.002	0.092 ± 0.002

Table 6.3: Fit parameters of the component ratio distribution of the ^{22}Na source and the ^{241}Am-Be source. The definitions of the parameters are given in the text.

trigger conditions. As in Table 6.2 the numbers of selected events do not differ significantly for the four positions of the ^{22}Na source. As expected, a higher fraction of the ^{241}Am-Be events than of the ^{22}Na events survives the cut on the component ratio. The contribution from the background to the selected events is bigger for the ^{22}Na than for the ^{241}Am-Be source.

The energy spectra of the selected nuclear recoil events for the ^{241}Am-Be source are shown in Figure 6.9. The spectrum of the background run has been normalised to the total number of events from the ^{241}Am-Be source. The normalised background spectrum is superimposed on the measured spectrum of the source. For energies below 10 p.e. there is a significant contribution

		Selected nuclear recoil events
^{241}Am-Be	**B**	(0.80 ± 0.05) %
^{241}Am-Be, Bg	**B**	(0.09 ± 0.01) %
^{22}Na	**A**	(0.17 ± 0.02) %
	B	(0.19 ± 0.03) %
	C	(0.18 ± 0.02) %
	D	(0.19 ± 0.03) %
^{22}Na, Bg	**B**	(0.12 ± 0.01) %

Table 6.4: Fraction of events selected by pulse shape discrimination as nuclear recoil events for the different trigger conditions. Bg indicates background run, A, B, C and D the source position. The errors are only statistical.

from background events to the spectrum, whereas above 10 p.e. the spectrum contains almost no background events. To get the shape of the spectrum without background events the normalised background spectrum is subtracted from the measured spectrum of the source bin by bin. The number of events per bin of the resulting spectrum is exponentially decreasing. As described in Section 6.2, the recoil energy of the argon nuclei does not only depend on the energy of the incident neutron, but also on the scattering angle. Thus, the peaks of the emission spectrum of the ^{241}Am-Be source are not observable anymore. After the subtraction of the background events 0.71 % of the collected events remain.

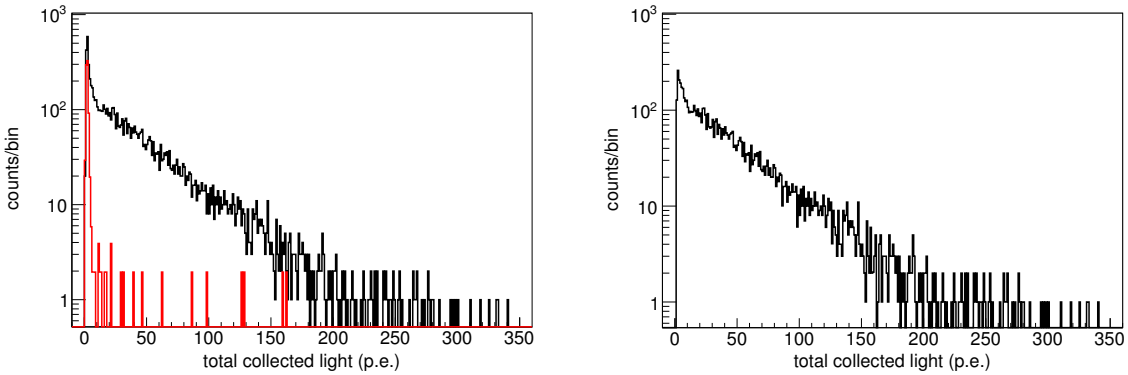

Figure 6.9: *Left:* Superposition of the energy spectra of the ^{241}Am-Be source (black) and the respective normalised background run (red). *Right:* Energy spectrum of the ^{241}Am-Be source after the subtraction of the background events.

6.6 Electronic Recoil Contamination of Nuclear Recoil Events

To estimate the electronic recoil contamination of the selected nuclear recoil events, the spectrum of the events from the ^{22}Na source, which are selected as nuclear recoil events, is determined. The events of the ^{22}Na source passing the cut on the component ratio are either real neutrons or photons, which are incorrectly identified as neutrons. In Figure 6.10 the superposition of the spectra of the ^{22}Na source and the background run, as well as the spectrum of the selected nuclear recoil events after the subtraction of the background events are shown. The number of

selected events above 20 p.e. is quite small and there was no contamination measured above 150 p.e.. In total 0.07 % of the collected events are left after the subtraction of the background events.

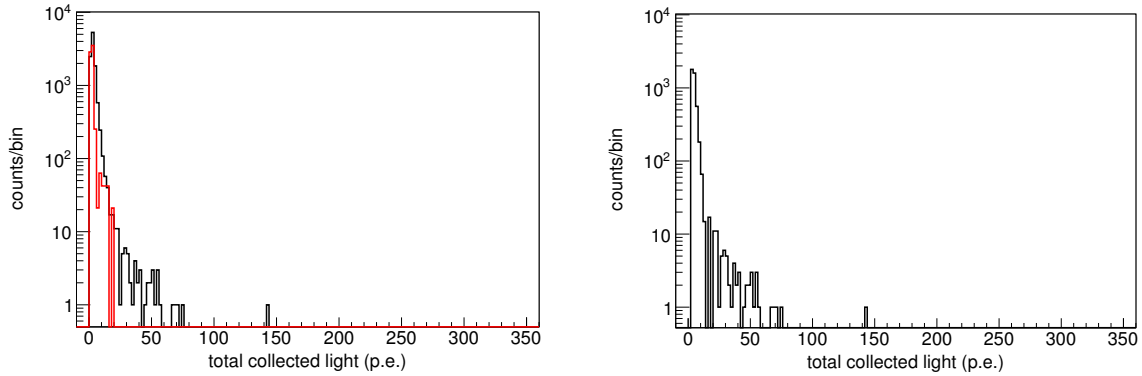

Figure 6.10: *Left:* Superposition of the energy spectra of the nuclear recoil events from the ^{22}Na source (black) and the respective background run (red). *Right:* Energy spectrum of the nuclear recoil events from the ^{22}Na source after the subtraction of the background events.

The electronic recoil contamination is estimated as the number of events from the ^{22}Na source with $0.635 \leq CR \leq 0.819$ divided by the total number of events from the ^{22}Na source. Figure 6.12 shows the electronic recoil contamination measured with pulse shape discrimination. For energies between 59 and 97 p.e. the electronic recoil contamination is $(9.8 \pm 4.9) \times 10^{-5}$, for energies between 36 and 59 p.e. it is $(1.0 \pm 0.2) \times 10^{-3}$. This corresponds to 8 contamination events between 59 and 97 p.e. and 84 contamination events between 36 and 59 p.e.. These values are valid for a nuclear recoil acceptance level of 68.27 %. The errors of the electronic recoil contamination are only statistical.
In the p.e. scale the obtained electronic recoil contamination is compatible with the results reported in Reference [90]. For the current light collection yield of ArDM the electronic recoil contamination in the region of interest, which is 30 to 100 keVnr, is 10^{-3} to 10^{-2} and significantly higher than the result from Reference [90]. This high value can be due to underestimation of the background neutrons in coincidence with a photon triggering an event in the NaI-crystal or to misidentified photons. Photons can for instance be misidentified because they produce extra light in one of the detector components or due to photoelectron statistics.

The number of photons which are misidentified due to photoelectron statistics is estimated with a Monte Carlo simulation. For every energy bin of the size of 1 p.e., photon events are generated. The detection times of the photoelectrons of each event are distributed according to the average pulse shape for electronic recoil events within the integration region, which is defined identically as for the data. The time samples in the simulation correspond to the 4 ns time samples of the PMT signals. For each event the component ratio is calculated. Photoelectrons with a detection time smaller than the peak time of the average pulse shape plus 50 ns contribute to the fast component, all the other photoelectrons contribute to the slow component. If the calculated component ratio is between 0.635 and 0.819, corresponding to the limits applied to the PMT signals and a nuclear recoil acceptance of 68.27 %, the event is incorrectly identified as a nuclear recoil event and contributes to the electronic recoil contamination. For every energy bin the number of misidentified photon events is counted and divided by the total number of photon events in that bin to enable a comparison with the measured electronic recoil contamination.

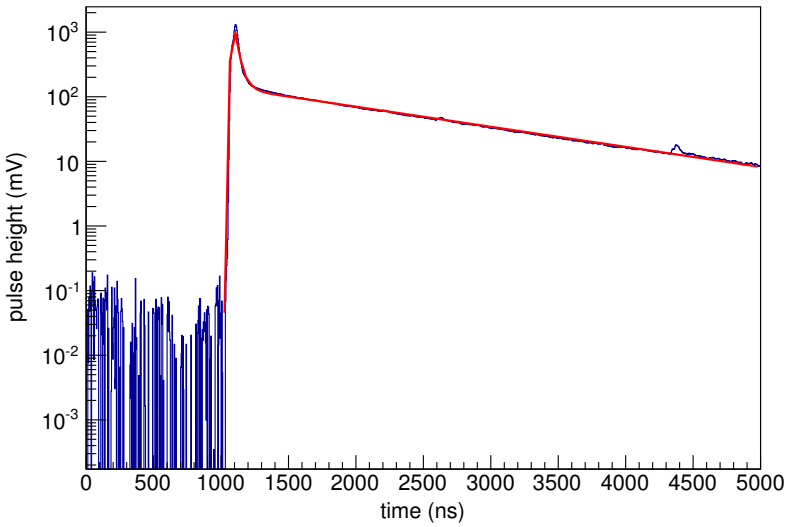

Figure 6.11: Average pulse shape for events with $0.235 \leq CR \leq 0.305$ fitted with Equation (6.6) (red) after baseline subtraction.

Two different average pulse shapes are used to generate the detection time of the photoelectrons:

- the average pulse shape for electronic recoil events measured with the current ArDM detector and
- the pulse shape from Reference [90].

The ArDM average pulse shape is generated by adding the pulse shapes of the events with $0.235 \leq CR \leq 0.305$, which pass all the cuts described in Section 6.5.1, and then dividing each time sample by the total number of considered events. The component ratio range was determined by the fit of the component ratio distribution for the ^{22}Na source. Events within the interval $[\mu_{er} - \sigma_{er}, \mu_{er} + \sigma_{er}]$ are selected. The baseline is calculated by determining the mean value in the pedestal region, where no signal is expected. It is then subtracted from the average signal over the full signal length. Figure 6.11 shows the average pulse shape after the baseline subtraction. The probability density function of the detection time of the photoelectrons is determined by fitting the average pulse shape with the convolution of the impulse response function of the PMTs, given by a Gaussian function $G(t - t_0, \sigma)$, and the decay function of the argon excimers:

$$f(t) = G(t - t_0, \sigma) * \left(H(t - t_0) \left(\frac{A}{\tau_1} e^{-\frac{t-t_0}{\tau_1}} + \frac{B}{\tau_2} e^{-\frac{t-t_0}{\tau_2}} + \frac{C}{\tau_3} e^{-\frac{t-t_0}{\tau_3}} \right) \right) \tag{6.5}$$

$$\begin{aligned} &= \frac{A}{2\tau_1} e^{\left(\frac{\sigma^2}{2\tau_1^2} - \frac{t-t_0}{\tau_1}\right)} \left(1 - \mathrm{erf}\left(\frac{\sigma^2 - \tau_1 (t - t_0)}{\sqrt{2}\sigma\tau_1}\right)\right) \\ &+ \frac{B}{2\tau_2} e^{\left(\frac{\sigma^2}{2\tau_2^2} - \frac{t-t_0}{\tau_2}\right)} \left(1 - \mathrm{erf}\left(\frac{\sigma^2 - \tau_2 (t - t_0)}{\sqrt{2}\sigma\tau_2}\right)\right) \\ &+ \frac{C}{2\tau_3} e^{\left(\frac{\sigma^2}{2\tau_3^2} - \frac{t-t_0}{\tau_3}\right)} \left(1 - \mathrm{erf}\left(\frac{\sigma^2 - \tau_3 (t - t_0)}{\sqrt{2}\sigma\tau_3}\right)\right). \end{aligned} \tag{6.6}$$

The parameters τ_1 and τ_3 are the decay times, while A and B are the intensities of the fast and the slow component of the scintillation light. The time t_0 is the peak time and $H(t - t_0)$ stands

for the Heaviside step function. The calculation of the convolution can be found in Appendix A. To improve the goodness of fit in the region between 50 and 200 ns after the peak time, a third scintillation light component, the intermediate component with decay time τ_2 and intensity B, is added to the fit function. Evidence for an intermediate component with a decay time of 20 – 40 ns has also been seen in References [1, 98]. The origin of this component is currently not well understood. It could come from an additional decay of argon excimers, but also from PMT effects, such as late pulses due to photoelectrons backscattering on the first dynodes or afterpulses induced by ionisation or luminescence of the residual gas in the PMT [99].

The results for the fit parameters are shown in Table 6.5. Compared to literature [1] the obtained decay times of the fast and the slow component of the scintillation light are rather small. This is due to the consideration of the intermediate component and possibly also to the special selection of the events. The fit of the average pulse shape of all the events without applying any selection criteria leads to longer decay times $\tau_1 = (4.9 \pm 1.0)$ ns and $\tau_3 = (1505 \pm 10)$ ns.

A (nVs)	B (nVs)	C (nVs)	τ_1 (ns)	τ_2 (ns)	τ_3 (ns)
38.2 ± 0.7	22.2 ± 0.6	186.5 ± 1.0	2.3 ± 1.0	40.4 ± 2.0	1396 ± 11

Table 6.5: Resulting parameters from the fit of the average pulse shape for events with $0.235 \leq CR \leq 0.305$. The average pulse shape is fitted with Equation (6.6).

The results of the simulation of the electronic recoil contamination with the average pulse shape of the current ArDM detector are shown in Figure 6.12. For every energy bin 10 000 photon events have been generated and the electronic recoil contamination has been calculated as explained above. This procedure has been repeated 1000 times and the average has been taken for every energy bin. This average is plotted in the figure in red.
For cross-checking these results, the same simulation was repeated with other average pulse shapes. In Reference [90] average pulse shapes are determined for 15 energy bins from 14 keVnr to 200 keVnr. When fitting these average pulse shapes only the fast and the slow, but not the intermediate component of the scintillation light were considered. The results of the simulation with these average pulse shapes are shown in Figure 6.12 in blue. The number of generated photon events and repetitions is the same as for the simulation with the pulse shape of the current ArDM detector.

The two simulations are in good agreement. For both simulations the fraction of photons, which are misidentified due to photoelectron statistics, decreases exponentially with increasing amount of collected light. The sudden rises in the electronic recoil contamination for certain numbers of photoelectrons are due to the number of possible combinations of the number of photoelectrons in the fast and the slow component time ranges. For example, for events with totally 8 photoelectrons only the combination of 5 photoelectrons in the fast component and 3 photoelectrons in the slow component gives events which are identified as nuclear recoil events. In contrast, for events with a total of 9 photoelectrons, there are two combinations contributing to the nuclear recoil events: 5 photoelectrons in the fast component and 4 of them in the slow component or 6 photoelectrons in the fast component and 3 of them in the slow component. This results in a higher contribution to the electronic recoil contamination for events with an energy of 9 photoelectrons than for events with an energy of 8 photoelectrons.

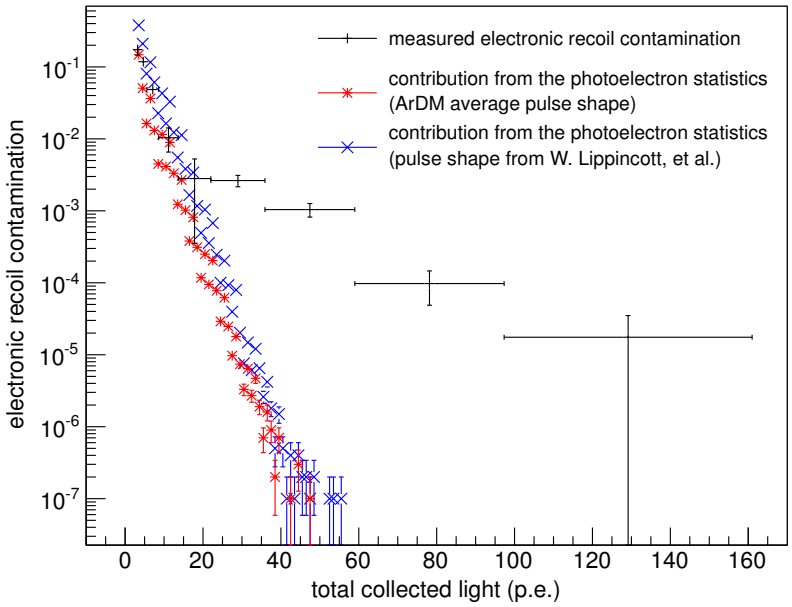

Figure 6.12: Measured electronic recoil contamination of the nuclear recoil events determined with pulse shape discrimination (black) and simulated contribution of the electronic recoil events, which are misidentified as nuclear recoil events due to photoelectron statistics. The red stars show the results of the simulation using the average pulse shape measured with ArDM as probability density function for the detection time of the photoelectrons. The blue crosses represent the simulation using the average pulse shapes from Reference [90]. Only statistical errors are shown for the measured electronic recoil contamination.

Both simulations show that for the current light collection yield of 0.7 p.e./keVee the electronic recoil contamination in the region of interest is dominated by photon events, which are incorrectly identified as nuclear recoil events due to photoelectron statistics. This can be counteracted by increasing the light collection yield of the detector. The following actions are taken to increase the light collection yield of ArDM:

- Twelve additional PMTs are going to be installed at the top of the detector for detection of the primary and secondary scintillation light.
- The existing PMTs of the bottom array will get a fresh TPB coating to counteract aging effects.
- A redesign of the reflector including the TPB coating is ongoing.

Above 30 p.e. the measured electronic recoil contamination stays significantly above the expectation from the photoelectron statistics. This can be due to an underestimation of the random coincidences of background neutrons and photons triggering an event in the NaI crystal. In this case the electronic recoil contamination can be reduced by operating the ArDM detector in the Canfranc Underground Laboratory. Another contribution to the electronic recoil contamination can be photons, which are incorrectly identified as neutrons, because they produce extra fast light in the detector components [90].

Assuming that the discrepancy between the measured electronic recoil contamination and the simulated contamination due to photoelectron statistics is only caused by underestimation of the random coincidences with backgrounds present on the surface, the simulated contribution of the photoelectron statistics to the electronic recoil contamination gives an estimate for the rejection power, which can be achieved with pulse shape discrimination at the Canfranc Underground Laboratory. The estimation of the rejection power expected for measurements in the Canfranc Underground Laboratory will be performed in Section 6.8. First, Section 6.7 gives an overview of the expected background in the underground laboratory and points out, which total rejection power is required to reduce the background rate from β and γ radiation to the order of the expected WIMP rate.

6.7 Expected Background Rates in the Canfranc Underground Laboratory

WIMP interactions with ordinary matter are very rare. For a WIMP mass between 30 and 100 GeV the spin-independent WIMP-nucleon cross section has been limited to values below 3×10^{-45} cm^2 by the XENON100 collaboration [27]. For a cross section of this size about 0.3 WIMP events per day per ton of argon are expected in the region of interest [52], which is defined as the nuclear recoil energy window from 30 to 100 keVnr. This small event rate requires very little background radiation or the capability to distinguish background events from the WIMP events.
To reduce the background induced by cosmic rays, the ArDM experiment will be operated in the Canfranc Underground Laboratory (Laboratorio Subterráneo de Canfranc, LSC) in the Pyrenees. It provides 2450 meters water equivalent of shielding. The cosmic muon flux in the laboratory is about a factor 10^5 smaller than above ground at sea level [88].

In the Canfranc Underground Laboratory the ArDM experiment has to deal with two different types of background:

- β and γ radiation with low LET and
- neutrons with higher LET.

While neutrons produce nuclear recoil signals, which are difficult to distinguish from WIMP events, the electronic recoil events from β and γ radiation can be rejected by means of pulse shape discrimination and the ratio of the ionisation charge over the scintillation light produced by the event, which is from now on called charge over light ratio. The origin of these two discrimination criteria is discussed in Section 2.1.

This section gives a short overview over the different background sources. Detailed Monte Carlo simulations to estimate the different background rates can be found in References [79, 100].

6.7.1 Background from β and γ Radiation

Two main sources contribute to the β and γ radiation background:

- γ radiation from uranium and thorium contaminations of the detector material and
- the β decay of the naturally occurring isotope ^{39}Ar.

γ background from the detector components
Most of the detector materials contain traces of uranium and thorium. Their decay chains produce γs at different energies. The uranium and thorium contaminations of the detector materials range from less then 1 to about 1000 ppb [79]. The borosilicate glass of the PMTs is expected to give the highest contributions to the γ background from the detector material. A screening of one of the Hamamatsu R5912-02MOD PMTs with a germanium detector showed, that the total gamma activity per PMT is 4 Bq [101].
A Monte Carlo simulation taking into account the two decay chains and the geometry of the detector was performed. It pointed out that in the ArDM detector the interaction rate of γs with an energy corresponding to a nuclear recoil energy of 30 to 100 keV is about 66 000 events per day [79].

^{39}Ar background
Commercially available argon is extracted from air by distillation. Atmospheric argon is composed of different argon isotopes. The most common isotopes are ^{40}Ar, ^{36}Ar and ^{38}Ar. They account for 99.60 %, 0.337 % and 0.063 % of the argon atoms in the atmosphere, respectively [102]. Also traces of the isotope ^{39}Ar are present in atmospheric argon. ^{39}Ar is mainly produced by cosmic rays interacting with the isotope ^{40}Ar in the stratosphere. The most dominant process of the ^{39}Ar production is the (n,2n) reaction [103]:

$$^{40}\mathrm{Ar} + \mathrm{n} \longrightarrow {}^{39}\mathrm{Ar} + 2\mathrm{n}. \tag{6.7}$$

The ^{39}Ar isotope is a β^- emitter. It decays to the stable isotope ^{39}K:

$$^{39}\mathrm{Ar} \longrightarrow {}^{39}\mathrm{K} + \mathrm{e}^- + \overline{\nu}_\mathrm{e}. \tag{6.8}$$

The half-life of ^{39}Ar is 269 years [102]. The energy spectrum of the emitted electrons is shown in Figure 6.13. The decay energy is $Q = 565$ keV and the mean energy of the electrons is 219 keV [104].

The measured activity of ^{39}Ar is (1.01 ± 0.08) Bq per kg of atmospheric argon [103, 105]. From the activity and the half-life, the ^{39}Ar mass fraction in atmospheric argon can be calculated to be $(8.0 \pm 0.6) \times 10^{-16}$ kg/kg [103, 105].
The event rate in the ArDM detector due to ^{39}Ar is of the order of 1 kHz. Assuming a scintillation efficiency L_eff of 0.25, the energy of the emitted electron has to be between 7.5 and 25 keV to generate an event in the region of interest. Only 3.5 % of the ^{39}Ar decays produce electrons in this energy range. Thus, an event rate of 35 Hz or 3×10^6 events per day in the region of interest is expected for the full ArDM detector. This event rate exceeds the rate from the background due to uranium and thorium contaminations of the detector material by more than an order of magnitude.

To reduce the background from β and γ radiation to the order of the expected WIMP rate a rejection power of 10^{-7} is required. As described above, two criteria can be combined to reject this class of background: the pulse shape discrimination and the charge over light ratio of the events. An estimation of the rejection power, which can be achieved with pulse shape discrimination at the Canfranc Underground Laboratory, and the consequences for the required rejection from the charge over light ratio are presented in Section 6.8.

To lower the dependency on the background rejection an other way to reduce the β and γ background might be possible. Replacing the atmospheric argon with ^{39}Ar depleted argon would decrease the ^{39}Ar background rate directly. Underground natural gas reservoirs contain

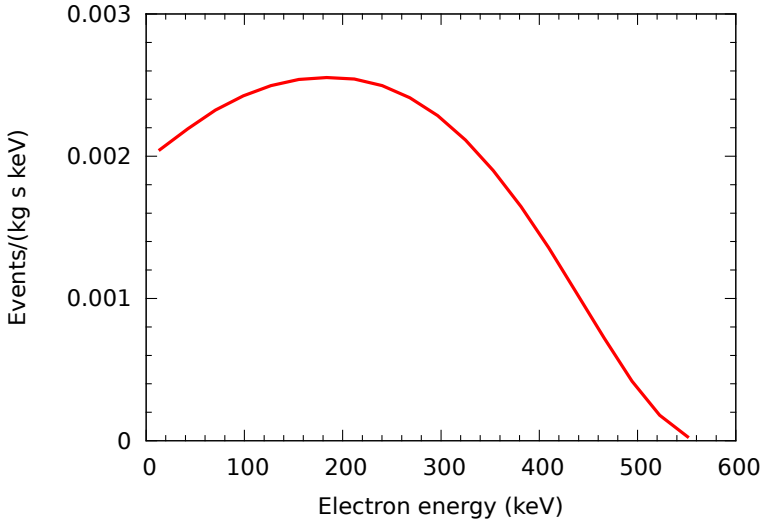

Figure 6.13: Beta spectrum of ^{39}Ar [104]. The decay energy is $Q = 565$ keV and the mean energy of the electrons is 219 keV.

small amounts of argon. The ^{39}Ar production is strongly suppressed underground due to the shielding of the cosmic rays by the rock. Thus, it is expected that the ^{39}Ar concentration in the argon from underground natural gas reservoirs is smaller than in atmospheric argon. Measurements by the WARP collaboration showed that the ^{39}Ar concentration in argon from the US National Helium Reserve, an underground natural gas reservoir in Texas, is smaller than 4×10^{-17} kg/kg and thus below 5% of the ^{39}Ar concentration in atmospheric argon [106].

6.7.2 Neutron Background

The neutron background is caused by two different sources:

- uranium and thorium contaminations of the detector material and the rock
- muon-induced neutrons.

Neutron background from radioactivity of the detector components and the rock
As the γ background, also the neutron background from the detector materials is due to uranium and thorium contaminations. The uranium and thorium decay chains contain several α decays with α energies of several MeV [79]. These α particles contribute to the neutron background by undergoing (α,n) reactions in the detector materials. A nucleus of the material can absorb an emitted α particle and emit a neutron with an energy of a few MeV [79].
Besides the two decay chains also the spontaneous fission of uranium contributes to the neutron background.

The biggest contribution to the neutron background from the detector components comes from the borosilicate glass of the PMTs. A Monte Carlo simulation taking into account the two decay chains and the geometry of the detector showed that about 2300 neutrons per year are emitted from the detector components [79]. Even though the neutron background rate is significantly smaller than the background rate from β and γ radiation, the neutron background is more critical. The neutrons generate nuclear recoils and are thus partially indistinguishable from WIMP interactions. Thus, it is essential to use low radioactive detector materials. Only neutrons, that scatter more than once on an argon nucleus in the detector, can be identified as background.

Due to the small WIMP-nucleon cross section, a WIMP is not expected to scatter more than once in the ArDM detector. Monte Carlo simulations showed that half of the neutrons interact more than once in the detector and the rate of neutrons from the detector material causing WIMP-like events is 0.07 events/day [79]. WIMP-like events are defined as events with only one interaction in the detector and a nuclear recoil energy between 30 and 100 keV.

Also uranium and thorium contaminations of the rock surrounding the ArDM experiment in the Canfranc Underground Laboratory contribute to the neutron background. The neutron flux from radioactivity of the rock in the laboratory is $(3.82 \pm 0.44) \times 10^{-6}$ cm^{-2}s^{-1} [88]. To reduce the background due to neutrons from the rock, a 50 cm thick polyethylene shield is installed around the detector. The neutron shield is described in Section 5.1. A detailed Monte Carlo simulation showed that the shield reduces the rate of neutrons hitting the detector to 0.7 neutrons per day. Only 12% of them, which corresponds to 0.08 neutrons per day, have enough energy to produce a nuclear recoil in the region of interest [89].

Muon-induced neutrons
High energetic cosmic muons can also contribute to the neutron background. They can cover large distances in the rock and even reach the underground laboratory. In the rock or other materials close to the detector, they can interact and produce neutrons, for example by spallation. The expected flux of muon-induced neutrons is significantly smaller than the flux of neutrons from radioactivity of the rock [88].

6.8 Estimation of the Rejection Power from Pulse Shape Discrimination

In this section the rejection power for β and γ events due to pulse shape discrimination is estimated for the operation of the ArDM detector in the Canfranc Underground Laboratory. Also the consequences for the rejection power from the charge over light ratio are presented. The rejection power indicates the fraction of β and γ events, which are misidentified as nuclear recoil events. Thus, it is equivalent to the electronic recoil contamination.

As described above, the neutron background in the Canfranc Underground Laboratory is significantly reduced, compared to the measurement on the surface at CERN presented in this chapter. This is due to the shielding from the rock and also the polyethylene shield. For the following estimation it is assumed, that the discrepancy between the measured electronic recoil contamination and the simulated electronic recoil contamination due to photoelectron statistics, which was presented in Section 6.6, is only caused by underestimation of the random coincidences of background neutrons with photons triggering an event in the NaI crystal. Under this assumption, the electronic recoil contamination expected in the Canfranc Underground Laboratory can be approximated by the electronic recoil contamination due to photoelectron statistics.

During the measurements presented in this chapter, the ArDM detector only included a bottom PMT array with 14 PMTs. No PMTs were installed at the top of the detector. The light collection yield in this configuration was measured to 0.7 p.e./keVee [95]. Table 6.6 shows the rejection power from pulse shape discrimination expected in the Canfranc Underground Laboratory for nuclear recoil energies of 30, 40 and 50 keVnr. The values are calculated from the electronic recoil contamination due to photolelectron statistics presented in Section 6.6 and valid for a nuclear recoil acceptance of 68.27 %. For the current light collection yield of

0.7 p.e./keVee the rejection power due to pulse shape discrimination is of the order of 10^{-2}. As shown in the previous section, a combined rejection power from pulse shape discrimination and charge over light ratio of 10^{-7} is required to reduce the background from β and γ radiation below the WIMP rate expected for a spin-independent WIMP-nucleon cross section of the order of 10^{-45} cm^2. Assuming that the two discrimination criteria are independent, the rejection from the charge over light ratio has to be better than 10^{-5} to reach a total rejection power of 10^{-7} for this light collection yield. This is a rather high value and it is not sure that it can be achieved with the charge over light ratio only. The exact values of the minimum required rejection power from the charge over light ratio are also listed in Table 6.6.

light collection yield (p.e./keVee)	**nuclear recoil energy (keVnr)**	**estimation of rejection power from PSD**	**minimum required rejection power from charge/light**
0.7	30	$(1.634 \pm 0.004) \times 10^{-2}$	6.1×10^{-6}
	40	$(1.310 \pm 0.003) \times 10^{-2}$	7.6×10^{-6}
	50	$(1.150 \pm 0.003) \times 10^{-2}$	8.7×10^{-6}
1.75	30	$(1.23 \pm 0.01) \times 10^{-3}$	8.1×10^{-5}
	40	$(3.11 \pm 0.06) \times 10^{-4}$	3.2×10^{-4}
	50	$(9.5 \pm 0.3) \times 10^{-5}$	1.1×10^{-3}
2.8	30	$(9.5 \pm 0.3) \times 10^{-5}$	1.1×10^{-3}
	40	$(1.8 \pm 0.1) \times 10^{-5}$	5.6×10^{-3}
	50	$(7.0 \pm 0.3) \times 10^{-7}$	1.4×10^{-1}

Table 6.6: Estimation of the rejection power from the pulse shape discrimination (PSD) and minimum required rejection from the charge over light ratio (charge/light) for different nuclear recoil energies and light collection yields. The values are valid for a nuclear recoil acceptance of 68.27 %. The chosen light collection yields are the light collection yield of the current detector configuration (0.7 p.e./keVee), the expected light collection yield after adding the top PMT array and re-coating the existing PMTs (1.75 p.e./keVee) and the light collection yield required to reach a rejection better than 10^{-4} at 30 keVnr from the PSD (2.8 p.e./keVee).

A possibility to improve the rejection from the pulse shape discrimination is to increase the light collection yield. In Section 6.6 a list of ongoing actions to increase the light collection yield of ArDM is presented. Among other measures, it includes the addition of the top PMT array and the new coating of the existing PMTs with TPB. These two modifications are not completed yet and the improvement of the light collection yield could not yet been measured, but an estimation of the new light collection yield based on measurements of the light collection yield of single freshly coated PMTs and a GEANT4 simulation [107] of the photon tracks in the detector was performed [101]. It showed, that an improvement by a factor of 2.5 compared to the current light collection yield can be expected [101]. This gives a light collection yield of 1.75 p.e./keVee. For this light collection yield rejection powers of about 10^{-3} at 30 keVnr and 10^{-4} at 50 keVnr are expected in the Canfranc Underground Laboratory. A rejection power of 10^{-4} from the pulse shape discrimination requires only a rejection of 10^{-3} from the charge over light ratio, which seams to be feasible, since for the WARP prototype containing 2.3 l of liquid argon a rejection power of 10^{-4} due to the charge over light ratio was evaluated [108].

To reach a rejection power of 10^{-4} from pulse shape discrimination for events with nuclear recoil energies down to 30 keVnr, a light collection yield of 2.8 p.e./keVee would be needed. This means that the light yield has to increase by a factor of 4 to achieve a rejection of 10^{-4} from the pulse shape discrimination in the region of interest. This rejection power is most likely necessary for background rejection in a dark matter run. Thus, the redesign and new coating of the reflector should improve the light collection yield by a factor of 1.6, to achieve – together with the addition of the top PMT array and the new coating of the existing PMTs – an increase of the light collection yield of a factor of 4.

Chapter 7

Conclusion

In this work the development of the control system for the ArDM experiment and a measurement of the electronic recoil contamination of nuclear recoil events carried out with the light readout system of the ArDM detector have been presented. ArDM is a direct dark matter detection experiment using 850 kg of liquid argon as target. It aims to measure the scintillation light and ionisation charge generated by the elastic scattering of WIMPs on argon nuclei.

The first part of this work discussed the development, installation and commissioning of the ArDM control system, which ensures a safe operation of the ArDM experiment in the Canfranc Underground Laboratory. The control system is based on a programmable logic controller (PLC) and allows for process control. It monitors all the temperatures, pressures and liquid argon levels in the experiment. For the temperature and liquid argon level measurements, sensors, readout devices and installation methods, which are suitable for operation at cryogenic temperature and, in case of the temperature measurement, also in vacuum were developed. The control system regulates the different subsystems of the ArDM experiment, such as the vacuum system, the cooling system for the liquid argon and the argon purification systems. For all these subsystems processes to control the involved actuators were designed, implemented and extensively tested. Furthermore, a new AC power supply unit for the Greinacher circuit, which can be supervised by the ArDM control system, was developed.
Five PVSS (Prozessvisualisierungs- und Steuerungssystem, process visualisation and control system) based user panels, which allow to view the condition of the experiment and control the system manually, were created.

In February 2012 the ArDM control system and the cryogenic system of ArDM have been installed in the Canfranc Underground Laboratory. After the installation, the control system was successfully recommissioned. Since then it is operated remotely without any difficulty. The ArDM control system is thus ready for underground operation of the ArDM detector.

In the second part of this work a measurement of the electronic recoil contamination of nuclear recoil events, i.e. the probability of incorrectly identifying an electronic recoil event as a nuclear recoil event, has been presented. The measurement was performed with the ArDM light readout system, operating the detector in single phase configuration on the surface at CERN. The electronic recoil contamination was determined by applying pulse shape discrimination on the scintillation light signals produced by γs from a ^{22}Na source. The parameters for the pulse shape discrimination have been tuned by analysing data taken with a ^{241}Am-Be neutron source. A strict event selection was applied to the data recorded with the ^{241}Am-Be and the ^{22}Na source. The measured electronic recoil contamination is $(9.8 \pm 4.9) \times 10^{-5}$ for events with

59 – 97 detected photoelectrons (p.e.) and $(1.0 \pm 0.2) \times 10^{-3}$ for events with 36 – 59 detected p.e. for a nuclear recoil acceptance of ∼68 %.

A Monte Carlo simulation of the fraction of electronic recoil events, which are misidentified as nuclear recoil events due to photoelectron statistics, was performed. It showed that for events with an energy below 30 p.e. the electronic recoil contamination is dominated by events mis-identified due to photoelectron statistics, while above 30 p.e. it is dominated by the background, which can be reduced by operating the ArDM detector in the Canfranc Underground Laboratory.
The simulation allows to estimate the β and γ background rejection power, which can be achieved by pulse shape discrimination for dark matter runs in the Canfranc Underground Laboratory. For the current light collection yield of the ArDM detector of 0.7 p.e./keVee and a nuclear recoil energy of 30 keVnr, the rejection power due to pulse shape discrimination has been estimated to $(1.634 \pm 0.004) \times 10^{-2}$.
A combined rejection power from the pulse shape discrimination and the charge over light ratio of 10^{-7} is required to reduce the background from β and γ radiation below the WIMP rate expected for a spin-independent WIMP-nucleon cross section of the order of 10^{-45} cm^2. As the rejection power from the charge over light ratio can be expected to be of the order of 10^{-3} – 10^{-4}, the rejection from the pulse shape discrimination has to be increased. This can be done by improving the light collection yield of the ArDM detector. The simulation showed, that an increase of the light collection yield by a factor four would be needed to reach a rejection power of 10^{-4} for events with a nuclear recoil energy of 30 keVnr.
It has thus been demonstrated in this work, that with some improvement of the light collection yield of the ArDM detector, a rejection power satisfactory for a dark matter search can be achieved with pulse shape discrimination.

Several modifications of the ArDM detector are currently ongoing to improve the light collection yield:

- Installation of twelve additional PMTs at the top of the detector for detection of the primary and secondary scintillation light
- New TPB coating of the existing PMTs of the bottom array to counteract aging effects
- Redesign of the reflector including the TPB coating.

After completion of these modifications, the ArDM detector will also be shipped to the Canfranc Underground Laboratory for measurements of the improved light collection yield, background measurements and subsequent dark matter runs.

Appendix A

Calculation of the Probability Density Function of the Photoelectron Detection Time

In Section 6.6 the fraction of the photon events, which are misidentified as nuclear recoil events due to photoelectron statistics, is estimated with a Monte Carlo simulation. For this purpose, the probability density function of the detection time of the photoelectrons has to be determined. As mentioned in Section 6.6 the probability density function can be described by the convolution of the impulse response function of the PMTs, given by a Gaussian function $G(t - t_0, \sigma)$, and the decay function of the argon excimers:

$$f(t) = G\left(t - t_0, \sigma\right) * \left(H\left(t - t_0\right) \left(\frac{A}{\tau_1} e^{-\frac{t-t_0}{\tau_1}} + \frac{B}{\tau_2} e^{-\frac{t-t_0}{\tau_2}} + \frac{C}{\tau_3} e^{-\frac{t-t_0}{\tau_3}} \right) \right). \tag{A.1}$$

Below the convolution is calculated. For convenience, only the first addend is considered:

$$f(t) = G(t - t_0, \sigma) * \left(H(t - t_0) \, \frac{A}{\tau} \, \exp\left(-\frac{t - t_0}{\tau}\right) \right). \tag{A.2}$$

Making the substitution

$$x = t - t_0 \quad \Leftrightarrow \quad t = x + t_0 \tag{A.3}$$

gives

$$\begin{aligned} f(x + t_0) &= G(x, \sigma) * \left(H(x) \, \frac{A}{\tau} \, \exp\left(-\frac{x}{\tau}\right) \right) && \text{(A.4)} \\ &= \frac{A}{\tau} \int_{-\infty}^{\infty} G(x - y, \sigma) \, H(y) \, \exp\left(-\frac{y}{\tau}\right) dy && \text{(A.5)} \\ &= \frac{A}{\tau} \int_{0}^{\infty} \frac{1}{\sqrt{2\pi}\sigma} \exp\left(-\frac{(x-y)^2}{2\sigma^2}\right) \exp\left(-\frac{y}{\tau}\right) dy && \text{(A.6)} \\ &= \frac{A}{\sqrt{2\pi}\tau\sigma} \int_{0}^{\infty} \exp\left(-\frac{1}{2\sigma^2}\left((x-y)^2 + \tfrac{2\sigma^2}{\tau} y\right)\right) dy. && \text{(A.7)} \end{aligned}$$

The term in the exponential function is

$$-\frac{1}{2\sigma^2}\left((x-y)^2 + \tfrac{2\sigma^2}{\tau} y\right) = -\frac{1}{2\sigma^2}\left(x^2 - 2xy + y^2 + \tfrac{2\sigma^2}{\tau} y\right) \tag{A.8}$$

$$= -\frac{1}{2\sigma^2}\left(y^2 - 2\big(x - \tfrac{\sigma^2}{\tau}\big)y + x^2\right) \tag{A.9}$$

$$= -\frac{1}{2\sigma^2}\left(y^2 - 2\big(x - \tfrac{\sigma^2}{\tau}\big)y + \big(x - \tfrac{\sigma^2}{\tau}\big)^2 - \big(x - \tfrac{\sigma^2}{\tau}\big)^2 + x^2\right) \tag{A.10}$$

$$= -\frac{1}{2\sigma^2}\left(y - \big(x - \tfrac{\sigma^2}{\tau}\big)\right)^2 + \frac{1}{2\sigma^2}\left(\big(x - \tfrac{\sigma^2}{\tau}\big)^2 - x^2\right) \tag{A.11}$$

$$= -\frac{1}{2\sigma^2}\left(y - \big(x - \tfrac{\sigma^2}{\tau}\big)\right)^2 + \frac{1}{2\sigma^2}\left(\frac{\sigma^4}{\tau^2} - \frac{2\sigma^2 x}{\tau}\right) \tag{A.12}$$

$$= -\frac{1}{2\sigma^2}\left(y - \big(x - \tfrac{\sigma^2}{\tau}\big)\right)^2 + \frac{\sigma^2}{2\tau^2} - \frac{x}{\tau}. \tag{A.13}$$

Inserting this in the integral gives

$$f(x + t_0) = \frac{A}{\sqrt{2\pi}\tau\sigma}\exp\left(\frac{\sigma^2}{2\tau^2} - \frac{x}{\tau}\right)\int_0^\infty \exp\left(-\frac{1}{2\sigma^2}\Big(y - \big(x - \tfrac{\sigma^2}{\tau}\big)\Big)^2\right) dy. \tag{A.14}$$

Making the substitution

$$z = \frac{1}{\sqrt{2}\sigma}\Big(y - \big(x - \tfrac{\sigma^2}{\tau}\big)\Big) \quad \Leftrightarrow \quad y = \sqrt{2}\sigma z + x - \tfrac{\sigma^2}{\tau} \tag{A.15}$$

$$\Rightarrow \quad dy = \sqrt{2}\sigma\, dz \tag{A.16}$$

results in

$$f(x + t_0) = \frac{A}{\sqrt{2\pi}\tau\sigma}\sqrt{2}\sigma\exp\Big(\frac{\sigma^2}{2\tau^2} - \frac{x}{\tau}\Big)\int_{-\frac{1}{\sqrt{2}\sigma}\left(x - \frac{\sigma^2}{\tau}\right)}^\infty \exp\left(-z^2\right) dz \tag{A.17}$$

$$= \frac{A}{\sqrt{\pi}\tau}\exp\Big(\frac{\sigma^2}{2\tau^2} - \frac{x}{\tau}\Big)\,\frac{\sqrt{\pi}}{2}\left(1 - \operatorname{erf}\Big(\frac{\sigma^2 - \tau x}{\sqrt{2}\sigma\tau}\Big)\right). \tag{A.18}$$

Resubstituting x finally gives

$$f(t) = \frac{A}{2\tau}\exp\Big(\frac{\sigma^2}{2\tau^2} - \frac{t - t_0}{\tau}\Big)\left(1 - \operatorname{erf}\Big(\frac{\sigma^2 - \tau(t - t_0)}{\sqrt{2}\sigma\tau}\Big)\right), \tag{A.19}$$

which is equivalent to Equation (6.6).

Bibliography

[1] A. Hitachi, *et al.*, *Phys. Rev. B* **27**, 5279 (1983).

[2] G. Bertone, D. Hooper, J. Silk, *Physics Reports* **405**, 279 (2005).

[3] F. Zwicky, *Helvetica Physica Acta* **6**, 110 (1933).

[4] V. C. Rubin, W. K. J. Ford, N. Thonnard, *The Astrophysical Journal* **238**, 471 (1980).

[5] K. G. Begeman, A. Broiels, R. H. Sanders, *Monthly Notices of the Royal Astronomical Society* **249**, 523 (1991).

[6] D. Clowe, *et al.*, *The Astrophysical Journal Letters* **648**, L109 (2006).

[7] D. J. Fixsen, *The Astrophysical Journal* **707**, 916 (2009).

[8] M. White, D. Scott, J. Silk, *Annual Review of Astronomy and Astrophysics* **32**, 319 (1994).

[9] S. Dodelson, L. M. Widrow, *Phys. Rev. Lett.* **72**, 17 (1994).

[10] The Fermi Gamma-ray Space Telescope, http://fermi.gsfc.nasa.gov.

[11] E. Aliu, *et al.*, *The Astrophysical Journal* **697**, 1299 (2009).

[12] D. Hooper, L. Goodenough, *Physics Letters B* **697**, 412 (2011).

[13] L. Bergström, *Annalen der Physik* **524**, 479 (2012).

[14] F. Halzen, D. Hooper, *New Journal of Physics* **11**, 105019 (2009).

[15] J. D. Zornoza, *arXiv:1204.5066 [astro-ph.HE]* (2012).

[16] O. Adriani, *et al.*, *Nature* **458**, 607 (2009).

[17] A. A. Abdo, *et al.*, *Phys. Rev. Lett.* **102**, 181101 (2009).

[18] J. Lewin, P. Smith, *Astroparticle Physics* **6**, 87 (1996).

[19] E. Armengaud, *Comptes Rendus Physique* **13**, 730 (2012).

[20] R. Bernabei, *et al.*, *Nuclear Instruments and Methods in Physics Research A* **592**, 297 (2008).

[21] C. E. Aalseth, *et al.*, *Phys. Rev. Lett.* **107**, 141301 (2011).

[22] G. Angloher, *et al.*, *European Physical Journal C* **72**, 1971 (2012).

[23] E. Armengaud, *et al.*, *Physics Letters B* **702**, 329 (2011).

[24] Z. Ahmed, *et al.*, *Science* **26**, 1619 (2010).

[25] E. Aprile, *et al.*, *Astroparticle Physics* **35**, 573 (2012).

[26] D. Akimov, *et al.*, *Physics Letters B* **709**, 14 (2012).

[27] E. Aprile, *et al.*, *arXiv:1207.5988 [astro-ph.CO]* (2012).

[28] A. Rubbia, *Journal of Physics: Conference Series* **39**, 129 (2006).

[29] D. Akimov, *et al.*, *arXiv:1204.6218 [astro-ph.IM]* (2012).

[30] M. G. Boulay, the Deap Collaboration, *Journal of Physics: Conference Series* **375**, 012027 (2012).

[31] A. Hime, *arXiv:1110.1005 [physics.ins-det]* (2011).

[32] E. Behnke, *et al.*, *Phys. Rev. D* **86**, 052001 (2012).

[33] M. Felizardo, *et al.*, *Phys. Rev. Lett.* **108**, 201302 (2012).

[34] C. Strege, *et al.*, *Journal of Cosmology and Astroparticle Physics* **2012**, 030 (2012).

[35] A. Fowlie, *et al.*, *arXiv:1206.0264 [hep-ph]* (2012).

[36] O. Buchmueller, *et al.*, *European Physical Journal C* **72**, 2020 (2012).

[37] J. Beringer, *et al.*, *Phys. Rev. D* **86**, 010001 (2012).

[38] W. M. Haynes, ed., *CRC Handbook of Chemistry and Physics* (CRC Press, 2011), 92nd edn.

[39] M. Miyajima, *et al.*, *Phys. Rev. A* **9**, 1438 (1974).

[40] R. Platzman, *The International Journal of Applied Radiation and Isotopes* **10**, 116 (1961).

[41] O. Chesnovsky, B. Raz, J. Jortner, *J. Chem. Phys.* **57**, 4628 (1972).

[42] G. Seidel, R. Lanou, W. Yao, *Nuclear Instruments and Methods in Physics Research A* **489**, 189 (2002).

[43] S. Kubota, *et al.*, *Phys. Rev. B* **13**, 1649 (1976).

[44] S. Kubota, *et al.*, *Phys. Rev. B* **17**, 2762 (1978).

[45] S. Kubota, M. Hishida, M. Suzuki, J. Ruan(Gen), *Phys. Rev. B* **20**, 3486 (1979).

[46] T. Doke, K. Masuda, E. Shibamura, *Nuclear Instruments and Methods in Physics Research* **291**, 617 (1990).

[47] T. Heindl, *et al.*, *Europhys. Lett.* **91**, 62002 (2010).

[48] S. Himi, T. Takahashi, J. Ruan(Gen), S. Kubota, *Nuclear Instruments and Methods in Physics Research* **203**, 153 (1982).

[49] T. Doke, *et al.*, *Japanese Journal of Applied Physics* **41**, 1538 (2002).

[50] D. Gastler, *et al.*, *Phys. Rev. C* **85**, 065811 (2012).

[51] C. Regenfus, *et al.*, *Journal of Physics: Conference Series* **375**, 012019 (2012).

[52] R. Chandrasekharan, Design of the Light Readout for the ArDM Experiment, Ph.D. thesis, ETH Zürich, Diss. ETH No. 16985 (2007).

[53] S. Amoruso, *et al.*, *Nuclear Instruments and Methods in Physics Research A* **523**, 275 (2004).

[54] W. Walkowiak, *Nuclear Instruments and Methods in Physics Research A* **449**, 288 (2000).

[55] D. W. Swan, *Proceedings of the Physical Society* **82**, 74 (1963).

[56] A. Bettini, *et al.*, *Nuclear Instruments and Methods in Physics Research A* **305**, 177 (1991).

[57] E. Buckley, *et al.*, *Nuclear Instruments and Methods in Physics Research A* **275**, 364 (1989).

[58] A. Borghesani, G. Carugno, M. Cavenago, E. Conti, *Physics Letters A* **149**, 481 (1990).

[59] A. Bolozdynya, *Nuclear Instruments and Methods in Physics Research A* **422**, 314 (1999).

[60] C. Monteiro, J. Lopes, J. Veloso, J. dos Santos, *Physics Letters B* **668**, 167 (2008).

[61] M. Suzuki, S. Kubota, *Nuclear Instruments and Methods* **164**, 197 (1979).

[62] A. Williams, R. Sara, *The International Journal of Applied Radiation and Isotopes* **13**, 229 (1962).

[63] T. Aoyama, *Nuclear Instruments and Methods in Physics A* **234**, 125 (1985).

[64] C. Amsler, *et al.*, *JINST* **5**, P11003 (2010).

[65] L. Epprecht, Design, construction and first commissioning of a 1 ton liquid argon detector for Dark Matter search (ArDM), Ph.D. thesis, ETH Zürich, Diss. ETH No. 20921 (2012).

[66] W. M. Burton, B. A. Powell, *Appl. Opt.* **12**, 87 (1973).

[67] V. Gehman, *et al.*, *Nuclear Instruments and Methods in Physics Research A* **654**, 116 (2011).

[68] J. Flournoy, I. Berlman, B. Rickborn, R. Harrison, *Nuclear Instruments and Methods in Physics Research A* **351**, 349 (1994).

[69] V. Boccone, *et al.*, *Journal of Instrumentation* **4**, P06001 (2009).

[70] F. Resnati, Modeling, design and first operation of the novel double phase LAr LEM-TPC detector, Ph.D. thesis, ETH Zürich, Diss. ETH No. 20550 (2012).

[71] P. Benetti, *et al.*, *Astroparticle Physics* **28**, 495 (2008).

[72] M. J. Berger, J. S. Coursey, M. A. Zucker, J. Chang, ESTAR, PSTAR and ASTAR: Computer Programs for Calculating Stopping-Power and Range Tables for Electrons, Protons and Helium Ions (version 1.2.3, 2005), [Online] Available: http://physics.nist.gov/Star [2012, 10], National Institute of Standards and Technology, Gaithersburg, MD.

[73] D. Lussi, Ph.D. thesis in preparation. ETH Zürich.

[74] H. Greinacher, *Zeitschrift für Physik* **4**, 195 (1921).

[75] J. D. Cockcroft, E. T. S. Walton, *Proceedings of the Royal Society of London. Series A* **136**, 619 (1932).

[76] M. Simon, Building a Greinacher high voltage generator and tests of it in liquid nitrogen and liquid argon with a field mill (2007). Semester Thesis, ETH Zürich.

[77] S. Horikawa, *et al.*, *Journal of Physics: Conference Series* **308**, 012027 (2011).

[78] V. Kamaraju, M. S. Naidu, *High voltage engineering* (Tata McGraw-Hill, 2009), fourth edn.

[79] L. Kaufmann, Detector Performance and Background Studies for the ArDM Experiment, Ph.D. thesis, ETH Zürich, Diss. ETH No. 17806.

[80] A. Badertscher, *et al.*, ArDM status report (2011).

[81] P. V. Rysselberghe, *The Journal of Physical Chemistry* **36**, 1152 (1931).

[82] Schneider Electric, *Automation platform Modicon Premium* (2008).

[83] B. Briss, L. Knipp, M. Schagginger, *PVSS II - Process visualization and control system: Getting Started - Basics* (Version 2.0, ETM professional control GmbH, 2004).

[84] E. Vitté, *InterSections: Le magazine Schneider Electric de l'enseignement technologique et professionnel*, La régulation, [Online] Available: http://www.intersections.schneider-electric.fr/stock_images/telec/1/n3/Guide_technique11.pdf (2004).

[85] V. Broida, *Automatica* **5**, 677 (1969).

[86] L. Epprecht, First Tests on the Cryogenic Installations of the ArDM Experiment (2008). Diploma Thesis, ETH Zürich, ETHZ-IPP 2008-05.

[87] A. Badertscher, *et al.*, *Journal of Instrumentation* **7**, P08026 (2012).

[88] J. Carmona, *et al.*, *Astroparticle Physics* **21**, 523 (2004).

[89] P. Mijakowski, Contributions to the ArDM meetings (2010).

[90] W. H. Lippincott, *et al.*, *Phys. Rev. C* **78**, 035801 (2008).

[91] M. Boulay, *et al.*, *arXiv:0904.2930v1 [astro-ph.IM]* (2009).

[92] A. Rytz, *Atomic Data and Nuclear Data Tables* **47**, 205 (1991).

[93] L. B. Magnusson, *Phys. Rev.* **107**, 161 (1957).

[94] M. Thompson, J. Taylor, *Nuclear Instruments and Methods* **37**, 305 (1965).

[95] C. Lazzaro, Reconstruction of the muon tracks in the OPERA experiment and first results on the light collection in the ArDM experiment, Ph.D. thesis, ETH Zürich, Diss. ETH No. 20551 (2012).

[96] L. Scotto Lavina, *Light Readout Analysis Tutorial: Instructions for the use of the LR-Analysis framework* (2010).

[97] The root system, http://root.cern.ch/.

[98] R. Acciarri, *et al.*, *Nuclear Instruments and Methods in Physics Research A* **607**, 169 (2009).

[99] R. Acciarri, *et al.*, *Journal of Instrumentation* **5**, P06003 (2010).

[100] L. Kaufmann, A. Rubbia, *The Identification of Dark Matter, Background studies for a ton-scale argon dark matter detector (ArDM)*, chap. 64, pp. 508–513.

[101] The ArDM collaboration, ArDM (LSC EXP-08) status report (2012).

[102] J. de Laeter, *et al.*, *Pure Appl. Chem.* **75**, 683 (2003).

[103] H. H. Loosli, *Earth and Planetary Science Letters* **63**, 51 (1983).

[104] M. G. Stabin, L. C. da Luz, *Health Phys.* **83**, 471 (2002). [Online] Available: www.doseinfo-radar.com.

[105] P. Benetti, *et al.*, *Nuclear Instruments and Methods in Physics Research A* **574**, 83 (2007).

[106] D. Acosta-Kane, *et al.*, *Nuclear Instruments and Methods in Physics Research A* **587**, 46 (2008).

[107] S. Agostinelli, *et al.*, *Nuclear Instruments and Methods in Physics Research A* **506**, 250 (2003).

[108] L. Grandi, WARP: An argon double phase technique for dark matter search, Ph.D. thesis, University of Pavia.

List of Figures

List of Tables

Acknowledgement

I would like to express my gratitude to everyone who supported me during these four years of doctoral studies. First of all, I would like to thank Prof. André Rubbia for giving me the opportunity to work in this interesting project, for his supervision, support and valuable suggestions.
I am very grateful to Andreas Badertscher for proofreading this thesis very carefully and efficiently.
I would like to thank Alessandro Curioni, Sosuke Horikawa and Alberto Marchionni. They were always on hand with help and advice.
Invaluable technical support I received from Adamo Gendotti, Leo Knecht, Gustav Natterer and Thierry Viant.
I am very thankful to Rosa Bächli and Rita Vonesch, who always took care of all the administrative formalities, which occurred during my doctoral studies.
Special thanks go to Lukas Epprecht, who not only spent innumerable hours with me working in the laboratory on ArDM, but also had the pleasure to put me with the crane in the ArDM detector vessel. I am also very thankful to Devis Lussi, who introduced me to the LRAnalysis program with a lot of patience. Both of them always found time to answer my questions of all kind.
During the last four years I had the opportunity to work together with: Claudia Lazzaro, Claudia Strabel, Filippo Resnati, Silvestro Di Luise, Luigi Esposito, Sebastien Murphy, Nguyen Khoi Nguyen, Federico Petrolo, Biagio Rossi, Davide Sgalaberna. I would like to thank them for their daily support.
I am thankful to Nicolas Bourgeois, Gilles Maire and Sylvain Ravat from the CERN PH-DT-DI group. Without them the realisation of the ArDM control system would not have been possible.